DEPARTAMENTO DE ASTROFISICA
Universidad de La Laguna

Eruptive phenomena in the solar atmosphere: radiation-MHD modeling and code development

Memoria que presenta
Daniel Nóbrega-Siverio
para optar al grado de Doctor
por la Universidad de La Laguna.

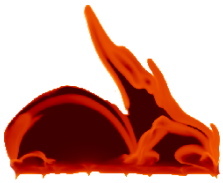

Director:
Prof. Fernando Moreno-Insertis
Co-supervisor:
Dr. Juan Martínez-Sykora

INSTITUTO Đ ASTROFISICA Đ CANARIAS
Junio de 2018

Resumen

En la atmósfera solar tienen lugar continuamente una extraordinaria variedad de fenómenos eruptivos que abarcan un amplio rango de escalas espaciales y temporales. De especial interés son aquellos relacionados con reconexión magnética entre sistemas que interactúan en la atmósfera, sobre todo cuando es resultado de emergencia de flujo magnético procedente del interior solar. Dichos fenómenos causan grandes perturbaciones en la atmósfera solar, liberan energía magnética que se transforma en energía cinética e interna del plasma y radiación, expulsan masa de forma impulsiva, y provocan la reconfiguración del campo magnético cromosférico y coronal. Entre los fenómenos eruptivos, hay uno cuya comprensión ha progresado lentamente desde que se les conoció observacionalmente hace muchas décadas: los *surges*.

Los *surges* son eyecciones frías, densas y no colimadas observadas típicamente en líneas cromosféricas, como Hα 6563 Å, con velocidades desde unas pocas hasta varias decenas de km s^{-1} y longitudes de $10 - 50$ Mm. Aparecen frecuentemente en la atmósfera relacionados con otros eventos de naturaleza efímera como estallidos UV o *jets* coronales de EUV/Rayos-X. Los experimentos numéricos idealizados del pasado explican los *surges* como un subproducto de reconexión magnética que tiene lugar entre los sistemas emergentes y preexistentes, y que, con el tiempo, arrastra plasma cromosférico a alturas superiores en la atmósfera. A pesar de su interés, estos experimentos carecen de algunos mecanismos físicos fundamentales a la hora de tratar con los *surges*, lo que supone que solamente puedan considerarse como primeros pasos en su investigación.

Esta tesis abarca el fenómeno *surge* desde cuatro puntos de vista: (1) desde su enfoque básico, que es teórico, modela la formación y evolución de los *surges* usando un código radiativo-magnetohidrodinámico (R-MHD) que incluye un tratamiento realista de las propiedades del plasma y del transporte radiativo; (2) desde una perspectiva observacional, analiza observaciones coordinadas de alta resolución de la cromosfera y región de transición (RT), explora la respuesta de las líneas de RT a la eyección de un *surge*, y estudia la relación estrecha entre *surges* y otros fenómenos como estallidos UV; (3) desde una perspectiva de modelado directo, crea observaciones sintéticas que nos permiten entender algunas de las peculiares características vistas en las observaciones y proporcionarles un fundamento teórico; y (4) desde un punto de vista de programación científica, desarrolla un módulo de Fortran que mejora la eficiencia computacional del término de difusión ambipolar, abriendo, de esta manera, la posibilidad de incluir efectos de ionización parcial en la electrodinámica de nuestros estudios por medio de la ley generalizada de Ohm.

El primer objetivo se logra gracias a las posibilidades ofrecidas por el código Bifrost. Mediante experimentos R-MHD 2.5D de emergencia de flujo magnético desde las capas subyacentes a la superficie solar hasta la corona, hemos encontrado que el *surge* se forma a pesar de la interacción previa del campo emergente con las celdas granulares en y por debajo de la superficie. El *surge* se separa de la región emergida como consecuencia de choques fuertes causados por el impacto de plasmoides eyectados a lo largo de la capa de corriente en el sitio de reconexión. Durante su ascenso, los elementos de plasma del *surge* experimentan aceleraciones que superan por mucho la gravedad solar, mientras que en la fase central y de descenso sufren caída libre. Usando trazado Lagrangiano detallado, distinguimos diferentes poblaciones de patrones evolutivos dentro del *surge*, algunas de ellas directamente relacionadas con procesos de calentamiento/enfriamiento incluidos como parte del código Bifrost. De hecho, hemos encontrado que una fracción no despreciable del *surge* no puede ser reproducida en experimentos previos y más idealizados debido a la falta de un tratamiento adecuado para la termodinámica y fuentes de entropía.

Hemos conseguido el segundo objetivo por medio de observaciones de un *surge* Hα simultáneo a un estallido UV obtenidos con el *Interface Region Imaging Spectrograph* (IRIS) y el *Swedish 1-m Solar Telescope* (SST), respectivamente. Aunque tradicionalmente relacionados con líneas cromosféricas, hemos encontrado que los *surges* pueden exhibir emisión UV realzada en líneas de Si IV con perfiles que son más brillantes y anchos que en una RT promedio. Además, proporcionamos evidencia observacional que respalda el origen común y la relación entre *surges* y estallidos UV.

El tercer objetivo se consigue por medio de modelado directo de experimentos numéricos que incluyen la ionización fuera del equilibrio de elementos clave en la RT como el silicio y el oxígeno. Los resultados muestran que la RT que envuelve al *surge* se ve fuertemente afectada por efectos de no-equilibrio, aumentando notablemente el número de emisores de las principales líneas de Si IV y O IV. La desviación del equilibrio estadístico se debe a los tiempos cortos de las pérdidas ópticamente delgadas y de la conducción térmica durante la evolución del *surge*. Además, hemos concluido que los efectos de línea de visión son importantes para entender los abrillantamientos interminentes en Si IV y O IV dentro de los *surges*.

Finalmente, hemos logrado el último propósito de esta tesis a través del desarrollo de un nuevo módulo en el código Bifrost que implementa el método *Super Time-Stepping* (STS) para acelerar los cálculos con difusión ambipolar. Mediante un análisis en detalle del método, encontramos la combinación óptima de parámetros que garantiza estabilidad y eficiencia. Como primera aproximación al trabajo a realizar en la etapa post-doctoral, en el último capítulo empezamos a explorar los efectos de difusión ambipolar en el proceso de emergencia de flujo y en el propio *surge*.

Unesco: 210602, 210604, 220409, 220410

Abstract

A bewildering variety of eruptive and ejective phenomena continually take place in the solar atmosphere on a wide range of space and time scales. Particular attention was devoted in the past decades to those associated with the reconnection of magnetic field lines of separate plasma systems that come into contact in the atmosphere, especially when this is the result of the emergence of magnetic flux from the solar interior. Such events can cause a large disruption of the solar atmosphere, lead to the release of magnetic energy which is turned into kinetic and internal energy of the plasma and radiation, launch impulsive mass ejections, and bring about the reconfiguration of the magnetic domain structure in the chromosphere and corona. Even though observationally known for many decades now, among those dynamic phenomena there is one whose understanding has progressed very slowly: the surges.

Surges are cool, dense and non-collimated ejections typically observed in chromospheric lines, like Hα 6563 Å, with velocities of a few to several tens of km s^{-1} and lengths of $10-50$ Mm. They frequently arise in the solar atmosphere related to other transient events like UV bursts or EUV/X-Ray coronal jets. Through idealized numerical experiments, the surges have been explained as a by-product of magnetic reconnection taking place between emerging and preexisting magnetic systems in the atmosphere that eventually causes chromospheric plasma to be dragged into higher layers. In spite of their interest, those experiments miss a number of fundamental physical mechanisms at work when the surges are ejected, so they constitute only a preliminary step in this field.

This thesis addresses the surge phenomenon under a fourfold perspective: (1) its basic approach is theoretical, and is carried out by modeling the formation and evolution of the surges using a radiation-magnetohydrodynamics (R-MHD) code that includes a realistic treatment of the material plasma properties and radiation transfer; (2) from an observational point of view, we analyze coordinated high-resolution observations of the chromosphere and transition region (TR), exploring the response of TR lines to a surge ejection and the close relationship of surges to other events like UV bursts; (3) from a forward modeling perspective, synthetic observations are created that permit us to understand some of the peculiar features seen in the actual observations and provide a theoretical basis for them; and (4) from the point of view of code development, we have created a Fortran module that improves the computational efficiency of the ambipolar diffusion term and opens up the possibility of including partial ionization effects on the electrodynamics of the system via the generalized Ohm's law.

The first objective is achieved thanks to the possibilities afforded by the Bifrost code. Via 2.5D R-MHD experiments of magnetic flux emergence from the solar layers beneath the surface up to the corona, we have found that a surge is formed in spite of the prior interaction of the the emerging field with the granular cells at and below the surface. The surge detaches from the emerged region as a consequence of strong shocks that develop following the impact of plasmoids ejected along the current sheet in the reconnection site. The surge plasma elements experience accelerations well in excess of the solar gravity value in the onset phase, while it undergoes free-fall in the central and decay phases. Using detailed Lagrange tracing, we have discerned different populations with distinct evolutionary patterns within the surge, some of them directly related to the heating/cooling processes included as part of the Bifrost code. In fact, we have found that a non-small fraction of the surge could not be obtained in previous and more idealized experiments because of the lack of a proper treatment of the thermodynamics and entropy sources.

The second goal of the thesis has been accomplished through the observation of an episode of simultaneous occurrence of an Hα surge and of a UV burst obtained with the Swedish 1-m Solar Telescope (SST) and the Interface Region Imaging Spectrograph (IRIS), respectively. Although surges are traditionally related to chromospheric lines, we have found that they can exhibit enhanced UV emission in TR lines of Si IV with brighter and broader spectral profiles than the average TR. Furthermore, we have provided additional observational evidence to support the common origin and relationship between surges and UV bursts.

The third objective is achieved by means of forward modeling of numerical experiments that include nonequilibrium ionization of key elements in the TR like silicon and oxygen. The results show that the TR enveloping the surge is strongly affected by nonequilibrium ionization effects, noticeably increasing the number of emitters of the main lines of Si IV and O IV. The departure from statistical equilibrium is due to the short characteristic times of the optically-thin losses and heat conduction during the surge evolution. In addition, we have concluded that line-of-sight effects are important to understand prominent and spatially intermittent Si IV and O IV brightenings within the surges.

Finally, the last goal of this thesis has been accomplished through the creation of a new module in the Bifrost code that implements the Super Time-Stepping (STS) method to speed up the calculation of the ambipolar diffusion term. After carrying out an in-depth analysis of the method, we have found the optimum combination of parameters that ensures stability and efficiency. As a first instance of work to be completed in the postdoctoral phase, in the final chapter we have started to explore the effects of ambipolar diffusion on the magnetic flux emergence process leading to the surge phenomenon and in the surge itself.

Unesco: 210602, 210604, 220409, 220410

Contents

1

Introduction

1.1 Brief perspective of eruptive phenomena in the solar atmosphere

The Sun is a dynamic star that exhibits a wide variety of eruptive and ejective phenomena. Observed in virtually all electromagnetic ranges, such as X-rays, extreme-ultraviolet (EUV), UV, visible light, infrared (IR) or radio, those phenomena cover a large spectrum of sizes and released energy. Among them, we find:

- Penumbral microjets: elongated transients in the chromosphere of sunspot penumbrae with typical lifetime of up to 1 minute (e.g., Katsukawa et al., 2007; Drews & Rouppe van der Voort, 2017; Samanta et al., 2017).

- Spicules: thin jet-like features of cool matter with sizes of a few megameters (Hansteen et al., 2006; De Pontieu et al., 2007; Pereira et al., 2012; Tsiropoula et al., 2012; Tian et al., 2014; Pereira et al., 2014; Skogsrud et al., 2015; Pereira et al., 2016; Martínez-Sykora et al., 2018, among others). There are two types of spicules: type I, with lifetimes of order $3-7$ minutes and ascending velocities of $15-40$ km s^{-1}; and type II, with lifetimes around $3-10$ minutes and faster velocities, namely, $30-110$ km s^{-1}. The latter are seen to fade out from cool lines such as Ca II H and Hα and then appear in hotter lines that form typically at transition region (TR) temperatures, like Si IV 1402 Å or Lyα 1216 Å, as a consequence of heating (e.g., Chintzoglou et al., 2018).

- Macrospicules: giant spicules with sizes between 7 and 45 Mm and lifetimes between 5 and 40 minutes, mostly detected in polar coronal holes in EUV lines like He II 304 Å (e.g., Bohlin et al., 1975; Habbal & Gonzalez, 1991; Pike & Harrison, 1997; Madjarska et al., 2006; Murawski et al., 2011; Kayshap et al., 2013)

- Surges: non collimated ejections of chromospheric plasma typically observed in Hα 6563 Å that often appear associated with flux emergence. Their lifetime ranges between several minutes to one hour, they have velocities of 50 km s^{-1} and sizes around $10 - 50$ Mm, reaching, in extreme cases, 200 km s^{-1} and $100 - 200$ Mm, respectively (Schmieder et al., 1984; Canfield et al., 1996; Kurokawa et al., 2007; Nelson & Doyle, 2013; Madjarska et al., 2017, among others).

- UV bursts: transient roundish explosions ($\sim 8 \times 10^4$ K) with lifetimes of ~ 5 min. Discovered by Peter et al. (2014) using the Interface Region Imaging Spectrograph (IRIS) satellite (De Pontieu et al., 2014), they are typically detected in opposite polarity regions and in close relation to flux emergence. At present, UV bursts (also known as IRIS bombs) constitute a hot topic for solar researchers interested in eruptive phenomena (e.g., Judge, 2015; Vissers et al., 2015; Kim et al., 2015; Tian et al., 2016; Grubecka et al., 2016; Chitta et al., 2017; Hansteen et al., 2017; Young et al., 2018).

- Coronal jets: hot, fast and collimated ejections typically observed in EUV and X-rays with an inverted-Y shape. They are classified into two types: standard coronal jets (Shibata et al., 1992b; Shimojo et al., 1996; Wang et al., 1998; Savcheva et al., 2007; Moreno-Insertis et al., 2008; Fang et al., 2014; Chen et al., 2017, e.g.,) or coronal blow-out jets (e.g. Moore et al., 2010; Moreno-Insertis & Galsgaard, 2013; Archontis & Hood, 2013; Young & Muglach, 2014; Pariat et al., 2016; Shen et al., 2017). A recent review of this topic can be found in the paper by Raouafi et al. (2016).

- Flares: one of the most energetic events in the solar atmosphere and, probably, the most studied eruptive phenomena since their first observation (Carrington, 1859; Hodgson, 1859). Flares strongly tend to take place in active regions, and are able to release up to 10^{32} erg of energy. They can be also divided into two categories: long-duration-events and impulsive flares (see the fundamental theoretical papers by Carmichael, 1964; Sturrock, 1966; Hirayama, 1974; Kopp & Pneuman, 1976, and the reviews by Priest & Forbes, 2002; Fletcher et al., 2011; Shibata & Magara, 2011).

- Coronal mass ejections (CMEs): extremely violent and energetic events. The amount of released energy in those phenomena is similar to that in flares, up to 10^{32} erg, and often appear in combination with them. CMEs are able to hurl up to 10^{13} kg of solar plasma into the heliosphere. The average velocity of those events is ~ 490 km s^{-1}, although the maximum ones can reach up to few thousands km s^{-1}(see Shibata & Magara, 2011; Webb & Howard, 2012; Yan et al., 2017; Green et al., 2018, and references therein).

The myriad of eruptive phenomena and their importance for the structure of the solar atmosphere make them a vibrant and active research area. Of special interest are those resulting from the interaction of magnetic flux recently emerged from the solar interior with the preexisting coronal magnetic field: many prominent features in the solar atmosphere are related to this fundamental process. As a result of magnetic flux emergence, current sheets

are formed and magnetic reconnection can ensue, leading to the disruption and reconfiguration of the coronal magnetic field. Those changes can be manifested in many ways like: (a) impulsive release of mass and energy that may constitute a significant input to the upper solar atmosphere and to the solar wind (Raouafi et al., 2016); (b) formation of strong shocks and generation of turbulence (Priest, 2014); (c) efficient energy transport via radiation and thermal conduction; (d) nonequilibrium (NEQ) effects in the ionization and recombination of the different atomic species (Raymond & Dupree, 1978; Joselyn et al., 1979; Kneer, 1980); (e) nonthermal processes and acceleration of particles (Priest & Forbes, 2002); (f) quasi-periodic radio emission due to tearing instabilities (Furth et al., 1963) and coalescence of plasmoids in the current sheet (Karlický et al., 2010), and so forth. The interaction between the emerged region and the preexisting coronal field can even provide telltale signatures about the structure of the magnetic fields below the surface, which is a useful diagnostic tool for the solar dynamo (Cheung & Isobe, 2014).

It seems clear, from the list of implications mentioned above, that to obtain a complete picture of the solar atmosphere, an in-depth analysis of eruptive and ejective phenomena is necessary, which implies taking into account a bewildering variety of physical processes acting on different space and time scales.

1.2 A piece of the eruptive phenomena puzzle: the surges

Within the catalog of eruptive phenomena, there is one that remains poorly analyzed and understood: the surges. This is an intriguing fact taking into account that they are common events that often appear associated with one of the most studied scientific targets of the solar atmosphere: the flares. In order to recall how surges fit into the eruptive phenomena puzzle, we provide a historical overview of surge observations (Section 1.2.1) followed by the theoretical approach to this phenomenon (Section 1.2.2).

1.2.1 Historical development of surge observations

The term *surges* was first introduced by McMath & Pettit (1937). In that paper, the authors thought that surges were a new different subclass of prominences of transient nature and peculiar behavior. They appeared as darkenings mainly in the Hα 6563 Å images in the vicinity of sunspots. When seen on the disk, they showed rising and falling motions akin to the ones of the sea in a coastline; when observed at the limb, they looked liked spike-like structures rising and falling practically along the same path. Concerning the latter, Figure 1.1 contains an image from that paper in which three different surges observed at the limb in 1936 are shown. In the figure, we can appreciate the peculiar morphology of the surge that resembles spike-like structures. Furthermore, comparing the second and third row, the form of the surge in the decay phase is practically identical in Hα 6563 Å as in Ca II K.

In the 1940s, additional attention was drawn to the surges because of their frequent occurrence in association with flares. Newton (1942) analyzed 25 of them finding that their time evolution could be summarized as follows: the surge appeared a few minutes after the brightenings associated with the flare eruption, with average upward velocities of 50 km

PLATE XIII

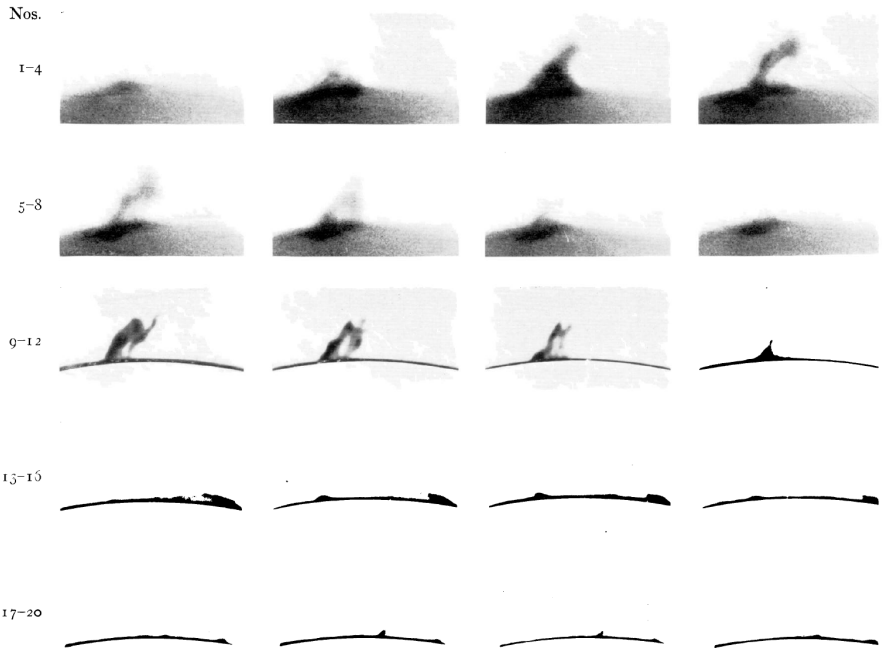

FIGURE 1.1— Observations by McMath & Pettit (1937) that lead to the term *surges*. The first three rows show a great surge from August 8, 1936. Numbers I-4 contain the rise in Hα; 5-8, the fall in Hα; and 9-I2, the fall in Ca II K. Those images have a cadence of 6 minutes. The last two rows show small surges observed in July 16, 1936 (numbers I3-I6) and August 22, 1936 (I7-20), with a cadence of 12 and 3.7 minutes, respectively.

s^{-1} (although their maximum velocities could reach up to 200 km s^{-1}); later, downward motions were detected with velocities around -30 km s^{-1}; and finally, the surge faded out with velocities around -50 km s^{-1}. In spite of the technical limitations of that time, an increasing amount of observational evidence indicated that the surges were not a subclass of prominences. They were effectively a new phenomenon characterized by rapid outward motions followed by a slower decay phase (McMath & Mohler, 1948), and where the Hα profiles showed asymmetric absorption, first in the blue wing (Ellison, 1943), and later in the red wing (Švestka, 1951). The strong correlation of surges and flares earned them the moniker *flare surges* (Ellison, 1949).

Thanks to further observations in multiple wavelengths in the subsequent years, additional properties were obtained and a noticeable effort was made to discern the mechanisms

behind the surge origin. In this vein, Kirshner & Noyes (1971) found plasma emitting in C III 977 Å surrounding the Hα cool ejection. Roy (1973) proposed that the acceleration of the surge could be explained through the melon-seed instability mechanism (Schlüter, 1957), which is a pinching of the magnetic field lines that ejects plasmoids due to the Lorentz tension force. It was also found that the moving magnetic features (MMF's), seen to traverse the moat around sunspots (Harvey & Harvey, 1973), were apparently able to produce surges (Rust, 1976). In the 1980s, studying the ascending and descending phases of this phenomenon, Cao et al. (1980) and Xu et al. (1981) defended the idea that solar surges result from the ejection of plasmoids as proposed by Roy (1973). Schmahl (1981) analyzed EUV observations to further explore the flare-surge correlation and inferred that the gas pressure gradient was enough to drive a surge. Through C IV 1548 Å and Hα observations, Schmieder et al. (1984) showed that the surge material followed the same path in both spectral lines, and that the surge could be interpreted as a dynamic *cloud* overlying the chromosphere. Verma (1985) found that 20% of solar surges were associated with microwave bursts (2800 - 15000 MHz) and later (Verma, 1986), that some surges with non flare relation could be associated with radio bursts. Additionally, statistical analysis of longitudinal and latitudinal surge distributions seemed to indicate that this cool phenomenon was more abundant in active zones (Verma, 1984; Özgüç, 1989; Özgüç et al., 1991).

In the 1990s and early 2000, most of the observations focused on the importance of the magnetic field, suggesting that the Hα surges could be an indirect result of flux emergence processes and the interaction (possibly reconnection) of the upcoming magnetized plasma with the ambient coronal field (Kurokawa & Kawai, 1993; Schmieder et al., 1995; Gaizauskas, 1996; Canfield et al., 1996; Chae et al., 1999; Yoshimura et al., 2003). Those suggestions were mainly based on (a) the observation of the cool ejections next to emerging bipolar regions, and (b) the detection of surges quasi-simultaneously with hot coronal plasma jets (observed in the EUV or in X-rays). In fact, through statistical analysis of different observational events in emerging flux regions (EFRs), Kurokawa et al. (2007) concluded that new magnetic flux emerged from the solar interior is key for the production of Hα surges. An example of the observations reported in that paper is shown in Figure 1.2. The figure illustrates a surge related to the birth of an EFR through Hα images obtained using different facilities: the two images in the upper row, labelled as 6/1, were taken in the Big Bear Solar Observatory (BBSO); the remaining four, labelled as 6/2, with the Domeless Solar Telescope (DST; Nakai & Hattori, 1985) at Hida Observatory. In the panels, the arrow indicates the location of the surge, the label P marks the penumbra of the sunspot of the active region NOAA 4201, and labels A and B indicate the two opposite magnetic polarities of the EFR. The characteristic morphology of the surge resembling a spike-like structure is clearly seen in the middle panel of the lower row. The close relation between flux emergence regions and surges was especially explored in active regions, where there are many observations of such cool ejections (e.g., Gu et al., 1994; Altas & Duzgelen, 1997; Brooks et al., 2007; Madjarska et al., 2009; Guglielmino et al., 2010).

The major improvements in satellites and telescopes of the past decades have overcome some of the observational limitations of previous studies, thus providing a much more complex perspective of the chromosphere and TR, and consequently, of the surge phenomenon.

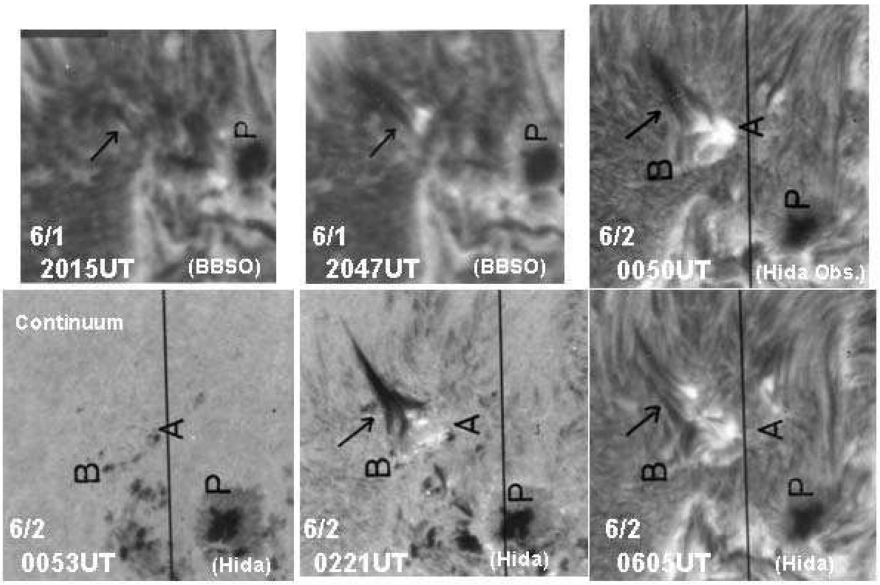

FIGURE 1.2— Image from the paper by Kurokawa et al. (2007): typical example of a surge related to the initial stages of an EFR. The observations were obtained on 1-2 June, 1983 at BBSO and Hida Observatory. The images at 00:53 UT and 02:21 UT are in Hα -5.0 Å and Hα $+0.8$ Å, respectively, while the others are in the Hα line center. The arrow indicates the location of the surge; label P, the penumbra of the sunspot; and labels A and B, the opposite magnetic polarities of the EFR.

The current observational knowledge about surges can be summarized as follows:

a) It is established now that surges are chromospheric phenomena seen as blue and redshifted absorptions in Hα with line-of-sight (LOS) apparent velocities of a few to several tens of kilometers per second on areas with projected lengths of $10-50$ Mm, reaching, in extreme cases, 200 km s^{-1} and $100-200$ Mm, respectively. In addition, surges have also been detected in other chromospheric lines such as the Ca II 8542 Å infrared triplet (Yang et al., 2013a; Kim et al., 2015), He I 10830 Å (Vargas Domínguez et al., 2014), Hβ 4861 Å (Zhang et al., 2000; Liu & Kurokawa, 2004), and also in Ca II H & K (Nishizuka et al., 2008; Liu et al., 2009). They can be recurrent (Jiang et al., 2007; Uddin et al., 2012; Wang et al., 2014) and/or have apparent rotational and helical motions (Jibben & Canfield, 2004; Bong et al., 2014). Furthermore, recent observations show that surges appear to be related to shocks (Yang et al., 2014) and Kelvin-Helmholtz instabilities (Zhelyazkov et al., 2015), and that they consist of small-scale thread-like structures (Nelson & Doyle, 2013; Li et al., 2016). These thread-like structures can be discerned in Figure 1.3 within the dark patch of the surge obtained by Nelson & Doyle (2013) using the Interferometric

BIdimensional Spectrometer (IBIS; Cavallini et al., 2000) instrument situated at the National Solar Observatory (New Mexico). In the image, besides those structures, the classic behavior of the surge is illustrated, first appearing at the blue wing (top panels) and, later, in the red wing of Hα (bottom panels).

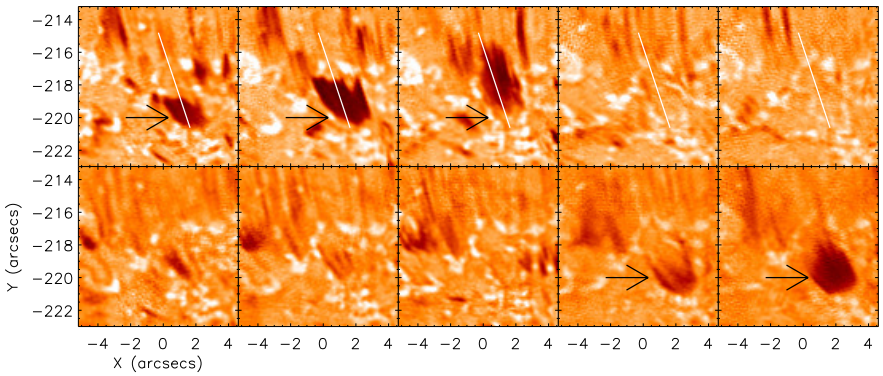

FIGURE 1.3— Temporal evolution of a surge observed by Nelson & Doyle (2013) using IBIS. Top: evolution of this event through time in the blue wing of the Hα line profile (each frame is separated by, approximately, 70 s). Bottom: corresponding FOV and frames in the red wing showing the apparent parabolic trajectory of this event. The black arrow indicates the location of the associated EUV brightening.

b) Surges are seen to be ubiquitous phenomena usually related to magnetic flux emergence (Vargas Domínguez et al., 2014; Kim et al., 2015; Guglielmino et al., 2018). Additionally, surges are frequently observed to appear in close relation to other different phenomena, in particular, to light bridges (Asai et al., 2001; Shimizu et al., 2009; Robustini et al., 2016; Tian et al., 2018), explosive events (Madjarska et al., 2009), UV, EUV or X-ray jets (Chen et al., 2008; Zhang & Ji, 2014), flares (Wang & Liu, 2012; Huang et al., 2014; Schrijver & Higgins, 2015), and even eruptive filaments (Li et al., 2017). Surges have also been suggested to be related to Ellerman bombs (EBs; Watanabe et al., 2011; Yang et al., 2013a; Vissers et al., 2013; Rutten et al., 2013), and may even able to trigger other eruptive phenomena (see Zheng et al., 2013, where the launch of a surge perturbed its surroundings, originating waves and disrupting the adjacent magnetic field unleashing a CME). Recent papers report on the coexistence of surges with bursts in Si IV (Kim et al., 2015; Huang et al., 2017); however, the focus of those papers was mainly on the bursts, without presenting an in-depth analysis of the associated surges. Additionally, surges can also provide useful hints to understand other similar chromospheric-temperature ejections such as macrospicules, since both phenomena show analogies in characteristic lifetimes, sizes, velocities, and in their plasma properties (see the statistical study by Bennett & Erdélyi, 2015).

1.2.2 Theoretical approach to the surges

Even though the surges have been observationally known for several decades now, their understanding has progressed slowly. We have to go back to the seminal paper by Heyvaerts et al. (1977) to set up the basis for the subsequent theoretical development of surges. In that paper, the authors explained how the emergence of magnetized plasma from the solar interior could lead to a conflict of magnetic orientation with the preexisting coronal field. During this conflict, magnetic reconnection could take place at the current sheet formed between both systems and, as a consequence, heating and ejection of hot plasma were obtained. This

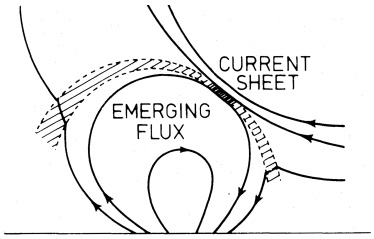

FIGURE 1.4— Representative scheme from the paper by Heyvaerts et al. (1977) to explain how magnetic flux emerged from the solar interior could lead to flares through magnetic reconnection with the preexisting coronal magnetic field.

mechanism to unleash flare eruptions was illustrated by the authors by means of a cartoon reproduced in Figure 1.4. In the image, the stage prior to the triggering of the flare is shown, where a current sheet is created between the two colliding magnetic systems. There, magnetic reconnection by the Petschek mechanism (Petschek, 1964) can occur between both systems. This paradigm of two interacting flux domains was implemented and verified a few years later in a 2D numerical experiment by Forbes & Priest (1984) and, nowadays, it is an extensively studied mechanism in the literature. Although it was able to provide a rough explanation for hot ejections, this elementary mechanism did not explain how cool and chromospheric plasma could be ejected next to flares: the surges continued being a mystery.

The first attempts to model a surge in numerical experiments were carried out by Steinolfson et al. (1979) and Shibata et al. (1982). Their models consisted of 1D hydrodynamic (HD) simulations in which a sudden increase of gas pressure was introduced at the top of the photosphere. The surge was then obtained as a by-product of the matter ejected from the initial burst. The models were able to successfully obtain speeds and timescales similar to the observed ones, but the key role of the magnetic field was not taken into account, so relevant processes such as the magnetic flux emergence and reconnection were omitted.

It was in the 90s when, using the flux emergence paradigm of Heyvaerts et al. (1977), Shibata et al. (1992a) and Yokoyama & Shibata (1995, 1996) showed, through 2.5D magnetohydrodynamics (MHD) numerical models, that cool plasma could be ejected next to a hot jet as a consequence of the *emergence of magnetic flux from the interior*. In Figure 1.5, a modified colored version of the schematic cartoon by Yokoyama & Shibata (1996) is shown

to illustrate the cool (blue) and hot (yellow) ejections in an oblique coronal magnetic field configuration. In the image, the green domain corresponds to the emerged region while the red one is related to the coronal loops created after the magnetic reconnection. In these papers, the authors tentatively identified the cool ejections with Hα surges and described them as resulting from *the slingshot effect due to reconnection, which produces a whiplike motion*. The cool surge had densities around 10^{-11} g cm^{-3}, speeds in the range $\approx 50 - 90$ km s^{-1}, and maximum vertical size of several Mm, which was quite satisfactory concerning the observed properties in Hα. In spite of the computational limitations of the time, these papers constituted a turning point for hot jets and surges. However, there were non-trivial issues in terms of realism like, e.g., the values of temperature and density they used for the corona, namely, 2.5×10^5 K and 1.7×10^{-12} g cm^{-3}, respectively, which are way off the expected ones in the real corona; or that there was no flux emergence process from a convection zone *per se*, just a perturbation of a convectively unstable layer by means of a type of buoyant instability often called the Parker instability.

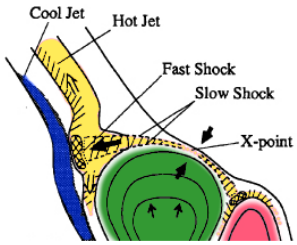

FIGURE 1.5— Schematic cartoon by Yokoyama & Shibata (1996) with added colors to illustrate the ejection of a cool (blue) and hot (yellow) component by means of magnetic reconnection between the emerged magnetized region (green) and the preexisting oblique coronal magnetic field. The red domain corresponds to loops post reconnection.

Using the same sort of setup as Yokoyama & Shibata (1996) but with more realistic coronal parameters, Nishizuka et al. (2008) also found hot and cool ejections in their numerical experiments, thus supporting the magnetic reconnection model for this kind of phenomena. Like previous authors, the acceleration mechanism of the surge was rather vaguely explained by means of the *slingshot effect* that produced a *whiplike motion*. Nishizuka et al. (2008) also suggested that the cool ejections associated with flux emergence could be the cause for jet-like features seen in Ca II H observations. In that paper, the authors found a resemblance between the modeled surge and an observed one in Ca II H broadband filter images taken by Hinode SOT. However, that identification was carried out through morphological image comparisons instead of using a proper treatment through forward modeling.

Further 2.5D models that include the formation of a cool chromospheric ejection are those of Jiang et al. (2012). In their experiments, the coronal background magnetic field is of the canopy-type and the emergence of magnetic flux is produced by changing the bottom boundary conditions in the simulation. Their results show that the height where

the magnetic reconnection takes place determines the size and kind of the ejection. The relevance of the height of the reconnection site was also addressed by Takasao et al. (2013) in their numerical experiments of flux emergence: when the magnetic reconnection takes place near the photosphere, it generates a slow-mode wave pulse that steepens as it goes upwards in the atmosphere, lifting chromospheric material; on the other hand, when the magnetic reconnection site was located in the upper chromosphere, a surge-like ejection was produced by a combination of a slow shock and *whiplike* motions. In the same year, Yang et al. (2013b) studied the hot and cool jets resulting from the interaction between moving magnetic features at the base of their experiment and the preexisting ambient field in the atmosphere. Even though it was the first time that surges were obtained in simulations that included thermal conduction and optically thin radiative losses, the main focus was put on the plasmoids generated by the tearing mode instability (Furth et al., 1963) during magnetic reconnection: the surge was treated as a secondary product without any additional importance.

The first detection of a surge in three dimensional models of magnetic flux emergence was reported by Moreno-Insertis et al. (2008). In that letter, the authors saw that cool and dense plasma was ejected from the reconnection site during the early stages of magnetic reconnection between the emerged region and the ambient field. It was also the first time in which a surge was obtained through flux emergence of a twisted magnetic flux tube introduced in a adiabatically stratified region rather than using a perturbation to promote the Parker instability in a convection-like layer. Although the experiment did not include radiation cooling nor heat conduction, this 3D model provided a new perspective of solar surges. The model was later analyzed in depth by Moreno-Insertis & Galsgaard (2013) finding that the surge consisted of a dense wall-like structure that appeared surrounding the emerged region with temperatures from 10^4 K to a few times 10^5 K. In Figure 1.6, the wall-like structure of the surge is illustrated through a density isosurface ($\rho = 4 \times 10^{-10}$ g cm^{-3}) surrounding the emerged region (green magnetic field lines). Note the morphologic resemblance of this wall with the spike-like structures shown previously in Section 1.2.1. By means of Lagrange tracing, the authors explained the formation of that wall through plasma from the emerged region that was transferred attached to magnetic field lines that changed connectivity in the main reconnection site. The cool ejecta had speeds of typically less than 50 km s^{-1} and were not collimated. Inspired by the observational study of Guglielmino et al. (2010), where surges moved in a preferred direction away from a sunspot, MacTaggart et al. (2015) analyzed in 3D experiments the relation between surges and magnetic reconnection in three different configurations through models of flux emergence in small-scale active regions. In particular, the authors described how the particular geometry of the ambient magnetic field is able to influence the ejection direction of the surges.

The theoretical models described in this section showed that magnetic flux emergence and magnetic reconnection are fundamental processes to obtain surges. Those experiments were able to reproduce some of the observational features of the surges, such as the characteristic megameter size, their small and non-collimated velocity of up to 50 km s^{-1}, and the peculiar spike-like shape. Additionally, they were able to provide a scenario in which surges and jets/flares are ejected simultaneously. Nonetheless, the mentioned experiments are extremely

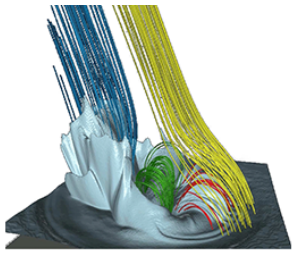

FIGURE 1.6— Image from the paper by Moreno-Insertis & Galsgaard (2013): 3D visualization of the dense domain of the surge through a density isosurface ($\rho = 4 \times 10^{-10}$ g cm^{-3}). Magnetic field lines are shown for the different connectivities: the emerged region (green), the ambient coronal field (yellow), reconnected field lines that keep their open field nature (blue), and the close loops created after the magnetic reconnection process (red).

idealized. Like for other important phenomena of the low solar atmosphere (prominences are a prime example for this), the theoretical study of surges is intricate because of the difficulties of coping with the material properties of the chromospheric plasma.

1.3 Objectives and framework of the thesis

This thesis addresses the surge phenomenon under a fourfold perspective:

- The main block of the thesis studies the surges under a theoretical point of view using state-of-the-art multidimensional numerical models. In this block, the objective is to perform 2.5D numerical experiments of surges obtained through flux emergence using the Bifrost code (Gudiksen et al., 2011), including and analyzing physical mechanisms that have not been taken into account in the previous literature, thus solving open questions related to the properties and features of this complex phenomenon. In Section 1.3.1, we detail the key physical mechanisms considered in this thesis.

- The second block carries out an observational study of surge data obtained with the IRIS satellite and the Swedish 1-m Solar Telescope (SST, Scharmer et al., 2003). In this block, we aim at exploring the response of TR emission lines, like Si IV 1402.77 Å, to the surge phenomenon, in addition to the close relation between surges and other eruptive events like UV bursts. Section 1.3.2 contains the observational reasons to study the surge in new spectral ranges and the diagnostic capabilities of UV spectral lines in the TR for surges.

- The objective of the third block is to combine theory and observations to carry out forward modeling via the spectral synthesis of our numerical data. In Section 1.3.3, we discuss why forward modeling is essential to provide theoretical support and interpret observations. In addition, we argue the reasons to include effects of nonequilibrium

ionization in the numerical experiments, particularly of those elements, such silicon and oxygen, that have important resonance lines that form in the TR and that are key for diagnostics of that region.

- The last block of the thesis addresses the implementation of a new Fortran module for the Bifrost code. Developed in the framework of this thesis, the purpose of this module is to *meet the challenge* posed by the low ionization level of the low atmosphere. Section 1.3.4 describes why it is necessary to include the physical process called ambipolar diffusion to understand the evolution of chromospheric plasma, and why it is crucial to speed up its computation when using multidimensional computer codes.

1.3.1 Theoretical point of view

The theoretical models of surges developed along the past decades (Section 1.2.2), whether 2D or 3D, were helpful in providing basic indications for the mechanisms that may lead to the simultaneous ejection of cold and hot plasma, and for the general properties of surges and hot jets, respectively. However, they lack essential physical processes relevant in the corona, chromosphere and photosphere, such as thermal conduction, optically thin losses, nonequilibrium effects, partial ionization, optically thick radiative transfer, scattering, ... Additionally, most of those models (e.g., Yokoyama & Shibata, 1996; Nishizuka et al., 2008; Jiang et al., 2012; Takasao et al., 2013) did not provide a thorough explanation of key physical mechanisms like the acceleration of the surge. Therefore, those experiments can only be taken as first steps when trying to understand the physics of the surges.

In this thesis, we aim to carry out a theoretical study that explores surges through numerical experiments that combine magnetohydrodynamics, radiation terms, and other important physical mechanisms. Although this task is not simple, the potential value of the results is large: many important aspects of this phenomenon have remained largely unexplored precisely because of this difficulty. In the following, we describe the main theoretical aspects that we have targeted in this thesis divided into two groups: (a) the use of a proper model of magnetic flux emergence within a self-consistent convection zone; and (b) the importance of dealing with entropy sources that had not been taken into account in the previous literature.

(a) Magnetic flux emergence within a self-consistent convection zone.
Observations and theoretical models indicate that magnetic flux emergence is a key mechanism to generate surges. To date, the few numerical experiments in which surges were obtained as a by-product (Section 1.2.2) did not have convection in the solar interior. In those experiments, the upper layers of the solar interior were treated in an approximate way, so the actual passage of magnetized plasma through the solar interior, and also in the photosphere, was grossly oversimplified. For phenomena so closely related to flux emergence like surges, this has to be improved: it is necessary to include a nonidealized model of solar magnetoconvection (see, e.g., the review by Nordlund et al., 2009).

Besides including a realistic self-consistent convection zone, it is also indispensable to properly model the magnetic flux emergence process itself. Radiative-MHD experiments

show that granular motions can strongly modify the rise of the magnetized tubes, deforming, slowing down and even breaking them in separate strands (e.g., Cheung et al., 2007; Martínez-Sykora et al., 2008; Tortosa-Andreu & Moreno-Insertis, 2009; Moreno-Insertis et al., 2018). In particular, Cheung et al. (2007) described how the weaker magnetic tubes are shredded by the convective flows and what reaches the surface leads to a non-coherent salt-and-pepper pattern of opposite polarities at the photosphere; on the other hand, for magnetic tubes of sufficiently high field strength, the tube can survive the rise without major disruption and the flux emergence will occur in a coherent way in the surface. This implies that the pattern of arrival of the magnetized plasma at the surface and the subsequent interaction with the preexistent magnetic field in the atmosphere that leads to the formation of surges critically depend on the evolution of the flux emergence in the solar interior.

(b) Entropy sources.
The previous surge experiments did not take into account the most relevant entropy sources in the solar atmosphere. As an exception, the experiment by Yang et al. (2013b) included thermal conduction and optically thin radiation, but their impact on the surge was not analyzed. Consequently, there are several questions that remain unsolved. A clear example is related to the inclusion of thermal conduction: is this physical process able to impact somehow on the cool material of the surge? Another question concerns the efficiency of the optically thin losses: could heated plasma from the reconnection site be cooled down so quickly that it ends up being part of the cold surge? Further complex questions are related to the radiative energy balance in the solar chromosphere. The chromospheric plasma is dominated by strong spectral lines that are formed out of local thermodynamic equilibrium (LTE), as shown by Carlsson & Leenaarts (2012), so we wonder whether the entropy losses due to the strongest lines of hydrogen, calcium and magnesium can affect the surge matter.

1.3.2 Observational point of view

As a second type of approach to the problem of the surges, within the thesis we have analyzed recent observations of a region in which a surge was emitted. The observational results described in Section 1.2.1 led to the conclusion that an essential component in the solar surge phenomenon is plasma with chromospheric temperatures and densities, as follows from their detection mainly in Hα and/or other chromospheric spectral lines. However, the detection of TR lines coming from the envelope of the surges, which may be crucial for their characterization, is a much less studied topic both observationally and theoretically. This situation leads to the observational objective of this thesis, namely, to take advantage of available high resolution observations for chromospheric and TR lines obtained with current facilities with the aim of discovering (a) the impact of surges in the transition region and how far the spectral lines formed in those layers of the Sun can be helpful for diagnostic purposes; and (b) their close relationship to other dynamical events, e.g., UV bursts.

(a) Surges in TR lines.
In the extended observational literature dealing with the surge phenomenon, there are

only a few papers that include TR lines. Observing a surge at the limb, Kirshner & Noyes (1971) found plasma emitting in the spectral line C III 977 Å, which, in equilibrium, is formed at 6×10^4 K (Raymond & Dupree, 1978). The amount of emission was in agreement with a theoretical model in which a hotter thin layer of ~ 100 km surrounded the cool chromospheric surge plasma visible in Hα. Schmieder et al. (1984) detected plasma in the TR line C IV 1548 Å, which is formed at $\sim 10^5$ K (according to Arnaud & Rothenflug, 1985), co-spatially with the surge observed in Hα. Much later, Madjarska et al. (2009) observed emission in the TR spectral lines N V 1238.82 Å and O V 629.77 Å during the launch and decay of the surge, tentatively suggesting heating of the surge material to TR and coronal temperatures. In addition, all those papers seem to indicate that the TR lines are indeed modified by the appearance of a surge, so it is necessary to further explore the diagnostic possibilities afforded by those spectral lines. An excellent opportunity for the work in this thesis was the availability of recent high-resolution coordinated observations for the same solar region of TR lines obtained with the IRIS satellite, which was launched in 2013, and Hα observations taken with the SST.

(b) UV Bursts.
From their first detection with IRIS (Peter et al., 2014), UV bursts have become an active area of research (see, e.g., Judge, 2015; Vissers et al., 2015; Tian et al., 2016; Grubecka et al., 2016; Chitta et al., 2017; Hansteen et al., 2017, among others). As said in Section 1.2.1, recent papers report on the coexistence of UV bursts with surges (Kim et al., 2015, Huang et al., 2017), leading to the question of how those two phenomena are related and indicating the relevance of studying both transient events together. Like implied above for the case of jets and flares, it is not possible to obtain a full understanding of the UV bursts without proper understanding of the surges: they are necessary to obtain a global perspective of the eruptive phenomena. Within the observational objectives in this thesis, we study the UV bursts in relation to the surge taking advantage of the coordinated IRIS/SST observations mentioned just above.

1.3.3 Forward modeling

Given the realism of the numerical simulations carried out here, a unique opportunity presents itself of carrying out direct forward modeling of the surge phenomenon via spectral synthesis calculated on the basis of our numerical boxes.

(a) The need and opportunity for forward modeling.
As said in Section 1.2.1, in the literature there is no real, direct comparison between surge observations and results from numerical experiments. For instance, the attempt by Canfield et al. (1996) consisted in a comparison of the observations with a schematic cartoon based on the numerical experiments of Yokoyama & Shibata (1996). Another attempt was made by Nishizuka et al. (2008), which just consisted in a basic, visual comparison between morphological features apparent in Hinode/SOT broadband Ca II images and those in temperature and density maps from the numerical experiments. In the letter by Moreno-Insertis et al. (2008), there was also a comparison with Hinode/XRT and EIS observations, but it was focused on the hot coronal jet and did not deal with

the surge phenomenon. With the realistic numerical modeling carried out in the present thesis, we are in an excellent situation for proper comparison of the results with the observations. Since the observations analyzed in the current thesis corresponds to the TR, a natural objective is to carry out forward modeling of lines originated in this region. For a proper comparison between observations and the TR synthetic spectra, we can degrade the latter, both spatially and spectrally, with the adequate Point Spread Functions (PSFs) and rebinning to match the conditions of the IRIS observation. Thus, we are able to provide theoretical explanation and understand the observations.

(b) Nonequilibrium (NEQ) ionization.
In order to obtain realistic synthetic observables, the numerical models have to include the key physical ingredients mentioned in Section 1.3.1. In addition, since the solar atmosphere is a highly dynamical environment (Kneer, 1980; Raymond & Dupree, 1978; Joselyn et al., 1979; Hansteen, 1993, among others), the population levels for different ions of the same atomic species can be out of ionization equilibrium. The effects of NEQ ionization have been shown to be a source of complexity primarily in the chromosphere and transition region for hydrogen (Leenaarts et al., 2007), helium (Golding et al., 2014), and heavier elements (see e.g., Bradshaw & Mason, 2003; Bradshaw & Cargill, 2006; Bradshaw & Klimchuk, 2011; Olluri et al., 2013a; De Pontieu et al., 2015; Reep et al., 2016, and references therein). The recent results of Olluri et al. (2013a, 2015); Martínez-Sykora et al. (2016b), in particular, concerning the silicon and oxygen ions (more specifically, Si IV and O IV), clearly indicate that one must relax the approximation of ionization equilibrium for diagnostic studies that involve their spectral lines. Given that one of the aims in this thesis is to unravel the impact of the surge in the transition region, we include the NEQ effects of those ions to perform the forward modeling and compare with the IRIS observations.

1.3.4 Code development

The last block of the thesis is devoted to code development. A common assumption in numerical experiments of the Sun is to model the plasma using the MHD approximation, i.e., the plasma is treated as a single fluid with complete coupling between its constituent microscopic species. This approximation is able to successfully explain many phenomena in different solar contexts; nevertheless, there are regions and phenomena where this assumption is no longer valid, e.g., because the plasma is partially ionized and there is a decrease of the collisional coupling (Zweibel et al., 2011; Khomenko & Collados, 2012; Martínez-Sykora et al., 2012; Vranjes & Krstic, 2013; Zweibel, 2015; Ballester et al., 2018, and references therein). There is a way to relax the MHD approximations to still treat the plasma as a single fluid but including the mentioned effects: the Generalized Ohm's Law (see the fundamental books by Braginskii, 1965; Mitchner & Kruger, 1973; Cowling, 1976 and its implementation in codes by, e.g., Leake et al., 2005; O'Sullivan & Downes, 2007; Cheung & Cameron, 2012; Martínez-Sykora et al., 2012). Numerical experiments with this extension reported a large impact of the partial ionization effects on the lower solar atmosphere (e.g., Khomenko & Collados, 2012; Khomenko et al., 2014; Shelyag et al., 2016; Martínez-Sykora et al., 2017);

in particular, the ambipolar diffusion and the associated Pedersen dissipation has been seen to noticeably modify the flux emergence process (Leake & Arber, 2006; Arber et al., 2007; Leake & Linton, 2013); more recently, it has been shown that the interaction of neutrals and ions in the chromosphere is a key ingredient to get type-II spicules (Martínez-Sykora et al., 2017). On the basis of those theoretical results, surges are natural candidates to be specially affected by partial ionization effects. However, the computations including partial ionization effects turn out to be very slow when solving them through standard methods. Thus, an objective of this thesis is to implement advanced numerical techniques to increase the efficiency in the numerical experiments that include those effects.

1.4 Methodology

In this section, details about methods and tools used in this thesis are given divided into four parts: Section 1.4.1 details the main numerical tool used in this thesis: the state-of-the-art numerical code Bifrost, which allows to carry out experiments in nonidealized conditions, including the key physical mechanisms explained above; Section 1.4.2 summarizes the tools we have developed for the a-posteriori analysis of the data; in Section 1.4.3, we list the large-scale supercomputing installations used for the calculation of the numerical models; and Section 1.4.4 contains the facilities where the data used in the observational part of the thesis had been obtained.

1.4.1 The Bifrost code

Bifrost is a massively parallel code developed for tridimensional numerical experiments of stellar atmospheres (Gudiksen et al., 2011). In order to explicitly solve the standard partial differential equations of magnetohydrodynamics (MHD), its core uses a staggered mesh in cartesian coordinates (x, y, z). The positioning of the variables in the mesh is as follows: the scalar variables, e.g., the density ρ, are defined in the center of the numerical cells; the components of the basic vector fields, namely, the magnetic field B_i and linear momentum p_i, are located at the center of the cell faces; and the cross product or curl of those vectors, like $(\mathbf{v} \times \mathbf{B})_\mathbf{i}$ or J_i, are defined on the cell edges.

The numerical scheme is a classic method of lines (MOL). It is based on a sixth order operator for the spatial derivatives. Since Bifrost uses a staggered mesh, it is not possible to avoid the use of interpolations to re-collocate the variables in space during the computations. Those interpolations are of fifth order. The time derivatives follow a predictor-corrector scheme of third order described by Hyman et al. (1979). The timestep is controlled by the Courant-Friedrichs-Lewy (CFL) criterion (Courant et al., 1928).

In spite of using high-order methods, the numerical codes are diffusive by their own nature due to the discretization of the equations. To ensure stability, Bifrost employs a diffusive operator that consists of two main terms: a small global diffusive term and the so called hyperdiffusion term inspired by Nordlund & Galsgaard (1995). The latter is a location-specific diffusion that acts in small regions of large gradients or jumps in the variables, like in current sheets or shocks.

The advantage of using the Bifrost code is that we can include different modules that provide physics that has not been used so far in the study of surges. In the following, we summarize the most important ones for this thesis.

- *Magnetic flux injection through the lower boundary.*
  In order to produce magnetic flux emergence, injection of magnetic flux through the lower boundary of the convection zone is carried out using a module developed by Martínez-Sykora et al. (2008). In this module, in particular, we can inject a twisted magnetic tube whose longitudinal and transverse field components have the canonical form of a Gaussian profile with an r-independent pitch (e.g., Fan, 2001).

- *Thermal conduction.*
  The thermal conduction is calculated in the code through the formula by Spitzer (1956). Thermal conduction is primarily important in the corona and, there, along the magnetic field lines. In the code, for simplicity, only the heat flux component parallel to the magnetic field is computed. The perpendicular component is smaller than the numerical diffusivity and therefore ignored.

- *Optically thin losses.*
  The radiative transfer is implemented in Bifrost in a detailed way. From heights from the corona down to the lower transition region and upper chromosphere, the radiative losses can be treated assuming that the atmosphere is optically thin, which is a good approximation for most of the lines originating in those regions. The main contributors to this radiation are the resonance lines of ionized elements such as carbon, oxygen, iron and, to a lesser extent, silicon.

- *Chromospheric radiation approximation.*
  With respect to the radiative transfer in the chromosphere, there are two main terms that have been taken into account: the radiative losses dominated by the strong lines of hydrogen, calcium and magnesium; and the radiative heating due to the absorption of the UV emission of the corona. The details of this approximation for the chromospheric radiation are explained by Carlsson & Leenaarts (2012).

- *Radiative transfer in the photosphere and convection zone.*
  To model the photosphere and the convection zone, it is necessary to range from optically thin to optically thick regimes. To that end, the integration of the radiative transfer equation is computed using an approximation known as *opacity binning* (Nordlund, 1982; Skartlien, 2000): it splits the frequency spectrum in groups (*bins*) where each of those bins is represented by a mean opacity, thus enormously decreasing the computational effort in the numerical integration. In Bifrost, the number of bins can be chosen depending on the needs of the particular calculation (Hayek et al., 2010). In this thesis, we use four bins: one for the continuum and the other three for lines of different strength.

- *Scattering.*
  The coherent scattering contribution is included in the code consistently with the

radiation field. Its effects are important since it can, e.g., modify the temperature distribution in the chromosphere (Skartlien, 2000; Hayek et al., 2010).

- *The equation-of-state (EOS).*
  The EOS can be chosen in Bifrost according to the requirements of each experiment. Since we have a proper treatment of the radiative transfer, in this thesis we opt for the most realistic EOS, which is based on tables generated by the *Uppsala Opacity Package* (Gustafsson et al., 1975). This EOS computes the ionization/recombination of the atoms in LTE and provides the opacity data, thermal emission and scattering probability for the radiation bins.

- *Nonequilibrium (NEQ) of heavy elements.*
  In Bifrost, there exists the possibility of enabling a module developed by Olluri et al. (2013b) to follow the NEQ ionization states of elements with atomic number greater than 2. This module solves the rate equations for those elements using the local values of the temperature, mass density, electron number density n_e and velocity without modifying the results of the radiative-MHD computation. Thus, we are able to calculate the NEQ ionization fraction of elements like, among others, silicon, carbon, or oxygen, which contains spectral lines that are essential to understand the transition region and corona.

- *Generalized Ohm's Law (GOL).*
  The failure of the MHD approximation in situations with important partial ionization effects can still be handled using a single fluid equation extending the induction and energy equations using the Generalized Ohm's Law (GOL). There is a module in Bifrost developed by Martínez-Sykora et al. (2012) that contains the two main terms of the GOL: the ambipolar diffusion, which deals with the decoupling of neutral and charged components, and the Hall effect, which takes into account the drift velocities between ions and electrons.

1.4.2 Tools developed for the analysis a posteriori

As part of the methodology to achieve the objectives of this thesis, we have created a large amount of numerical tools, e.g., to treat the raw numerical data or to deal with the observational files. In the following, we summarize those a posteriori developed tools.

- Lagrangian tracing.
  We have developed a separate program consisting of a suite of routines to calculate the Lagrangian tracers of an ensemble of plasma elements. This program allows us to choose any sample of tracers at a given time once the numerical experiment has finished. The tracers can be evenly or unevenly distributed in the physical domain of the experiment with a desired spacing. Once the distribution is established, we can follow the tracers backward and/or forward in time solving the ordinary differential equation for the element position $\mathbf{r}$, namely,

$$\frac{d\mathbf{r}}{dt} = \mathbf{v}(\mathbf{r}, t), \tag{1.1}$$

where $\mathbf{v}(\mathbf{r}, t)$ is the Eulerian velocity map at that position. The solution of this differential equation is carried out by means of a 4th-order Runge-Kutta method. For accuracy, given the high values of the acceleration in different stages of the evolution, we must have high cadence in the stored snapshots (in our case, the cadence is 0.2 seconds). The importance of following Lagrangian elements to unravel details of the evolution of the plasma led Leenaarts (2018) to implement a module in Bifrost that calculates the Lagrangian tracing during the numerical run instead of computing it *a posteriori*, making thus possible an accurate Lagrangian tracing even in the most dynamical environments.

- Statistical analysis.
  In order to carry out statistical analysis, we have programmed a batch of specific routines that can compute the basic moments (mean, standard deviation, skewness and kurtsosis) of a given statistical distribution. In addition, we can calculate other relevant statistical quantities such as the mode and fit the distributions to Gaussian functions. This is applied to study, e.g., the large number of elements (up to 10^5) followed by the Lagrangian tracing, or to deduce linewidths and Doppler shifts in observations. Furthermore, to obtain more information from the statistical analysis, we use histograms and Joint Probability Density Functions (JPDFs). Thus, we are able to discern different pattern of behaviors in the plasma population of a surge or its acceleration distribution.

- Visualization tools.
  We have also created visualization tools: a routine to plot magnetic field lines that takes advantage of parallelization capabilities to speed up the computation; another visualization routine that allow us to tentatively distinguish shocks regions by means of the velocity divergence $\nabla \cdot \mathbf{u}$; or routines that can apply masks to the numerical or observational data to isolate regions of interest.

- As part of the developed tools, we have also programmed a new Fortran module for the Bifrost code that speeds up the calculations that include ambipolar diffusion. In Chapter 5, we provide details about this new module, besides the validation test and some preliminar results.

1.4.3 Supercomputing facilities

Since realistic experiments are demanding in terms of computing resources, in this thesis we have used three different supercomputing facilities to carry out the numerical simulations.

- *MareNostrum*
  MareNostrum is the generic name that the Barcelona Supercomputing Center (BSC) uses to refer to the different updates of the most powerful supercomputer in Spain and among the top supercomputing facilities in Europe. In the thesis, two versions have been used to perform our numerical experiments: MareNostrum3, which contained 48,896 Intel Sandy Bridge processors and reached the 129th position (2013) of the

most powerful computers in the world according to the Top500 list[1]; and the current MareNostrum4, whose main general-purpose block has a total of 165,888 Intel Xeon Platinum processors and is in the 16th position of the Top500.
`https://www.bsc.es/marenostrum/marenostrum`

- *Teide-HPC*
  Teide-HPC (High Performance Computing) is the second most powerful supercomputer in Spain. Located in Tenerife (Spain), it belongs to the Instituto Tecnológico y de Energías Renovables (ITER). With 17,800 Intel Sandy Bridge computing cores, during the first years of the thesis, it appeared in the 169th position (June 2014) within the Top500 list.
  `http://teidehpc.iter.es/en`

- *LaPalma*
  Located in the island of La Palma (Spain), it is a supercomputer installation belonging to the IAC and one of thirteen nodes that form the Spanish Supercomputing Network (RES). In the course of the thesis, two versions have been used: LaPalma2, with 2048 IBM PowerPC 970MP processors; and the current one, LaPalma3, with 4032 cores Intel Xeon E5-2670.
  `http://www.iac.es/sieinvens/SINFIN/Main/supercomputing.php`

1.4.4 Observational data

The observational data used in this thesis were obtained with the following instruments.

- *IRIS*
  The Interface Region Imaging Spectrograph (IRIS; De Pontieu et al., 2014) is a NASA small explorer mission developed and operated by Lockheed Martin Solar and Astrophysics Laboratory (LMSAL) launched on 27 June 2013. It is able to scan the chromosphere, transition region, and corona with $0.33 - 0.4$ arcsec spatial resolution, 2 s temporal resolution, and 1 km s^{-1} in terms of Doppler shifts. In particular for this thesis, the IRIS observational dataset consists of spectral information obtained through a medium-dense raster, and images by means of slit-jaw images (SJI) of C II 1330, Si IV 1400 and Mg II k 2796 Å.

- *SST*
  The Swedish 1-m Solar Telescope (SST, Scharmer et al., 2003) is operated on the island of La Palma by the Institute for Solar Physics (ISP) of Stockholm University in the Spanish Observatorio del Roque de los Muchachos of the Instituto de Astrofísica de Canarias. It has installed an spectropolarimeter called CRISP (Scharmer et al., 2008),

[1] `https://www.top500.org/`

which includes a dual Fabry-Pérot interferometer that is able to make fast wavelength tuning within a spectral region that samples the chromosphere and photosphere. The observational dataset used in this thesis contains Ca II 8542 Å and Hα 6563 Å spectral scans, and photospheric polarization maps obtained by adding the Stokes V maps of the 3 outer spectral positions in both wings of the Ca II 8542 line.

1.5 Outline of this thesis

The thesis is structured in four chapters that deal with various open questions described in Section 1.3 and a final one with the main conclusions. The layout is as follows:

1. In Chapter 2, we provide a new perspective of surges introducing, for the first time together, thermal conduction, photospheric and chromospheric radiative transfer, optically thin radiative cooling, and a realistic equation of state (EOS) in a numerical simulation of this kind. We present results from a 2.5D numerical experiment carried out with Bifrost where a surge is obtained as a by-product of magnetic flux emergence and reconnection. Through detailed Lagrangian tracing, we evaluate the role of the different entropy sources. Additionally, other relevant aspects such as plasmoid formation, mechanisms of acceleration and shocks are studied in relation to the surge formation.

2. Chapter 3 is devoted to the interpretation of observations through comparison with our models. We use coordinated observations from space and the ground with IRIS and SST to study a simultaneous episode of an Hα surge and a Si IV burst, finding emission of Si IV within the surge. Additionally, we compute spectral synthesis from our numerical experiments, with spatial and spectral degradation to mimic the observational conditions, focusing on the transition region IRIS spectral line Si IV 1402.77 Å.

3. In Chapter 4, we address other limitation in the realism of surge modeling: the lack of equilibrium in the ionization/recombination processes. Specifically, we focused on the nonequilibrium ionization of silicon and oxygen to provide theoretical support to observations and explain why surges are natural sites to show enhanced emissivity in transition region lines. Furthermore, we analyze LOS effects due to the involved geometry of the surge.

4. In Chapter 5, we present the implementation, testing, and first results of a new Fortran module in the Bifrost code that calculates the ambipolar diffusion term of the General Ohm's Law (GOL) in an efficient way through the Super Time-Stepping (STS) method (Alexiades et al., 1996).

5. Finally, Chapter 6 contains a summary of the main conclusions of this thesis and the perspective of the surge phenomenon in the near future.

2

The cool surge following flux emergence in a radiation-MHD experiment

The aim of this chapter of the thesis is to analyze and understand the physics of the formation and evolution of the surges using a realistic treatment of the material plasma properties and of the radiation transfer for the layers from the top of the solar interior to the corona. This is the first time that such realistic modeling is attempted in this sort of experiments. The numerical tool used is the Bifrost code, which, as described in Section 1.4.1, has a realistic multi-component EOS as well as advanced modules for photospheric and chromospheric radiation transfer, heat conduction and optically-thin radiative cooling in the corona. We have performed a 2.5D radiative-MHD numerical experiment of the emergence of a twisted magnetic tube through the granular and mesogranular convection layer beneath the surface and into the atmosphere. The time evolution of the system leads to the ejection of part of the emerged material as a cool and dense surge. Thanks to this modeling approach, a new perspective of the morphology, dynamics and time evolution of the surge is obtained with a degree of detail that allows direct comparison of the theoretical results with observations: the comparison is then carried out in the following chapters of the thesis.

The main results and conclusions of this chapter are summarized in the following:

- The rise of the magnetic tube through the convection zone up to the surface shows resemblances with previous experiments of magnetic flux emergence. In the initial stages, it starts to develop a dumbbell shape (Emonet & Moreno-Insertis, 1998), and then, the convection flows deform and break the tube in different fragments (e.g., Cheung et al., 2007; Martínez-Sykora et al., 2008; Tortosa-Andreu & Moreno-Insertis, 2009). Some of those fragments are able to reach the surface and pile up magnetized plasma in the surface. As a consequence, the granular pattern is modified and anomalous granules appears similar to what is found in observations (Guglielmino et al., 2010; Ortiz et al., 2014). When enough magnetic field is gathered, a buoyancy instability is promoted (Newcomb, 1961), allowing the magnetized plasma to go up into higher

layers of the atmosphere. This emerged material forms a structure akin to a dome (see, e.g., Yokoyama & Shibata, 1996, Archontis et al., 2004, Moreno-Insertis & Galsgaard, 2013 and references therein) and non-stationary magnetic reconnection between the emerged region and the preexisting magnetic field takes place. As a by-product of the magnetic reconnection process, a hot jet and a surge are obtained.

- Through extensive Lagrange tracing of the mass elements of the surge, we analyze their evolution and, in particular, the role of the entropy sources. We have been able to distinguish four different plasma populations that contribute to the surge, some of which cannot be obtained in more idealized experiments like those of Yokoyama & Shibata, 1996, Nishizuka et al., 2008, Jiang et al., 2012, Moreno-Insertis & Galsgaard, 2013. This is because thermal conduction and optically thin losses are key mechanisms in the surge evolution. In fact, one of those populations that can not be obtained with a proper thermodynamical treatment, reaches high temperatures, between TR ($\sim 10^5$ K) up to coronal ($\sim 10^6$ K) temperatures, typically when going through the current sheet, but is then brought back down to classical surge temperatures of order 10^4 K thanks to the action of the radiation losses and thermal conduction terms. That population covers up to 34% of the surge cross section at the time of maximum development, i.e., an important fraction of the phenomenon is missed in idealized experiments. Moreover, the plasma elements of that population are located in the boundaries of the surge surrounding cooler plasma and, as we see in the following chapters, they constitute an important source of UV emission.

  The finding that a significant fraction of the plasma in the surge suffers heating/cooling processes that makes it reach high temperatures for part of its life may also be of interest concerning its observational detection. Additionally, an adequate treatment of the entropy sources and sinks in the energy equation, besides being important when studying the formation and time evolution of surges, may also apply to other cool ejections such as the macrospicules.

- Thanks also to the Lagrangian tracing, we are able to study in detail the acceleration mechanisms and provide further explanations besides the overused *slingshot effect* mentioned in Section 1.2.2. In the launch phase, the surge originates from a peeling mechanism that mostly drags chromospheric plasma from the emerged dome. In that phase, many elements suffer accelerations well in excess of the solar gravity because of the Lorentz force and, to a lesser extent, the pressure gradient. Although the acceleration values may seem quite large, an elementary calculation shows that sustained accelerations of several times the solar gravity ought to be expected in this kind of phenomenon. After the launch phase, the surge shows oscillating behavior resembling a swaying finger. When nearing the apex of their individual trajectories, the plasma elements of the surge follow quasi-parabolic trajectories with acceleration close to solar gravity. In the numerical experiments, both the launch and decay of the surge show similarities with the morphology and kinematics seen in observations.

- Studying the jumps in different quantities, it is found that the formation of the surge

and hot jet is mediated by a structure far from the reconnection site composed of two strong shocks: one of them is located at the base of the hot jet and resembles a switch-off slow shock; the other is a nearly perpendicular shock that leads to the detachment of the surge from the original emerged plasma dome.

The above results and conclusions were published by Nóbrega-Siverio et al. (2016) in May 2016 in the volume 822 of *The Astrophysical Journal (ApJ)* with the title **The Cool Surge Following Flux Emergence in a Radiation-MHD Experiment**. This paper is attached in the following pages and can also be found in the ADS:
`http://adsabs.harvard.edu/abs/2016ApJ...822...18N`

The Astrophysical Journal, 822:18 (14pp), 2016 May 1 doi:10.3847/0004-637X/822/1/18

THE COOL SURGE FOLLOWING FLUX EMERGENCE IN A RADIATION-MHD EXPERIMENT

D. Nóbrega-Siverio[1,2], F. Moreno-Insertis[1,2], and J. Martínez-Sykora[3,4]
[1] Instituto de Astrofisica de Canarias, Via Lactea, s/n, E-38205 La Laguna (Tenerife), Spain; dnobrega@iac.es, fmi@iac.es
[2] Department of Astrophysics, Universidad de La Laguna, E-38200 La Laguna (Tenerife), Spain
[3] Lockheed Martin Solar and Astrophysics Laboratory, Palo Alto, CA 94304, USA; juanms@lmsal.com
[4] Bay Area Environmental Research Institute, Petaluma, CA, USA
Received 2015 November 19; accepted 2016 January 14; published 2016 April 27

ABSTRACT

Cool and dense ejections, typically Hα surges, often appear alongside EUV or X-ray coronal jets as a result of the emergence of magnetized plasma from the solar interior. Idealized numerical experiments explain those ejections as being indirectly associated with the magnetic reconnection taking place between the emerging and preexisting systems. However, those experiments miss basic elements that can importantly affect the surge phenomenon. In this paper we study the cool surges using a realistic treatment of the radiation transfer and material plasma properties. To that end, the Bifrost code is used, which has advanced modules for the equation of state of the plasma, photospheric and chromospheric radiation transfer, heat conduction, and optically thin radiative cooling. We carry out a 2.5D experiment of the emergence of magnetized plasma through (meso) granular convection cells and the low atmosphere to the corona. Through detailed Lagrange tracing we study the formation and evolution of the cool ejection and, in particular, the role of the entropy sources; this allows us to discern families of evolutionary patterns for the plasma elements. In the launch phase, many elements suffer accelerations well in excess of gravity; when nearing the apex of their individual trajectories, instead, the plasma elements follow quasi-parabolic trajectories with accelerations close to $g_\odot$. We show how the formation of the cool ejection is mediated by a wedge-like structure composed of two shocks, one of which leads to the detachment of the surge from the original emerged plasma dome.

Key words: magnetohydrodynamics (MHD) – methods: numerical – Sun: atmosphere – Sun: chromosphere – Sun: corona – Sun: flares

Supporting material: animations

1. INTRODUCTION

Cool, chromospheric-temperature ejections are key dynamical elements of the solar atmosphere. Surges, in particular, usually appear in connection with magnetic flux emergence episodes, where they are often associated with hot, high-speed EUV or X-ray jets. Even though observationally known for several decades now, the theoretical understanding of the surges has progressed slowly, and there are still many unsolved questions. First detections of chromospheric surges date back to the 1940s, when they were described as Hα absorption markings related with bright eruptions (flares) corresponding to outward velocities followed by inward motion (Ellison 1942; Newton 1942). Further observational properties were obtained in the 1970s and 1980s (Kirshner & Noyes 1971; Roy 1973; Cao et al. 1980; Schmieder et al. 1984, among others): the surges were seen as blue and redshifted absorptions in Hα that typically have a length of 10–50 Mm, and line-of-sight velocities of a few to several tens of km s^{-1}, reaching, in extreme cases, 100–200 Mm and 200 km s^{-1}, respectively. The surges were also observed in Ca II (Rust 1976); a close relationship between Hα surges and EUV ejections was found as well (Schmahl 1981). Later, different observations focused on the role of the magnetic field, suggesting that the Hα surges could be an indirect result of flux emergence processes and the interaction (possibly reconnection) of the upcoming magnetized plasma with the ambient coronal field (Kurokawa & Kawai 1993; Schmieder et al. 1995; Canfield et al. 1996; Chae et al. 1999). Those suggestions were based mainly on the detection of the cool ejections next to emerging bipolar regions and quasi-simultaneously with hot coronal plasma jets (observed in the EUV or in X-rays). The high resolution observations of the past decade (e.g., Yoshimura et al. 2003; Jibben & Canfield 2004; Brooks et al. 2007; Jiang et al. 2007; Uddin et al. 2012; Vargas Domínguez et al. 2014) have provided further evidence for the frequent relation between magnetic flux emergence, chromospheric ejections and hot jets. Other chromospheric-temperature ejections, such as macrospicules, show some analogies with the surges: they are multithermal structures observed mainly in He II 304 Å and Hα, with a cool core surrounded by a thin sheath of 1–2 $\times$ 10^5 K (e.g., Bohlin et al. 1975; Habbal & Gonzalez 1991; Pike & Harrison 1997; Madjarska et al. 2006; Bennett & Erdélyi 2015).

Concerning the theoretical effort, the seminal paper by Heyvaerts et al. (1977; see also Forbes & Priest 1984) discussed how the emergence of magnetized plasma from the solar interior could lead to a conflict of magnetic orientation with the preexisting coronal field, and hence to reconnection and the ejection of hot plasma. Using this flux emergence paradigm, Shibata et al. (1992) and Yokoyama & Shibata (1995, 1996) then showed, through a 2.5D numerical model with an initial uniform coronal field, that cool plasma could be ejected next to a hot jet as a consequence of the emergence of magnetic flux from the interior. The authors tentatively identified those cool ejections with Hα surges and described them as resulting from *the sling-shot effect due to reconnection, which produces a whip-like motion* (Yokoyama & Shibata 1996). Their cool surge had a density around 10^{-11} g cm^{-3}, speeds in the range $\approx$50–90 km s^{-1}, and a maximum vertical size of several megameter. Nonetheless, due

to the computational limitations of the time, the corona used in the experiment had unrealistic values of density and temperature. Using the same sort of setup, but with more realistic coronal parameters, Nishizuka et al. (2008), through morphological image comparisons, suggested that the cool ejections associated with flux emergence could be the cause for the jet-like features seen in Ca II H + K observations. The more recent flux-emergence experiment of Jiang et al. (2012) had a canopy-type configuration of the ambient coronal magnetic field, and also led to the ejection of cool and hot plasma. A study of the cool ejection in three-dimensions following magnetic flux emergence has only recently been published (Moreno-Insertis & Galsgaard 2013). This experiment yielded a cool (from 10^4 K to a few times 10^5 K) and dense (between 10^{-12} and 10^{-13} g cm^{-3}) wall-like plasma domain surrounding the emerged flux region. Through Lagrange tracing, the authors explained the formation of the wall through plasma, which was being transferred from the emerged region attached to field lines that change connectivity in the main reconnection site. The cool ejecta had speeds of typically less than 50 km s^{-1} and were not collimated. Similar surge speeds were found by MacTaggart et al. (2015) in 3D flux emergence experiments for a variety of magnetic configurations.

All of those theoretical models, whether 2D or 3D, have been helpful in providing basic indications for the mechanisms that may lead to the simultaneous ejection of cold and hot plasma; nevertheless, they lack essential physical processes relevant in the photosphere, chromosphere, and corona, and can therefore only be taken as first steps when trying to understand the physics of the surges. The aim of this paper is to provide a new perspective of the cool ejections introducing some of those physical processes, like thermal conduction, photospheric and chromospheric radiative transfer, optically thin radiative cooling, and a realistic equation of state (EOS). To that end, we use the Bifrost code as computational tool (Gudiksen et al. 2011). For a first approach, in this paper we are using a 2.5D setup. The initial phase of the flux emergence process takes place through solar-like granular convection, which influences the sizes of the resulting structures in the low atmosphere. We can study the subsequent phenomena of reconnection and plasma ejection in the atmosphere with high temporal cadence and spatial resolution, focusing on the formation, maximum development, and decay phases of the surge. The study includes detailed Lagrange tracing of the mass elements in the surge, which allows us to analyze in detail their origin and thermal evolution, the role of the various entropy sources, and the acceleration mechanisms. We show that the cool and dense ejection is a complex and fascinating phenomenon in which the entropy sources play an important role.

The layout of this paper is as follows. Section 2 describes the physical and numerical model. In Section 3 we show the initial phases of the experiment prior to the initiation of the cool ejection. Sections 4 and 5 analyze the surge in detail through its various phases (ejection, detachment, and decay), focusing on the heating sources, kinematics, and dynamics of the plasma elements. Finally, Section 6 contains the discussion and the summary.

2. THE PHYSICAL AND NUMERICAL MODEL

2.1. The Numerical Code

The experiment we present in this paper was run using the radiation-magnetohydrodynamics (RMHD) Bifrost code (Gudiksen et al. 2011). This code includes thermal conduction along the magnetic field lines and radiation transfer adequate to the photosphere, chromosphere, and corona; it takes into account entropy sources such as Spitzer thermal conductivity, optically thin cooling, and radiative losses by neutral hydrogen, singly ionized calcium, and magnesium, among others; details are provided in the papers by Skartlien (2000), Hayek et al. (2010), Gudiksen et al. (2011), Leenaarts et al. (2011), and Carlsson & Leenaarts (2012). The code also has an EOS that includes the ionization/recombination of the relevant atomic species. On the other hand, because of the validity range of the radiation tables in the code, there is an ad hoc heating term that forces the plasma to stay above $T = 1660$ K (a discussion in detail concerning this term can be found in the paper by Leenaarts et al. 2011). The advantages of the Bifrost code probably make the simulation in this paper the most realistic one to date for the formation and dynamics of surges (but see the discussion concerning various limitations of the present model in Section 6.3).

The description of the model underlying our experiment is divided into two parts: (1) the background stratification, numerical grid, and boundary conditions and (2) the twisted magnetic tube.

2.2. Background Stratification, Numerical Grid and Boundary Conditions

Concerning the background stratification, we started from a preexisting statistically stationary magnetoconvection configuration that includes, in a self-consistent manner, the uppermost layers of the solar interior, the photosphere, the chromosphere, the transition region, and the corona. The convection patterns range between granular and mesogranular. The corona has a temperature of about 1 MK and a quasi-uniform vertical magnetic field of 10 G in order to mimic a coronal hole medium. The initial magnetic field is contained in the $x - z$ plane, with z being the vertical coordinate. The left panel in Figure 1 shows the horizontal averages for our initial condition for density ρ, gas pressure P_g, and temperature T; all of them normalized to their photospheric values at $z = 0$ Mm, namely, $\rho_{\rm ph} = 3.09 \times 10^{-7}$ g cm^{-3}, $P_{g_{\rm ph}} = 1.11 \times 10^5$ erg cm^{-3} and $T_{\rm ph} = 5.62 \times 10^3$ K. In the right panel we present a 2D temperature map where a number of magnetic field lines have been superimposed in black. In the image, the granulation pattern is distinguishable through the vertical field concentrations in the convective downflows and through the horizontal field lines in the center of the granules in the photosphere.

The physical domain is $0.0\,{\rm Mm} \leqslant x \leqslant 16.0\,{\rm Mm}$ and $-2.6\,{\rm Mm} \leqslant z \leqslant 14.4\,{\rm Mm}$, with $z = 0$ Mm corresponding to the solar surface, or more precisely, to the horizontal level where $\langle \tau_{500} \rangle = 1$. The numerical box has 512×512 points in the (x, z) directions, respectively. The grid is uniform in the x-direction with $\Delta x = 31$ km, and non-uniform in the vertical direction in order to better resolve the lower photosphere. The vertical grid spacing varies between 19 km, reached in the photosphere and chromosphere, and 90 km at the top and bottom of the domain. The boundary conditions are periodic in the horizontal direction. At the top of the box characteristic boundary conditions (as described by Gudiksen et al. 2011) have been chosen that suppress incoming waves so as to eliminate any signal reflexion while the plasma can leave the domain. Additionally, the corona is expected to have temperatures of order 1 MK but the two-dimensional nature

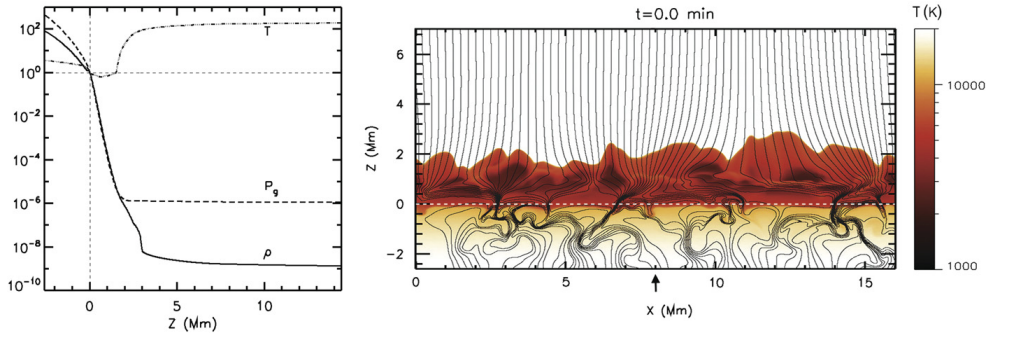

Figure 1. Left: horizontal averages for density ρ, gas pressure P_g, and temperature T for the initial stratification. The values are normalized to their photospheric values at $z = 0$ Mm, namely, $\rho_{\rm ph} = 3.09 \times 10^{-7}$ g cm^{-3}, $P_{\rm gph} = 1.11 \times 10^5$ erg cm^{-3}, and $T_{\rm ph} = 5617$ K. The dotted horizontal line delineates the unity and the vertical one, the solar surface. Right: temperature map for the initial background stratification for heights between $z = -2.3$ Mm and $z = 7.0$ Mm. Magnetic field lines appear superimposed in black. The inflow region where the tube has been injected is at $x = 8$ Mm (black arrow). The solar surface is roughly at $z = 0$ Mm (dashed horizontal white line).

of this experiment prevents a self-consistent magnetic heating resulting from photospheric field line braiding, as in the 3D experiment of Gudiksen & Nordlund (2005). To alleviate this problem, a *hot-plate* is implemented at the top boundary, meaning a Newton cooling term that forces the temperature in the boundary cells to stay fixed at 10^6 K. For the bottom boundary the code uses a technique often implemented in magnetoconvection simulations (e.g., Stein & Nordlund 1998; Hansteen et al. 2007), namely, it keeps the bottom boundary open so that plasma can go across it, and constant entropy is set in the incoming material to keep the convection going, while the rest of the variables is extrapolated.

2.3. The Twisted Magnetic Tube

In order to produce magnetic flux emergence, we inject a twisted magnetic tube with axis pointing in the y-direction, the ignorable coordinate in this 2.5D experiment. The injection is done through the lower boundary of the box following the method described by Martínez-Sykora et al. (2008). The longitudinal and transverse components of the magnetic field in the tube have the canonical form of a Gaussian profile with an r-independent pitch (e.g., Fan 2001),

$$B_y = B_0 \exp\left(-\frac{r^2}{R_0^2}\right), \quad (1)$$

$$B_\theta = q\, r\, B_y, \quad (2)$$

where r and θ are the radial and azimuthal coordinates relative to the tube axis, R_0 is a measure for the tube radius, q a constant twist parameter, and B_0 the magnetic field in the tube axis. To favor the emergence, we inject the tube in an inflow region, namely $x_0 = 8.0$ Mm (marked with a black arrow in the right panel of Figure 1). The rest of the parameters are selected within the ranges that lead to a coherent emergence pattern at the surface; the chosen values are presented in Table 1. The initial axial magnetic flux is $\Phi_0 = 1.5 \times 10^{19}$ Mx, which is in the range of an ephemeral active region (Zwaan 1987). This magnetic field configuration has positive helicity. The field lines have pitch $\Delta y_p = 2\pi/q = 2.6$ Mm independently of the radius. In other words, all field lines execute two turns around the axis along a distance of 5.2 Mm.

Table 1
Parameters of the Initial Twisted Magnetic Tube

x_0 (Mm)	z_0 (Mm)	R_0 (Mm)	q (Mm^{-1})	B_0 (kG)
8.0	−2.9	0.16	2.4	19

3. INITIAL PHASES

We call *initial phases* the time interval when the injected magnetic flux is rising through the convection zone and the photosphere until it reaches the low corona, or more precisely, until an emerging plasma dome is formed, as explained in Section 3.3. The initial phases share similarities with previous RMHD experiments of magnetic flux emergence (Cheung et al. 2007; Martínez-Sykora et al. 2008; Tortosa-Andreu & Moreno-Insertis 2009) and also with more idealized MHD experiments (Yokoyama & Shibata 1996; Fan 2001; Magara 2001; Archontis et al. 2004; Moreno-Insertis et al. 2008; Moreno-Insertis & Galsgaard 2013). Figure 2 illustrates the module of the magnetic field, B, at four different instants of the initial phases. In the following, we explain the different panels of the figure.

3.1. Emergence Through the Convection Zone

The first stage of the rise of the magnetic tube is an expansion away from the injection point with velocities of order 1 km s^{-1}. As the tube rises through the convection zone, it starts to develop a dumbbell shape that is easily identifiable because of the high field concentration on either side of the tube axis, panel (A) in Figure 2. Afterwards (Panel (B)), the action of the convection flows on the rising tube starts to be evident. They deform and break the twisted magnetic tube into smaller fragments in the regions of strong shear, typically where the downflows hit the tube. We can identify five large fragments during the emergence process. One of the fragments of the tube, the one tagged "(1)" in panel (C), reached the surface approximately 35 minutes after the initiation of the

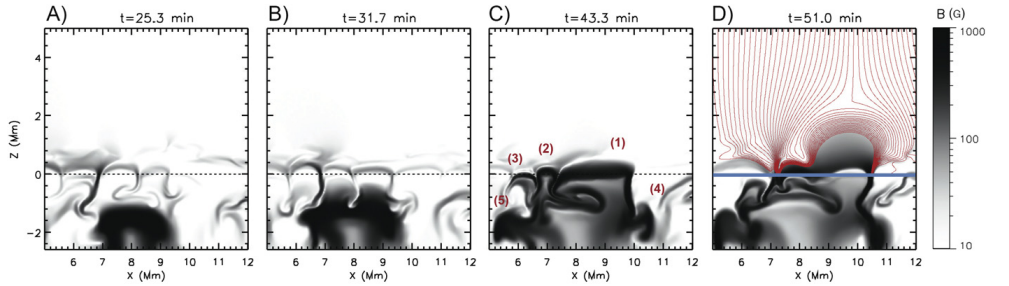

Figure 2. Gray-scale maps of the magnetic field strength for the initial phases of the experiment. The horizontal dashed line corresponds to the solar surface. In panel (C), we have indicated with labels 1 through 5 the different fragments resulting from the initial tube. Panel (D) is subdivided into two parts, above and below the thick blue line: magnetic field lines are superimposed in red, but only in the upper subpanel, to avoid blurring the structures of the interior.

experiment. At that instant, this fragment had a horizontal size of 1.3 Mm, i.e., on the order of a granular size. Two further pieces, "(2)" and "(3)", get to the surface at $t \sim 38$ and 43 minutes respectively, although they are smaller than the previous one. The fragments labeled "(4)" and "(5)" were strongly braked and pushed down by the convection downflows, and they do not reach the surface. Most of the eruptive phenomena observed in the atmosphere after the emergence are associated with the first fragment, so we focus attention onto it in the following.

3.2. Anomalous Granulation and Buoyancy Instability

Once in the photosphere, in the transition between super- and sub-adiabatically stratified regions, the magnetized plasma starts to pile up, consequently increasing the magnetic pressure. The enhanced pressure produces a sideways growth of the fragment leading to an anomalous granule of about 2.6 Mm horizontal extent (Figure 2, panel (C), $x = 7.4$–10 Mm), which is twice the size it had when it reached the surface. Similar anomalous granulation related with flux emergence was found in the numerical experiments by Cheung et al. (2007), Martínez-Sykora et al. (2008), and Tortosa-Andreu & Moreno-Insertis (2009), and in the observations by Orozco Suárez et al. (2008), Guglielmino et al. (2010), and Ortiz et al. (2014), among others. The later evolution of the anomalous granule occurs in the frame of the buoyancy instability (Newcomb 1961), along the general lines described by Tortosa-Andreu & Moreno-Insertis (2009) and, to some extent, also in idealized models without radiation (see Magara 2001; Archontis et al. 2004; Moreno-Insertis 2006; Murray et al. 2006). In all those cases the development of the instability allows the magnetized plasma to rise well above the photospheric heights.

3.3. The Emerged Magnetized Dome

Following the buoyancy instability, the plasma belonging to the anomalous granule suffers a rapid expansion into the atmosphere with radial velocities of 15 km s^{-1} at heights around 1–2 Mm. This expansion leads to the classical dome (or mountain) formation already found in the past (see, e.g., Yokoyama & Shibata 1996; Archontis et al. 2004; Moreno-Insertis & Galsgaard 2013 and references therein). In panel (D) of Figure 2 we show the early stages of the emerged dome between $z = 0$ Mm and $z = 2$ Mm approximately. In the upper subpanel (above $z = 0$, marked by a thick horizontal line in blue), magnetic field lines are shown superimposed in red: they are seen to collect into compact field line bunches at the location of photospheric downflows. One of those bunches is located at $x \approx 7.2$ Mm; the region between those lines and the left side of the dome corresponds to a current sheet that is described in Section 3.4.

As the dome expands, its plasma temperature decreases significantly, reaching the lower limit allowed in our simulation explained in Section 2. This is expected for expansion phenomena in the chromosphere (e.g., Hansteen et al. 2006; Martínez-Sykora et al. 2008; Tortosa-Andreu & Moreno-Insertis 2009; Leenaarts et al. 2011). Simultaneously, the dome interior suffers a draining process owing to the gravitational flows that take place along the loop-like magnetic field lines, as described by Moreno-Insertis & Galsgaard (2013). The combination of the expansion and the draining produces a density change from the values during the first stages of the dome evolution (10^{-11} to 10^{-12} g cm^{-3}) to values on the order of 10^{-14} g cm^{-3} in later phases.

3.4. The Current Sheet: Unsteady Reconnection

The expansion of the dome pushes its magnetic field against the preexisting vertical coronal magnetic field. This generates an orientation conflict on the left-hand side of the dome, giving rise to a thin concentrated current sheet. In Figure 3, we illustrate the latter using as inverse characteristic length of the magnetic field variation the quantity

$$L_B^{-1} = \frac{|\nabla \times \boldsymbol{B}|}{|\boldsymbol{B}|}. \quad (3)$$

This quantity permits good visualization of any abrupt change of B. For comparison, in a pure rotational discontinuity of the field, $L_B{}^{-1}$ is π times the inverse width of the sheet, while in a Harris sheet it goes through infinity at the center of the sheet. In the figure, the pixels where $L_B < 1000$ km are shown in color, with magnetic field lines superimposed as solid lines. There is a reconnection site located at $x \sim 6.8$ Mm and $z \sim 1.8$ Mm (black cross). Along its lifetime, the current sheet repeatedly experiences the formation of plasmoids (like the one at $z \sim 2.4$ Mm in Figure 3) through the development of the tearing-mode-instability (Furth et al. 1963). This behavior has been detected in previous flux emergence experiments, e.g., in 2D by Yokoyama & Shibata (1996) and in 3D by Archontis

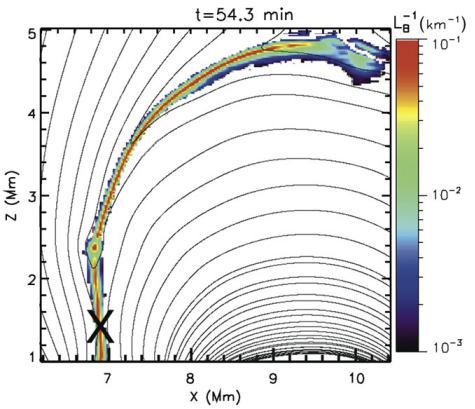

Figure 3. Map of the inverse characteristic length of the magnetic field L_B, see Equation (3), illustrating the thin current sheet at the boundary between emerged plasma and the corona. Only the pixels where $L_B < 1000$ km are shown in color. Magnetic field lines appear superimposed as solid lines. The black cross is the central part of the reconnection site.

et al. (2006), Moreno-Insertis & Galsgaard (2013), and Archontis & Hansteen (2014). In our case, the timescale of plasmoid formation is between several tens of seconds and a few minutes. This range is compatible with the theoretical value for the growth time of the tearing mode (see Goldston & Rutherford 1995): the latter is close to the geometric mean between $\tau_a = L_B/v_a$ and $\tau_d = L_B^2/\eta$, where v_a is the Alfvén velocity and η is the diffusivity. In our current sheet, $\tau_a = 10^{-2}$–10^{-3} s and $\tau_d = 10^{7}$–10^{8} s, and the geometric mean of those quantities is near the measured values in the experiment.

As time goes on, the area where the orientation conflict is located grows in length because of the dome expansion. During this phase, the plasmoids are ejected as part of the reconnection process, probably through the melon seed ejection mechanism (Schlüter 1957), which can be launched when there is an imbalance in the Lorentz force holding the plasmoid on its sides along the current sheet. Some of the plasmoids also merge forming bigger ones as a result of the coalescence instability (Finn & Kaw 1977).

4. THE EJECTION OF COOL, HIGH-DENSITY PLASMA

As a result of the reconnection process taking place at the boundary between emerged dome and coronal material, a substantial amount of plasma with chromospheric temperatures and densities is ejected to coronal heights. We refer to this phenomenon as the *cool and dense ejection* or *surge* and avoid the word *jet*, since the ejecta are not collimated and do not have large speeds, as shown in this section. In Figure 4, the overall evolution of the surge from the initial stages to the decay phase is illustrated using grayscale maps for the density and with a number of temperature contours with values indicated in panel (A). In panels (A) and (B) we can see an apparent peeling process that is carrying dense and cool plasma to greater heights toward the right of the dome. At the same time, a hot coronal jet is forming on the left side as can be identified through the pink contours in Panel (B). In panel (C), the dome seems to be splitting into two parts at $x \approx 12$ Mm. In panel (D), we can distinguish the cool and dense plasma ejection as the elongated structure located to the right of the emerged dome with temperatures below 3×10^4 K, i.e., chromospheric temperatures, including a colder core of lower temperatures down to 2×10^3 K. Around this instant, the ejecta reach their maximum height, $z = 13.2$ Mm, and the density range in the surge is between 10^{-14} and 10^{-11} g cm^{-3}. The rest of the panels (E), (F), (G), and (H) show the decay phase. During the decay, the surge moves first to the left and then to the right in a swaying motion caused by the Lorentz force associated with the bending of its magnetic field lines. The cool surge remains as an easily identifiable feature until $t \approx 66$ minutes, so its lifetime can be estimated to be about 7−8 minutes. The accompanying Movie 1 shows the time evolution of the density and temperature of the system.

In order to analyze the fundamental aspects of the surge, we have followed more than 3×10^5 plasma elements through Lagrangian tracing. The choice of tracers was carried out at the time of maximum vertical extent of the cool ejection, $t = 61$ minutes, and is shown in panel (I) of Figure 5 with dots of different colors superimposed on the image. We set the side and top boundaries of the surge to coincide with the isocontour $T = 3 \times 10^4$ K (blue curve) and use as lower limit the $z = 2$ Mm horizontal axis. The tracers are then evenly distributed in that domain with high-resolution spacing $\delta x = \delta z = 10$ km. For later reference, we have drawn the tracers in four different colors (cyan, yellow, purple, and red) according to the four different populations of plasma elements that are introduced and discussed from Section 4.1 onward. The resolution is high enough for the individual tracers to be indistinguishable in the figure: the domains looks like a continuous surface. Once the distribution is established, we follow the tracers backward in time until $t = 51$ minutes, to study their origin, and also forward, until $t = 65$ minutes. The tracking has a high temporal cadence of 0.2 s in order to reach good accuracy even in locations with high gradients and phases of fast changes, like when going through the current sheet.

The rest of this section is divided into three blocks devoted to the heating and cooling sources of the surge (Section 4.1), the plasma acceleration (Section 4.2), and the velocities, densities, and temperatures (Section 4.3).

4.1. Heating and Cooling Sources

Here we analyze the heat sources and sinks in the surge, since they are key for understanding its structure and evolution. From all the entropy sources included in the Bifrost code, the relevant ones for the surge are those resulting from the Spitzer thermal conductivity, the optically thin cooling, the radiative losses by neutral hydrogen, and the ohmic and viscous heating. The rest, like those associated with the chromospheric radiative losses by singly ionized calcium and magnesium, have much longer characteristic times and need not be discussed. The following results are focused on the rising phase of the ejecta until they reach their maximum height at around $t = 61$ minutes. Thereafter, the characteristic times of the heating and cooling processes become much longer than the general evolutionary timescale of the surge: the temperature changes in the decay phase are due to adiabatic compression.

The study of the thermal properties of the individual Lagrangian elements allows one to discern four different

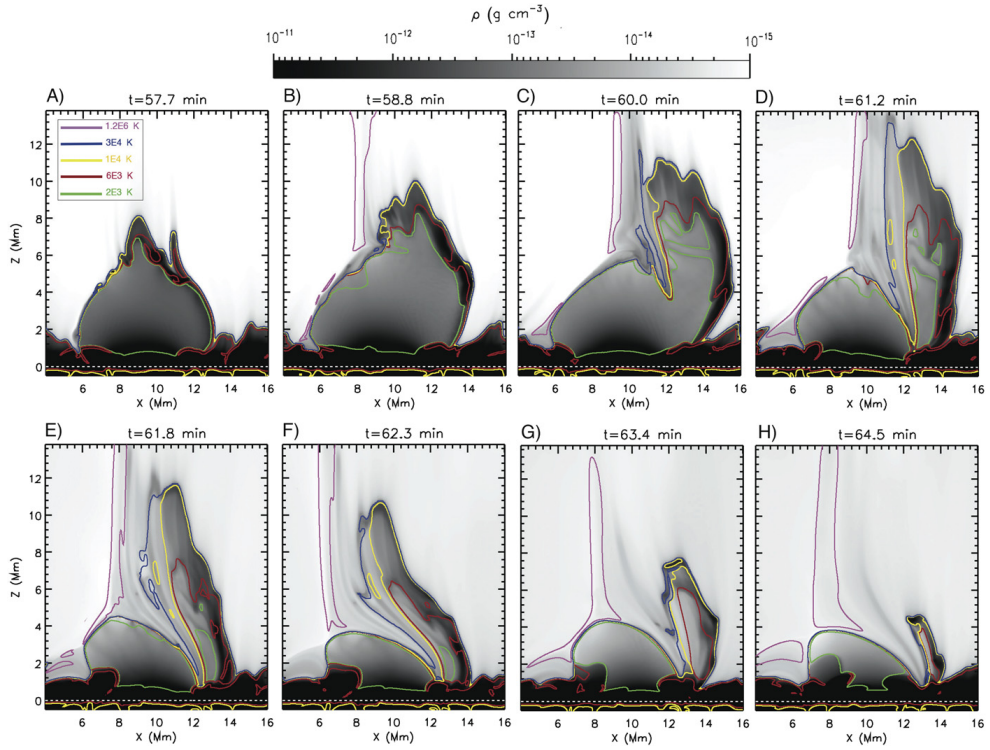

Figure 4. Density maps showing the formation and descending phases of the cool and dense ejection. Temperature contours have been superimposed to the maps to complete the image: the association of colors to temperatures is given in panel (A). The hot coronal jet is also visible on the left-hand side of the dome delineated by the pink contours.

(An animation of this figure is available.)

plasma populations within the ejecta of different origin and evolution that we have identified with labels "A", "B", "C", and "D", and drawn in colors cyan, yellow, purple, and red, respectively, in Figure 5. In Panel (I) we have already introduced the distribution of the Lagrangian elements when the cool ejection reaches its maximum height. Panels (II.1)–(II.4) show the evolution of those elements during previous stages of the surge. These panels illustrate the origin of the plasma in the surge and how the different populations evolve to give rise to the distribution shown in Panel (I). A more complete view of the formation of the surge is also provided via the accompanying Movie 2. The nature of the different populations is analyzed in the following.

4.1.1. Population A

Population A, plotted in cyan in Figure 5, corresponds to plasma originating in the dome (see panel (II.1)) and it is heated through Joule and viscous dissipation during the early stages of formation of the surge. Owing to the high density of this population, those entropy sources are not able to heat the plasma to values above 3×10^4 K. At $t = 61$ minutes, this population covers 44% of the cross section of the surge and its total mass per unit length in the y direction is 10^{-3} g Mm^{-1}. The top-left panel in Figure 6 shows with a black solid line the time evolution of the temperature of a representative plasma element of this population. The element jumps from dome temperatures, close to 2×10^3 K, to values around the temperature of the hydrogen ionization/recombination, namely 6×10^3 K. In the same panel (red curve), the values of $L_B{}^{-1}$ at the positions reached by that plasma element indicate that it passes near the current sheet, but not quite through it: the typical values of L_B in the current sheet are less than 100 km (see Figure 3).

4.1.2. Population B

The second group of Lagrange tracers is what we call Population B, drawn in yellow in Figure 5. Its defining feature is that the plasma elements in it, in spite of originating in the dome, reach temperatures between 10^5 and 10^6 K during the launch phase, and then cool down to temperatures below

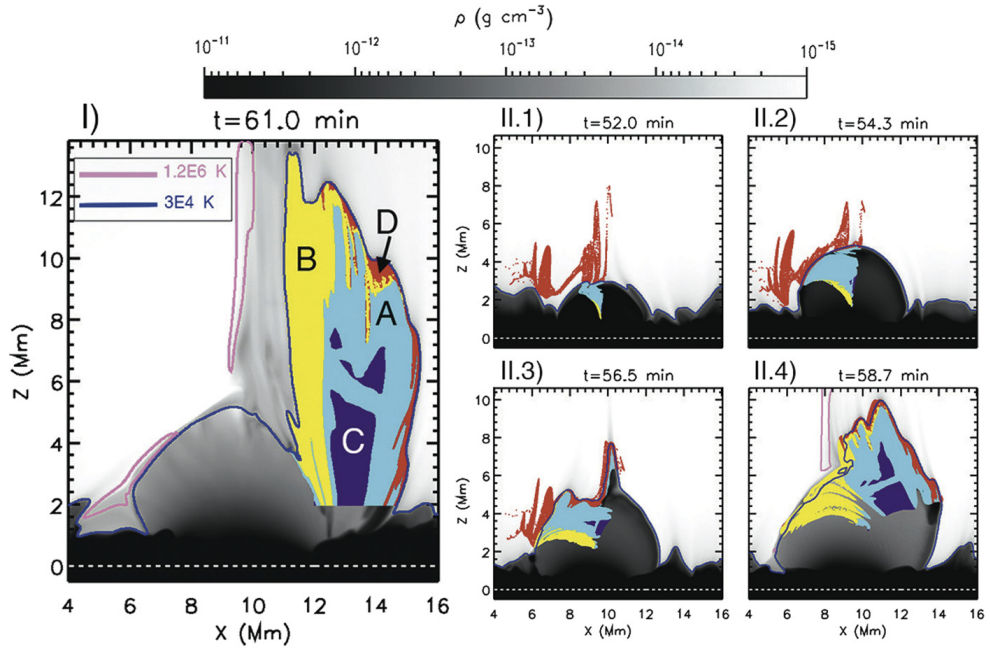

Figure 5. Panel (I): Density map showing the basic distribution of the more than 3×10^5 Lagrangian tracers by means of colored domains (cyan, yellow, purple, and red). The domains correspond to the four different populations discussed from Section 4.1 onward and are tagged with the corresponding capital letters. Panels (II.1) through (II.4): Evolution of the ensemble of tracers from time 52 minutes onward.

(An animation of this figure is available.)

3×10^4 K. This family leaves the dome later than the elements of population A, as shown in the panels (II.1)–(II.4) of Figure 5; it ends up covering 34% of the surge's cross section at $t = 61$ minutes, but it has comparatively low densities, so its integrated mass at that time is 4.7×10^{-5} g Mm^{-1} only. There are two main reasons for the sudden increase in temperature of the elements of this population, namely:

1. Unlike for Population A, some of its plasma elements pass through the current sheet, and are strongly heated there (see the yellow tracers above the blue temperature contour, 3×10^4 K, in panels (II.3) and (II.4)). The top-right panel in Figure 6 depicts an example of this behavior for a representative member of this population. The characteristic length L_B reaches a small value, around 25 km, after which it decreases, indicating that the plasma element is then leaving the current sheet. When in the current sheet, the Joule dissipation and, to a lesser extent, the viscous dissipation become highly efficient, with short characteristic timescales from several seconds to a few tens of seconds, as shown in the left panel of Figure 7.
2. Some plasma elements of this population, those close to the blue contour on the left side of the surge in panel (I) of Figure 5, are affected by their passage through a strong shock. This shock is a central feature of the dynamics of the surge and is described separately (Section 5).

Additionally to the foregoing, the heating processes are particularly effective at increasing the temperature of the particles of this population given their comparatively low initial density: their late ejection from the emerged dome implies that the density of the latter has already been substantially reduced through the gravitational draining explained in Section 3.3. The late ejection furthermore explains their appearance on the left hand side of the surge and with comparatively low density (see the left side of the surge in panel (D) of Figure 4 in comparison with its right side).

The short duration of the high temperature spurt of these mass elements is explained by the activation, when the temperature is nearing 10^6 K, of thermal conduction and optically thin radiative losses as effective entropy sinks. The associated characteristic times ($\tau_{\rm Spitz}$, $\tau_{\rm thin}$, respectively) for the plasma element studied above can be seen (Figure 7, right panel) to reach low values of several seconds ($\tau_{\rm Spitz}$) or of a few tens of seconds ($\tau_{\rm thin}$). When T decreases to values around 10^4 K, the radiative losses by neutral hydrogen can also be important (see the curve labeled $\tau_{\rm H}$). It is through these cooling processes that the elements of this population eventually adopt the cool temperatures of the surge.

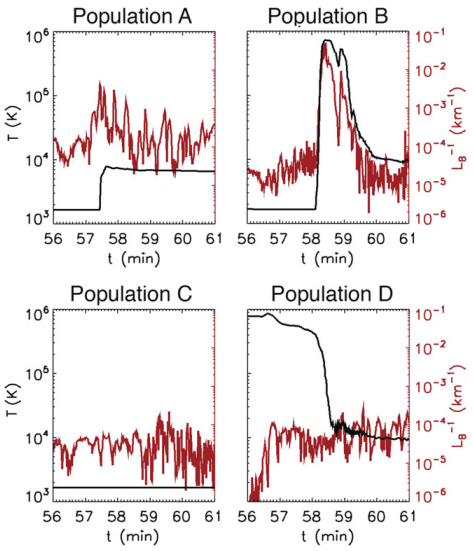

Figure 6. Set of panels showing the time evolution for four different plasma elements followed by Lagrangian tracing. The chosen elements are representative of the four different populations we found concerning the thermal properties. In the panels, the temperature T is plotted in in black while L_B^{-1} in red. This last quantity allows to identify the proximity of the element to the current sheet.

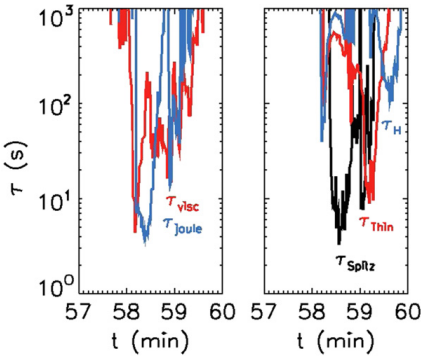

Figure 7. Characteristic times of the entropy sources and sinks for the representative plasma element of Population B used in Figure 6. Left panel: Joule ($\tau_{\rm Joule}$) and viscous ($\tau_{\rm visc}$) heating sources. Right panel: Thermal conduction ($\tau_{\rm Spitz}$), optically thin radiative losses ($\tau_{\rm thin}$), and radiative losses by neutral hydrogen ($\tau_{\rm H}$).

4.1.3. Population C

Population C, plotted in purple in Figure 5, is a fraction of the surge coming from the dome that maintains its initial temperature in the time range shown. At $t = 61$ minutes, this population covers 15% of the cross section of the surge and has a small mass content, 2.8×10^{-5} g Mm^{-1}. The Lagrangian tracing shows that the plasma elements were dragged passively from the dome, following the motion of the magnetic field lines explained in Section 4.2.1. Along this process, they are never heated by Joule or viscous dissipation. The local values of T and L_B^{-1} for a representative plasma element of this population are given in Figure 6, bottom-left panel. In fact, those plasma elements expand along their motion, which explains why this population is barely visible in panels (II.1) and (II.2) of Figure 5 in comparison with panels (II.3) and (II.4). The density of the elements decreases by approximately one order of magnitude, but their temperature is kept constant through the ad hoc heating term mentioned in Sections 2 and 6.3.

4.1.4. Population D

A small fraction of the Lagrange elements in the surge, plotted in red in Figure 5, have tracks that start in coronal heights at $t < 57$ minutes (panels (II.1)–(II.3)). The ensemble of such elements is called Population D in the following. They cover 7% of the cross section of the surge at $t = 61$ minutes (panel (I)). The temperature and L_B^{-1} evolution for a representative plasma element of this population is shown in the bottom-right panel of Figure 6. The tracks start at heights well above the reconnection site, with standard coronal temperature and density. When approaching the current sheet, though, these elements go through regions of large density gradients. The diffusion term included in the mass conservation equation becomes important, with characteristic timescale less than one minute, i.e., similar to the evolutionary time of the particles. The evolution that takes place then is effectively equivalent to a process of mixing across the density gradient with plasma elements coming from the dome, after which their behavior is equivalent to that of population A. This kind of effective mixing is peculiar of population D: the density diffusion term is small for the elements of the other populations. A proper study of the evolution of this population must therefore await a numerical experiment with much higher spatial resolution and correspondingly small numerical diffusion (see also the discussion in Section 6.3).

4.2. The Acceleration of the Surge

We turn now to the dynamics of the surge and study the acceleration of the plasma elements first during the launch phase (Section 4.2.1) and then when they are near the apex of their trajectory (Section 4.2.2).

4.2.1. Acceleration During the Launching Phase

The initial acceleration of the mass elements of the surge takes place when they are not far from the thin current sheet that covers the top-left region of the dome (Section 3.4). In this region, the Lorentz force may reach values well above gravity because of the high curvature of the magnetic field lines after reconnection. The gas pressure gradient may also reach large values because of the low values of the magnetic field at the center of the current sheet. For an estimate, call a_L and a_p the acceleration associated with those forces, use L_B as given in Equation (3) and define L_P as the corresponding length scale of variation of the gas pressure. One obtains

$$\left| \frac{a_L}{g_\odot} \right| = \frac{v_a^2}{2\, L_B\, g_\odot} \approx 18\, \frac{(v_a)^2_{100}}{(L_B)_{\rm Mm}}, \qquad (4)$$

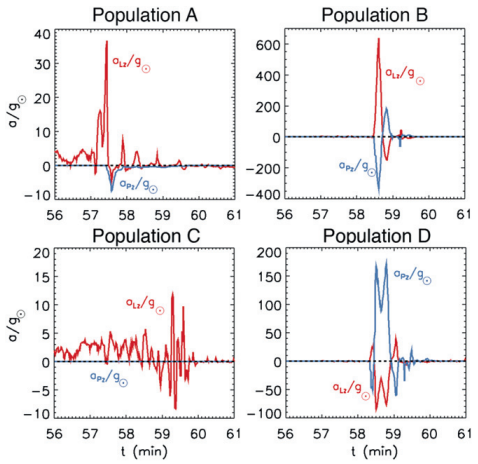

Figure 8. Vertical acceleration components a_{L_z} and a_{p_z} in units of $g_\odot$, in red and blue respectively, of the same representative plasma elements used in Figure 6. The panels illustrate the high acceleration of the plasma during the launch of the cool ejection.

$$\left|\frac{a_p}{g_\odot}\right| = \frac{c_s^2}{\gamma\, L_P g_\odot} \approx 22\,\frac{(c_s)^2_{100}}{(L_P)_{\rm Mm}}, \qquad (5)$$

where the subindices "100" and "Mm" indicate velocities measured in units of 100 km s^{-1} and lengths measured in macrometers, respectively, and v_a, c_s, $g_\odot$, and γ have their customary meaning (Alfvén and sound speed, solar gravity, and ratio of specific heats, respectively). In the reconnection region, the characteristic lengths are substantially smaller than 1 Mm and either the Alfvén velocity or the sound speed (or both) are of order 100 km s^{-1}. Equations (4) and (5) tell us, therefore, that a_L and a_p can easily exceed $g_\odot$; in fact, in some extreme cases they reach values of a few times 100 $g_\odot$ for a short period of time.

Figure 8 shows the vertical acceleration components a_{L_z}(red) and a_{p_z} (blue) for the representative Lagrangian elements used in Figure 6. We note the following behavior:

1. In Section 4.1.1 we saw how the elements of population A pass near, even though not quite through, the current sheet. In the top-left panel of Figure 6 we see how, in that phase, they are ejected by the Lorentz force with accelerations of tens of $g_\odot$. We also note the close relationship between the dynamic and thermodynamical changes (compare this panel with the corresponding one in Figure 6).
2. In the case shown in the top-right panel (population B), the element is ejected upward in a short time interval around $t = 58.5$ minutes. The acceleration values are extreme in this case, reaching $a_{L_z}/g_\odot = 6.4 \times 10^2$ and $a_{p_z}/g_\odot = -3.5 \times 10^2$ and last for about 10 s. Those values result from the fact that the element is going through the current sheet at that point and the characteristic lengths are correspondingly small, $L_B = 40$ km and $L_P = 50$ km (compare these lengths with those shown in Figure 3).

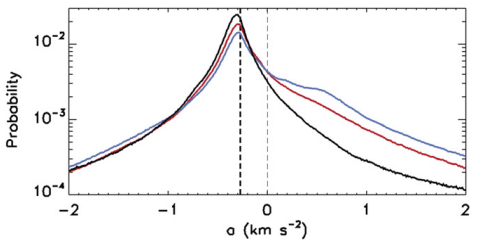

Figure 9. Histograms of the vertical accelerations for a time interval around the apex of the trajectories $|t - t_{\rm apex}| = 1$ minute (black curve), 2 minutes (red curve), and 3 minutes (blue curve). The vertical lines mark $-g_\odot$ (thick) and the zero acceleration value (thin). The statistical properties of these distributions are collected in Table 2.

3. The elements in Population C, like the one shown in the left-bottom panel, are the furthest away from the current sheet and their characteristic lengths are the largest ones. As a consequence, the acceleration values are lower than for other populations but are, anyway, typically a few to several times $g_\odot$. The plasma in this population is dragged by the magnetic field following the highly dynamical motion initiated in the current sheet and the gas pressure does not play any important role.
4. The right-bottom panel shows an element from Population D. The large pressure gradients in the boundary between the corona and the current sheet lead to a small characteristic length $L_P = 100$ km and to the predominance of a_{p_z} compared to a_{L_z}. The extreme values of the acceleration in this case are around $a_{L_z}/g_\odot = -0.8 \times 10^2$ and $a_{p_z}/g_\odot = 1.6 \times 10^2$, and last for about 20 s.

In the foregoing we have proved that the Lorentz force and gas pressure gradients in the region at and near the current sheet can easily cause substantial accelerations of tens to hundreds of $g_\odot$. This may seem quite large, but it is naturally associated with the fact that the plasma elements must jump by, in some cases, 6 Mm in height (from the top of the dome to the top of the resulting surge, check Figure 4) in a matter of, say, one minute. As an elementary calculation shows, sustained accelerations of several times $g_\odot$ (or impulsive accelerations of from tens to hundreds of times $g_\odot$) ought to be expected.

4.2.2. Acceleration Near the Apex of the Trajectories

We examine now the acceleration of the plasma elements during the central period of development of the surge, namely when the Lagrange elements are close to the apex of their trajectories. To do this, we call $t_{\rm apex}$ the time when each individual element reaches its maximum height and use $t - t_{\rm apex}$ as the time variable. Figure 9 contains three histograms for the vertical accelerations of the plasma elements for $|t - t_{\rm apex}| = 1$ minute (black curve), 2 minutes (red curve), and 3 minutes (blue curve). Additionally, we have carried out a statistical study using the sample of the vertical accelerations of all elements during the indicated time intervals with a cadence of 0.2 s. The basic moments of the statistical distribution and their mode are given in Table 2. The three distributions are highly peaked (positive kurtosis) and their most frequent value (the mode) is very near $-g_\odot$ in all cases. The mean of the most

Table 2
Statistical Moments of the Three Distributions of Figure 9

Curve	$t-t_{\rm apex}$ (minutes)	Mean/$g_\odot$	$\sigma_{\rm st\ dev}/g_\odot$	Mode/$g_\odot$
Black	[−1, 1]	−0.99	6.3	−1.1
Red	[−2, 2]	−0.48	6.6	−1.1
Blue	[−3, 3]	0.18	11.	−1.0

representative histogram (black curve) also coincides with $-g_\odot$. Yet, the distributions are not narrow, with standard deviations ranging from $6\,g_\odot$ to $11\,g_\odot$. Also: as wider time ranges around $t_{\rm apex}$ are chosen (red and blue curves), upward accelerations linked to the launch phase are more frequently represented and the mean of the distributions then shifts toward positive values.

4.3. Further Properties: Velocity, Temperature and Density.

We describe now some further properties of the ejecta: velocities, temperatures, and densities. Figure 10 contains double PDF plots for the vertical velocity u_z (upper row), and the density ρ (lower row) versus the temperature, T, of the Lagrangian elements. The panels illustrate representative phases of the surge: the launch phase ((A) panels); and the instant where the surge reaches its maximum vertical extent ((B) panels).

1. In the (A) panels we see that the majority of the plasma elements have cold temperatures (close to 2×10^3 K), densities around 10^{-13} g cm^{-3}, and velocities of a few tens of km s^{-1}: these are elements located in the dome at that time. Further, there is a group of elements clustered at a temperature of 6–7 thousand K, possibly near the phase of hydrogen ionization/recombination, with small, positive velocities also of tens of km s^{-1}. This group contains a mixture of elements that have reached that temperature either through heating of cold plasma (Population A) or cooling of hot plasma (Populations B and D) through the action of the different entropy sources. Additionally, in the density panel there are two extended tails of elements toward higher temperatures and velocities. Those elements correspond to, on the one hand, hot, low density Population-D plasma originating in the corona, and, on the other hand, denser plasma from Population B undergoing its heating-cooling phase. As we saw in Section 4.2.1, the elements of Populations B and D suffer the largest accelerations and, as a consequence, the range of velocities is between 20 and 150 km s^{-1}.
2. The (B) panels in the figure are representative of the phase of maximum vertical development of the ejection. We see that basically the whole ensemble is already falling, albeit with small velocities ($|u_z| < 30$ km s^{-1}). Concerning the temperatures, there is an important concentration of particles at the temperatures of hydrogen ionization/recombination (around 6×10^3 K), ionization/recombination of He I/He II (around $T\sim10^4$ K, label "4") and, to a lesser extent, of He II/He III (around $T\sim2\times10^4$ K, label "5")—see also the discussion about this issue in Section 6.3. The density range for this phase of the cool surge is between 10^{-14} and 10^{-11} g cm^{-3}. In the later phases of the surge, the velocities continue in the range of a few to tens of km s^{-1}.

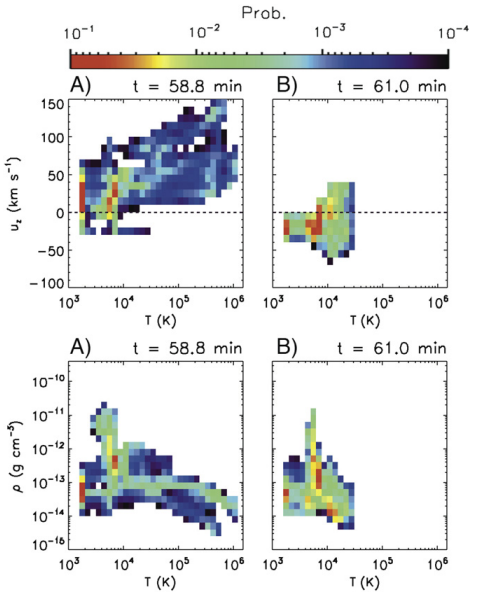

Figure 10. Double PDF plots for the temperature T and either the vertical velocity u_z (upper panels), or the density ρ (lower panels) of the Lagrangian elements.

The resulting global picture of the surge during its main development phase corresponds to plasma with velocities of tens of km s^{-1}. The temperatures tend to be $0.6-1\times10^4$ K (but with a small population which have retained their original cold temperature of a few thousand K) and the densities are in a large range between 10^{-14} and 10^{-11} g cm^{-3}.

5. THE DETACHMENT OF THE COOL EJECTION FROM THE DOME

Looking back at Figure 4, we realize that from panel (D) onward the ejecta adopt the shape of a detached *wall*, a cool and dense wall. Going a little earlier in time (panel (C)), we locate the origin of the detachment in the fact that the dome is being split in two at $x\approx11$ Mm, the process taking place mainly between $z\approx4$ and $z\approx6$ Mm. The appearance of this *cleft* is especially noticeable following the blue temperature contour ($T=3\times10^4$ K). In panels (D) and (E), the detachment is seen to be complete and the ejecta are from then on a separate wall-like structure.

The explanation of this phenomenon lies in the formation of a series of shocks above the dome starting at $t\approx59$ minutes (check also the density and temperature evolution shown in the accompanying Figure 4). Successive blobs of plasma coming up from the reconnection site along the top of the dome impinge on the surge. Strong shocks are created that deform and redirect plasma in the blob, last for a brief period of time and then weaken. A new blob arrives and creates again a shock system of the same kind. To illustrate the shock region in one of these collision events, Figure 11 (left panel: general view; right-panel: blow-up of the shock region) shows a map of the

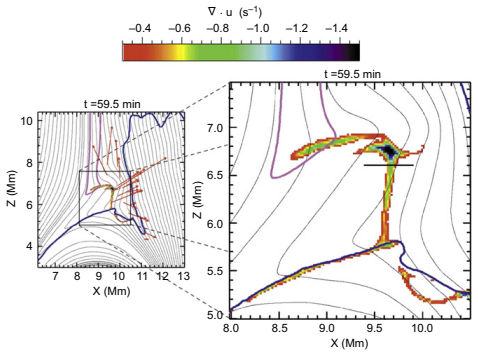

Figure 11. Left: map of the velocity field divergence, $\nabla \cdot \boldsymbol{u}$. Only the pixels where $\nabla \cdot \boldsymbol{u} < -0.5\,\mathrm{s}^{-1}$ are shown in color. Pink and blue contours are the same as those in Figure 4. The magnetic field is superimposed as black lines, while the velocity field in the detachment region is shown with red arrows. Right: zoom out for the previous panel to highlight the shock region. The horizontal black line is the cut used in Figure 12 to study the fast shock.

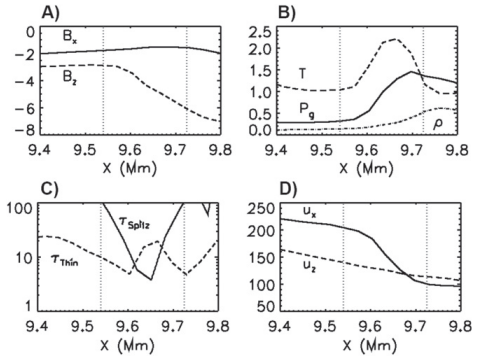

Figure 12. Jump relations along the horizontal black line in the right panel of Figure 11. The auxiliar vertical lines enclose the compression region where $\nabla \cdot \boldsymbol{u} \leqslant -0.2\,\mathrm{s}^{-1}$. Panel (A): magnetic field B_x and B_z in G. Panel (B): temperature T normalized to 4×10^5 K, gas pressure P_g in erg cm^{-3}, and density ρ normalized to 10^{-13} g cm^{-3}. Panel (C): characteristic times for the Spitzer conductivity, τ_{Spitz}, and the optically thin losses, τ_{Thin}, in seconds. Panel (D): velocities u_x and u_z in km s^{-1}.

divergence of the velocity field, $\nabla \cdot \boldsymbol{u}$, thus signposting the locations where a large compression is taking place. Further, the figure contains the blue (3×10^4 K) and pink (1.2×10^6 K) isotemperature contours of Figure 4, and a collection of field lines drawn as black curves. Also, the arrows show the velocity field in the detachment region, between the hot jet and the cool ejecta.

From the color map we see that the shock front has a wedge-like or arrowhead shape, which is a common feature of the successive shocks seen during the detachment phenomenon. The shocks cause high levels of compression and heating of the plasma going through it. The two sections of the arrowhead show distinctive features: the upper part, which is roughly horizontal and nearly perpendicular to the field lines in the postshock region, resembles a slow-mode shock almost of the switch-off kind. This could be related with the slow-mode shocks generated when plasmoids collide with the ambient magnetic field after being ejected, as illustrated by Yang et al. (2013). This shock is directly related with the hot jet: it is located at the base of the latter (see the pink contours) and the plasma goes through it before flowing along the horn-like jet field lines. We leave its study for a follow-up paper dealing with the properties of the hot jet.

The lower, almost vertical branch of the wedge, in turn, is a shock directly associated with the detachment process studied in this section. The field lines cross it but subtending only a small angle to the tangent direction to the shock front. $\nabla \cdot \boldsymbol{u}$ has high compression values of about $-0.8\,\mathrm{s}^{-1}$, sometimes reaching even $-3.0\,\mathrm{s}^{-1}$. Plasma traverses the structure from the left. Figure 12 shows the profiles across the shock for a number of relevant variables. To that end, we plot those variables along the horizontal black line plotted in the right panel of Figure 11. The B_z component (panel (A)) is not far from the perpendicular component of the field to the front normal. This component increases by a factor of 2 in absolute value across the shock, which suggests that the shock is a moderately strong, fast shock. This is also supported by the fact that the quasi-parallel component of the velocity (u_z, panel (D)) does not change substantially across the shock, whereas the normal velocity changes by a factor 2, approximately. The temperature has a suggestive profile (panel (B)), that we can understand with the help of the entropy sources (panel (C)). In the first half of the shock the temperature increases, mostly because of the compression work experienced by the plasma element when entering the shock. In the center and final half of the shock, however, T reaches a plateau and decreases: this is probably due to the action of the heat conduction (to a limited extent also of the optically thin radiation cooling): the characteristic cooling timescales are low (4 s for the former, see panel (C)), and fit with the duration of the transit of the plasma across the shock if one takes into account the motion of the front as a whole. Finally, the density increases by a factor 5 (panel (B)), which is larger than the maximum allowed for adiabatic shocks: the large compression ratio is reached thanks to the entropy decrease due to the non-adiabatic effects. As a further consequence of the heat conduction, the thermal energy is distributed efficiently along the individual field lines well beyond the shock itself, giving rise to the structure along the cleft that marks the boundaries of the cool ejection and lets it appear as a separate domain. The velocities involved in the shock, panel (D), are on the order of a hundred km s^{-1}.

The plasma diverted downward after crossing the vertical section of the shock penetrates deeper into the underlying dome as successive shock systems are formed. When the last one in the series ends ($t \approx 61$ minutes, Panel (F) of Figure 4), the surge is completely detached from the remnants of the dome on the left. The hot plasma domains at that time have the classical inverted-Y or Eiffel-tower shape commonly seen in observations, with one of the legs of the tower coinciding with the *cleft*. Meanwhile, the cool surge enters the decay phase following the swaying motion explained at the beginning of Section 4. Both the hot and cool ejections finally disappear almost simultaneously at around $t = 66$ minutes.

6. DISCUSSION

We have performed a 2.5D radiative-MHD numerical experiment of emergence of magnetized plasma through

granular convection and into the atmosphere. The time evolution of the system leads to the ejection of part of the emerged material as a cool and dense surge. The experiment was done with the Bifrost code, which includes a realistic multi-component EOS as well as modules for photospheric and chromospheric radiation transfer, heat conduction, and optically thin radiative cooling in the corona. In the following, we first provide a comparison with observational data (Section 6.1) and then discuss the relevance of some of the entropy sources not included in the flux emergence experiments so far (Section 6.2). The final paragraphs point out a number of limitations of the present experiment that may be overcome in the future (Section 6.3).

6.1. Observations

A first block of quantities that can be compared to observations concern the size, timescale, and kinematic properties of the surge. A more in-depth comparison must be done through a-posteriori synthesis of different spectral lines based on the numerical boxes. However, the most important spectral lines that one could use for this comparison (like Hα, Ca II H+K, or He II 10830 Å) require careful treatment including NLTE aspects; this kind of approach must therefore be left for future work.

The height of the surge in our experiment varies considerably in the different stages of the evolution. At the time of maximum development, the ejecta constitute a vertically elongated object with height of about 13 Mm and width of about 2 Mm. The observed length (see Section 1) falls typically in the interval 10–50 Mm, so the height of our surge is within the observed range, even though toward its lower limit. This fits with the fact that the experiment deals with a simple emergence event into a coronal hole, whereas many classical observations refer to surges measured in the context of flare episodes in active regions, which involve a larger amount of magnetic flux and where larger structures should be expected. The cool ejection in our experiment lasts for about 7–8 minutes, which, again, is toward the lower limit of the observed durations (several minutes to one hour, Jiang et al. 2007; Vargas Domínguez et al. 2014). Regarding the velocities, although high velocities of up to 150 km s^{-1} can be reached along the launch phase, during most of the surge evolution the mass elements have rising or falling velocities below 50 km s^{-1}, and the ejection is not collimated. The observations, in turn, yield a velocity range of 10−200 km s^{-1}, as inferred mainly from Hα measurements (Roy 1973; Canfield et al. 1996; Chae et al. 1999; Jibben & Canfield 2004; Uddin et al. 2012; Nelson & Doyle 2013; Vargas Domínguez et al. 2014, among others), which is compatible with the results of the experiment.

Concerning the acceleration, in the experiment we have detected two different patterns of behavior: (1) during the launch phase, the mass elements suffer large accelerations, well in excess of solar gravity; (2) when near the apex of their individual trajectories, the acceleration values are remarkably close to $g_\odot$. There is no definitive observational value to use for a comparison here: in the paper by Roy (1973), the author reports a fast rising phase for the surge with acceleration of 0.24–2.1 km s^{-2}, i.e., roughly 1–10 $g_\odot$. Observed values for the acceleration at the time of maximum and in the decay phase are more difficult to obtain. In their recent paper, Nelson & Doyle (2013) detected an apparent parabolic trajectory for the cool ejection in their study, but no particular value for the acceleration was given.

6.2. The Relevance of the Entropy Sources

An adequate treatment of the entropy sources and sinks in the energy equation, or, more generally, of the material properties of the plasma, like its EOS, is important when studying the formation and time evolution of the cool ejections. Thanks to the possibilities afforded by the Bifost code and to an extensive Lagrange tracing of the mass elements of the surge, we have been able to distinguish different patterns of behavior among them and group them into separate populations. One of those populations, Population B, provides a good illustration in that sense. That population covers 34% of the surge cross section at the time of maximum development. It reaches high temperatures, between 10^5 and 10^6 K, typically when going through the current sheet, but is then brought back down to classical surge temperatures of order 10^4 K thanks to the action of the radiation losses and thermal conduction terms. This population could not be obtained in more idealized experiments, like those of Yokoyama & Shibata (1996), Nishizuka et al. (2008), Jiang et al. (2012), Moreno-Insertis & Galsgaard (2013), and MacTaggart et al. (2015). The first authors, for instance, find that the material in the surge structure is not heated significantly along its life (which would roughly correspond to the behavior of our populations A and C). Instead, we find that a non-small amount of the plasma in the surge suffers heating/cooling processes that lead them to high temperatures during a fraction of its life. This explains part of the structural properties of the modeled surge and may also be of interest concerning its detection.

The importance of a proper treatment of the entropy sources and of the EOS may also apply to other cool ejections such as the macrospicules. Chromospheric material and hotter, transition-region material probably coexist in these objects, as indicated by their detection both in Hα and in the EUV line He II 304 Å. However, the numerical experiments in the literature (e.g., Murawski et al. 2011; Kayshap et al. 2013) are of the idealized kind, so, while possibly capturing various basic features of the macrospicule phenomenon, they may also miss important aspects.

6.3. The Progress Toward Realism in the Theoretical Modeling of Surges Following from Flux Emergence

The essential component in the observed solar surge phenomenon is plasma with chromospheric temperatures and densities, as follows from their detection in spectral lines like Hα, Ca II H+K, Ca II 8542 Å, or He II 10830 Å. Like for other important phenomena of the low solar atmosphere (prominences are a prime example for this), their theoretical study is intricate because of the difficulties of coping with the material properties of the chromospheric plasma. All previous numerical studies of surges following from flux emergence were done on the basis of highly idealized models, without radiation transfer nor a multi-component EOS with realistic abundances, partial ionization processes, etc. Our present paper constitutes a large step forward in that direction, given the degree of realism of the material modules of the Bifrost code, as explained in Section 2.1. In the following we first compare our results with those of the 3D experiment of Moreno-Insertis & Galsgaard (2013). Then, a few limitations of the present experiment are

discussed, namely the presence in flux emergence models of cool and dense plasma domains in the low atmosphere, the effects of partial ionization on Ohm's law, and the lack of ionization/recombination equilibrium in processes occurring on short timescales.

Our approach allowed us to gain new insights compared with previous idealized simulations of the ejection of cool surges, even with the recent 3D experiment by Moreno-Insertis & Galsgaard (2013). Major differences between the two experiments come from the inclusion in our case of detailed material properties, radiation transfer and heat conduction, which have allowed us, e.g., to discern different plasma populations that later constitute the cool surge, or to study the initial interaction of the rising plasma with realistic granulation, or to identify the process of detachment and decay of the surge. In a 2D experiment, one can reach much higher spatial resolution, which facilitates the study of many aspects difficult or impossible to consider in a 3D problem, like the formation and evolution of plasmoids or the shock structures associated with the jets. Finally, our Lagrange tracing has an extremely high cadence (thanks again to the reduced storage demands of a 2D experiment), and this is advantageous when pursuing the motion of the plasma elements across regions with strong gradients. On the other hand, various general properties of the surge in this paper are in agreement with the simulation of Moreno-Insertis & Galsgaard (2013): being three-dimensional, the cool ejecta in their experiment had the shape of an almost circular plasma wall with chromospheric density surrounding the emerged region, even if the largest concentration was found at the base of the hot jet. There, the cool domain had a height (∼10 Mm), similar to that obtained in the present 2.5D experiment, and width (∼6 Mm), which is wider than in the present paper, perhaps because of the lack of realistic convection cells in their experiment, which can modify the horizontal sizes of the emerged structures. The surge velocities, around 50 km s^{-1}, are also within the range given by those authors for their cool ejecta.

When large magnetized plasma domains rise from the solar interior to the low atmosphere, a dense and cold plasma dome is formed, as repeatedly shown in the numerical experiments since the 1990s. At the interface between the dome and the overlying atmospheric material a large density gradient arises. Numerical codes tend to smooth that sharp density contrast through diffusion, in many cases via some explicit diffusion term, like in Bifrost, or, in a less controllable fashion, through the hidden, intrinsic diffusion of the numerical scheme, like in formally ideal MHD codes. Irrespective of whether a process of mixing takes place in such interfaces in the actual Sun, any result associated with this diffusion in the theoretical models must be handled with care. In our case, we have identified a family of plasma elements originating in coronal heights (population D, Section 4.1.4) whose density is increased to a large extent via this kind of diffusion process when they pass near the current sheet before being incorporated to the surge. The initial mass of this family is negligible compared to the final mass of the surge; in some sense, that family is swallowed by the much more dense material coming from the dome, so the qualitative (and, to a large extent, quantitative) properties of the final surge should be widely independent of the evolution of this particular population. A different issue concerns the dome itself: the large expansion associated with the rise leads it to adopt cold temperatures, below 2000 K. The ad hoc heating term mentioned in Section 2 is then activated in the calculation to prevent the plasma from cooling to lower temperatures, for which the radiation tables used by Bifrost become inaccurate (see Leenaarts et al. 2011). The material of the surge originates essentially in the dome, so, in spite of the enormous advantages of the new generation of MHD codes compared with the previous idealized models, a fully realistic treatment of the evolution of the surge in its formation stage must await the completion of material modules for the codes adequate to the very cold plasma volumes in the low atmosphere.

In the same vein, another aspect that must be improved in future models of the solar surges is the use of a generalized Ohm's Law incorporating partial ionization effects. On the basis of the general results of Leake & Arber (2006), Arber et al. (2007), Martínez-Sykora et al. (2012, 2015), and Leake & Linton (2013), among others, we expect that these effects may allow some slippage of magnetic field and plasma via ambipolar diffusion and counteract to some extent the cold temperatures of the rising dome. This could affect the populations obtained in the surge, especially Population C (see Section 4.1.3). As a final item in the list of limitations in the realism of the current model, we mention here the lack of non-thermal equilibrium in the ionization/recombination processes of hydrogen and helium. As already proposed long ago (Kneer 1980), in chromospheric processes that occur on comparatively fast timescales (e.g., in shocks), the ionized species, especially hydrogen and helium, may take longer to recombine than predicted by local thermodynamic equilibrium (LTE) equations (see the recent results by Leenaarts et al. 2007 and Golding et al. 2014). This problem is particularly important if one tries to obtain a posteriori, i.e., on the basis of the calculated computational boxes, synthetic spectra for the hydrogen or helium lines from plasma at temperatures around 6×10^3 K (for H) or between 1 and 2×10^4 K (for He). However, the time evolution of the system itself may also be affected in a non-negligible way by this departure of LTE. The inclusion of the non-equilibrium effects into the models of surges is therefore another improvement that must be incorporated in future extensions of the present work.

We gratefully acknowledge financial support by the Spanish Ministry of Economy and Competitiveness (MINECO) through projects AYA2011-24808 and AYA2014-55078-P, as well as by NASA through grants NNX11AN98G, NNM12AB40P, and NNX14AI14G (HGCR grant) and contracts NNM07AA01C (Hinode) and NNG09FA40C (IRIS). The authors thankfully acknowledge the computer resources and the technical expertise and assistance provided at the LaPalma supercomputer installation (IAC, Spain) and at the Teide High-Performance Computing facilities (Instituto Tecnologico y de Energias Renovables, ITER, Spain), where the calculations presented in this paper were carried out. Use for test runs of the Pleiades cluster through the computing project s1061 from NASA's HEC division is also acknowledged. Finally, the authors are grateful to the members of the Bifrost development team for their help with the Bifrost code, and to the anonymous referee for his/her constructive comments.

REFERENCES

Arber, T. D., Haynes, M., & Leake, J. E. 2007, ApJ, 666, 541
Archontis, V., Galsgaard, K., Moreno-Insertis, F., & Hood, A. W. 2006, ApJL, 645, L161

Archontis, V., & Hansteen, V. 2014, ApJL, 788, L2
Archontis, A., Moreno-Insertis, F., Galsgaard, K., Hood, A., & O'Shea, E. 2004, A&A, 426, 1047
Bennett, S. M., & Erdélyi, R. 2015, ApJ, 808, 135
Bohlin, J. D., Vogel, S. N., Purcell, J. D., et al. 1975, ApJL, 197, L133
Brooks, D. H., Kurokawa, H., & Berger, T. E. 2007, ApJ, 656, 1197
Canfield, R. C., Reardon, K. P., Leka, K. D., et al. 1996, in IAU Coll. 153, Magnetodynamic Phenomena in the Solar Atmosphere—Prototypes of Stellar Magnetic Activity, ed. Y. Uchida, T. Kosugi, & H. S. Hudson (Cambridge: Cambridge Univ. Press), 49
Cao, T.-j., Xu, A.-a., & Tang, Y.-h. 1980, ChA, 4, 143
Carlsson, M., & Leenaarts, J. 2012, A&A, 539, A39
Chae, J., Qiu, J., Wang, H., & Goode, P. R. 1999, BAAS, 31, 963
Cheung, M. C. M., Schüssler, M., & Moreno-Insertis, F. 2007, A&A, 467, 703
Ellison, M. A. 1942, MNRAS, 102, 22
Fan, Y. 2001, ApJL, 554, L111
Finn, J. M., & Kaw, P. K. 1977, PhFl, 20, 72
Forbes, T. G., & Priest, E. R. 1984, SoPh, 94, 315
Furth, H. P., Killeen, J., & Rosenbluth, M. N. 1963, PhFl, 6, 459
Golding, T. P., Carlsson, M., & Leenaarts, J. 2014, ApJ, 784, 30
Goldston, T. P., & Rutherford, P. H. 1995, Introduction to Plasma Physics (Boca Raton, FL: CRC Press)
Gudiksen, B. V., Carlsson, M., Hansteen, V. H., et al. 2011, A&A, 531, A154
Gudiksen, B. V., & Nordlund, Å. 2005, ApJ, 618, 1020
Guglielmino, S. L., Bellot Rubio, L. R., Zuccarello, F., et al. 2010, ApJ, 724, 1083
Habbal, S. R., & Gonzalez, R. D. 1991, ApJL, 376, L25
Hansteen, V. H., Carlsson, M., & Gudiksen, B. 2007, in ASP Conf. Ser. 368, The Physics of Chromospheric Plasmas, ed. P. Heinzel, I. Dorotovic, & R. J. Rutten (San Francisco, CA: ASP), 107
Hansteen, V. H., De Pontieu, B., Rouppe van der Voort, L., van Noort, M., & Carlsson, M. 2006, ApJL, 647, L73
Hayek, W., Asplund, M., Carlsson, M., et al. 2010, A&A, 517, A49
Heyvaerts, J., Priest, E. R., & Rust, D. M. 1977, ApJ, 216, 123
Jiang, R.-L., Fang, C., & Chen, P.-F. 2012, ApJ, 751, 152
Jiang, Y. C., Chen, H. D., Li, K. J., Shen, Y. D., & Yang, L. H. 2007, A&A, 469, 331
Jibben, P., & Canfield, R. C. 2004, ApJ, 610, 1129
Kayshap, P., Srivastava, A. K., Murawski, K., & Tripathi, D. 2013, ApJL, 770, L3
Kirshner, R. P., & Noyes, R. W. 1971, SoPh, 20, 428
Kneer, F. 1980, A&A, 87, 229
Kurokawa, H., & Kawai, G. 1993, in ASP Conf. Ser. 46, IAU Coll. 141: The Magnetic and Velocity Fields of Solar Active Regions, ed. H. Zirin, G. Ai, & H. Wang (San Francisco, CA: ASP), 507
Leake, J. E., & Arber, T. D. 2006, A&A, 450, 805
Leake, J. E., & Linton, M. G. 2013, ApJ, 764, 54
Leenaarts, J., Carlsson, M., Hansteen, V., & Gudiksen, B. V. 2011, A&A, 530, A124
Leenaarts, J., Carlsson, M., Hansteen, V., & Rutten, R. J. 2007, A&A, 473, 625
MacTaggart, D., Guglielmino, S. L., Haynes, A. L., Simitev, R., & Zuccarello, F. 2015, A&A, 576, 4
Madjarska, M. S., Doyle, J. G., Hochedez, J.-F., & Theissen, A. 2006, A&A, 452, L11
Magara, T. 2001, ApJ, 549, 608
Martínez-Sykora, J., De Pontieu, B., & Hansteen, V. 2012, ApJ, 753, 161
Martínez-Sykora, J., De Pontieu, B., Hansteen, V., & Carlsson, M. 2015, RSPTA, 373, 40268
Martínez-Sykora, J., Hansteen, V., & Carlsson, M. 2008, ApJ, 679, 871
Moreno-Insertis, F. 2006, in ASP Conf. Ser. 354, Solar MHD Theory and Observations: A High Spatial Resolution Perspective, ed. J. Leibacher, R. F. Stein, & H. Uitenbroek (San Francisco, CA: ASP), 183
Moreno-Insertis, F., & Galsgaard, K. 2013, ApJ, 771, 20
Moreno-Insertis, F., Galsgaard, K., & Ugarte-Urra, I. 2008, ApJL, 673, L211
Murawski, K., Srivastava, A. K., & Zaqarashvili, T. V. 2011, A&A, 535, A58
Murray, M. J., Hood, A. W., Moreno-Insertis, F., Galsgaard, K., & Archontis, V. 2006, A&A, 460, 909
Nelson, C. J., & Doyle, J. G. 2013, A&A, 560, A31
Newcomb, W. A. 1961, PhFl, 4, 391
Newton, H. W. 1942, MNRAS, 102, 2
Nishizuka, N., Shimizu, M., Nakamura, T., et al. 2008, ApJL, 683, L83
Orozco Suárez, D., Bellot Rubio, L. R., del Toro Iniesta, J. C., & Tsuneta, S. 2008, A&A, 481, L33
Ortiz, A., Bellot Rubio, L. R., Hansteen, V. H., de la Cruz Rodríguez, J., & Rouppe van der Voort, L. 2014, ApJ, 781, 126
Pike, C. D., & Harrison, R. A. 1997, SoPh, 175, 457
Roy, J.-R. 1973, SoPh, 32, 139
Rust, D. M. 1976, RSPTA, 281, 353
Schlüter, A. 1957, in IAU Symp. 4, Radio Astronomy, ed. H. C. van de Hulst (Cambridge: Cambridge Univ. Press), 356
Schmahl, E. J. 1981, SoPh, 69, 135
Schmieder, B., Mein, P., Martres, M. J., & Tandberg-Hanssen, E. 1984, SoPh, 94, 133
Schmieder, B., Shibata, K., van Driel-Gesztelyi, L., & Freeland, S. 1995, SoPh, 156, 245
Shibata, K., Nozawa, S., & Matsumoto, R. 1992, PASJ, 44, 265
Skartlien, R. 2000, ApJ, 536, 465
Stein, R. F., & Nordlund, Å. 1998, ApJ, 499, 914
Tortosa-Andreu, A., & Moreno-Insertis, F. 2009, A&A, 507, 949
Uddin, W., Schmieder, B., Chandra, R., et al. 2012, ApJ, 752, 70
Vargas Domínguez, S., Kosovichev, A., & Yurchyshyn, V. 2014, ApJ, 794, 140
Yang, L., He, J., Peter, H., et al. 2013, ApJ, 777, 16
Yokoyama, T., & Shibata, K. 1995, Natur, 375, 42
Yokoyama, T., & Shibata, K. 1996, PASJ, 48, 353
Yoshimura, K., Kurokawa, H., Shimojo, M., & Shine, R. 2003, PASJ, 55, 313
Zwaan, C. 1987, ARA&A, 25, 83

3

Surges and Si IV bursts in the solar atmosphere: understanding IRIS and SST observations through RMHD experiments

In the previous chapter, there was an open question concerning whether one of the surge populations, the one that is heated to coronal temperatures and then cooled down to chromospheric ones, could show UV emission. For that reason, one of the objectives of this chapter is to explore surges in TR emission lines taking advantage of the high-resolution satellites and telescopes. In addition, we aim to analyze the surge in relation to other events and explain the observations by means of theoretical-numerical modeling developed during this thesis. To that end, we combine observations in the chromospheric line Hα, to identify the surge, together with the TR line Si IV 1402.77 Å, to see the TR impact of this phenomenon and the relation to UV bursts. In particular, we study a simultaneous episode of an Hα surge and a Si IV burst, occurred on 2016 September 03 in active region AR12585, using coordinated space and ground observations from IRIS and SST (see their descriptions in Section 1.4.4). The observational study allows us to identify emission of Si IV within the surge, which had not been reported in the literature so far. In order to give a theoretical interpretation of the observations, we performed 2.5D RMHD numerical experiments of surges obtained through magnetic flux emergence from the granular cells right below the surface up to the atmosphere. For this task, an improvement was introduced in the theoretical modeling with respect to the previous chapter of the thesis, namely, an extra module of the Bifrost code that calculates the Si IV population in NEQ ionization (see Section 1.4.1 of the Introduction). We then compare the results of the experiments with the observations using forward modeling, i.e., through the spectral synthesis of the simulations with subsequent degradation to the observational conditions. Thus, it is possible to have a first approach to interpret the observations, although the complete explanation is addressed in Chapter 4.

The main results and conclusions of this chapter are described in the following:

- Analyzing light curves from observations, we have detected that the surge and Si IV burst can be linked spatially and temporally to opposite magnetic polarity patches in the photosphere that converge and collide, which suggests that surges and Si IV bursts share a common physical origin. Additionally, an Ellerman bomb (EB) is visible in close vicinity just prior to the start of the burst and remains active during the whole lifetime of the burst, which is akin to the findings by Watanabe et al. (2011); Yang et al. (2013a); Vissers et al. (2013); although the relation between surges and EB does not seem to be common according to Rutten et al. (2013).

- One of the most striking results of this thesis is the finding, for the first time, of extended emission in Si IV within the observed surge. To date, the few papers with bursts and surges (e.g., Kim et al., 2015 and Huang et al., 2017) had only addressed the coexistence of surges, seen in Hα and Ca II 8542 Å, and Si IV brightenings, but without identifying evidences of Si IV within the surge domain. The observed Si IV spectral profiles in the surge are around a factor 2-5 brighter than a quiet-sun typical Si IV profile. Other interesting features of this finding is that the brightest emission in Si IV within the domain of the surge is located near its footpoints or base. Moreover, the profiles are mainly redshifted with asymmetries to the blue. Our finding implies that surges, which are traditionally associated with chromospheric lines such as Hα 6563 Å and Ca II 8542 Å, have enough impact in the TR to be detectable. In the next chapter, we see how one of the surge populations described in the Chapter 2 is the reason of the emission found in Si IV.

- With respect to the Si IV burst, it shows the typical characteristics reported in contexts other than surges (Peter et al., 2014; Vissers et al., 2015; Tian et al., 2016; Grubecka et al., 2016, among others). The burst appears in regions on the surface where magnetic flux regions of opposite polarity converge and collide. There, the profiles are broad, because of the presence of blue and red components, and absorption features appear superimposed on the Si IV lines. In addition, these locations reveal brightenings in the wings of Mg II h & k lines with small enhancement in the cores, and enhanced wings in Hα.

- Through spectral synthesis, we are able to distinguish resemblances with the observations, like the fact that the brightest points in Si IV within the surge are found near its footpoints or base. We also find that even the less bright regions of the surge in Si IV seem to be brighter than an average transition region. In the next chapter, we will provide a theoretical explanation for all this findings.

The above results and conclusions were published by Nóbrega-Siverio et al. (2017) in December 2017 in the volume 850 of *The Astrophysical Journal (ApJ)* with the title **Surges and Si IV Bursts in the Solar Atmosphere: Understanding IRIS and SST Observations through RMHD Experiments**. This paper is attached in the following pages and can also be found in the ADS:
`http://adsabs.harvard.edu/abs/2017ApJ...850..153N`

The Astrophysical Journal, 850:153 (12pp), 2017 December 1 https://doi.org/10.3847/1538-4357/aa956c

Surges and Si IV Bursts in the Solar Atmosphere: Understanding *IRIS* and SST Observations through RMHD Experiments

D. Nóbrega-Siverio[1,2], J. Martínez-Sykora[3,4], F. Moreno-Insertis[1,2], and L. Rouppe van der Voort[5]
[1] Instituto de Astrofisica de Canarias, Via Lactea, s/n, E-38205 La Laguna (Tenerife), Spain; dnobrega@iac.es
[2] Department of Astrophysics, Universidad de La Laguna, E-38200 La Laguna (Tenerife), Spain; fmi@iac.es
[3] Lockheed Martin Solar and Astrophysics Laboratory, Palo Alto, CA 94304, USA; juanms@lmsal.com
[4] Bay Area Environmental Research Institute, Petaluma, CA 94952, USA
[5] Institute of Theoretical Astrophysics, University of Oslo, P.O. Box 1029 Blindern, NO-0315 Oslo, Norway; rouppe@astro.uio.no
Received 2017 August 18; revised 2017 October 20; accepted 2017 October 20; published 2017 November 28

Abstract

Surges often appear as a result of the emergence of magnetized plasma from the solar interior. Traditionally, they are observed in chromospheric lines such as Hα 6563 Å and Ca II 8542 Å. However, whether there is a response to the surge appearance and evolution in the Si IV lines or, in fact, in many other transition region lines has not been studied. In this paper, we analyze a simultaneous episode of an Hα surge and a Si IV burst that occurred on 2016 September 03 in active region AR 12585. To that end, we use coordinated observations from the *Interface Region Imaging Spectrograph* and the Swedish 1-m Solar Telescope. For the first time, we report emission of Si IV within the surge, finding profiles that are brighter and broader than the average. Furthermore, the brightest Si IV patches within the domain of the surge are located mainly near its footpoints. To understand the relation between the surges and the emission in transition region lines like Si IV, we have carried out 2.5D radiative MHD (RMHD) experiments of magnetic flux emergence episodes using the Bifrost code and including the nonequilibrium ionization of silicon. Through spectral synthesis, we explain several features of the observations. We show that the presence of Si IV emission patches within the surge, their location near the surge footpoints and various observed spectral features are a natural consequence of the emergence of magnetized plasma from the interior to the atmosphere and the ensuing reconnection processes.

Key words: line: profiles – magnetohydrodynamics (MHD) – methods: observational – methods: numerical – Sun: chromosphere – Sun: transition region

Supporting material: animations

1. Introduction

Surges are a good example of the complexity of chromospheric ejections. In Hα 6563 Å, surges are seen as darkenings in the blue/red wings of the line with line-of-sight (LOS) apparent velocities of a few to several tens of km s^{-1} on areas with projected lenghts of 10–50 Mm (Kirshner & Noyes 1971; Roy 1973; Cao et al. 1980; Schmieder et al. 1984; Chae et al. 1999; Guglielmino et al. 2010, among others). They can be recurrent (Schmieder et al. 1995; Gaizauskas 1996; Jiang et al. 2007; Uddin et al. 2012) and have apparent rotational and helical motions (Gu et al. 1994; Canfield et al. 1996; Jibben & Canfield 2004; Bong et al. 2014). Recent observations show that the surges consist of small-scale thread-like structures (Nelson & Doyle 2013; Li et al. 2016) and that they appear to be related to shocks (Yang et al. 2014) and Kelvin–Helmholtz instabilities (Zhelyazkov et al. 2015). The surges have also been detected in other chromospheric lines, such as the Ca II 8542 Å infrared triplet (Yang et al. 2013; Kim et al. 2015), He I 10830 Å (Vargas Domínguez et al. 2014), Hβ 4861 Å (Zhang et al. 2000; Liu & Kurokawa 2004), and also in Ca II H & K (Rust 1976; Nishizuka et al. 2008; Liu et al. 2009).

Surges normally appear to be related with emerging flux regions (EFR, Kurokawa et al. 2007). This is especially evident in active regions (ARs), where there are many observations of such cool ejections (e.g., Brooks et al. 2007; Madjarska et al. 2009; Wang et al. 2014). Furthermore, surges are also associated with other phenomena such as light bridges (Asai et al. 2001; Shimizu et al. 2009; Robustini et al. 2016) and explosive events (EEs), EUV or X-ray ejections (see, e.g., Schmahl 1981; Canfield et al. 1996; Chen et al. 2008; Madjarska et al. 2009; Zhang & Ji 2014). It has also been suggested that surges can be related to Ellerman bombs (EBs; Watanabe et al. 2011; Vissers et al. 2013; Yang et al. 2013); nevertheless, this relation does not seem to be common (Rutten et al. 2013).

On the other hand, observations carried out with the *Interface Region Imaging Spectrograph* (*IRIS*) satellite (De Pontieu et al. 2014) have provided a new perspective on transient phenomena in the chromosphere and transition region. In particular, the connection between UV bursts observed with *IRIS* (also referred to as *IRIS* bursts or *IRIS* bombs; Peter et al. 2014) and previously known phenomena has become an active area of research (see, e.g., Judge 2015; Vissers et al. 2015; Tian et al. 2016; Grubecka et al. 2016, among others). In this context, recent papers report on the coexistence of surges with bursts in Si IV (Kim et al. 2015, Huang et al. 2017 and M. S. Madjarska et al. 2017, in preparation); nevertheless, the focus of those papers was mainly on the bursts, without presenting an in-depth analysis of the associated surges.

The aim of this paper is to explore the response of transition region lines during surge formation and to characterize and explain the corresponding spectral profiles. Furthermore, we want to provide theoretical support for the relation between Hα surges and other phenomena such as Si IV bursts and EBs. To that end, we use coordinated observations from space and the ground with *IRIS* and the Swedish 1-m Solar Telescope (SST; Scharmer et al. 2003). Those instruments provide high-resolution observations

that cover chromospheric and transition region lines, which are essential for this study. Theoretical support is given by 2.5D numerical experiments similar to the one discussed in detail by Nóbrega-Siverio et al. (2016, hereafter NS2016), but extending the Bifrost code capabilities (Gudiksen et al. 2011) by including a module developed by Olluri et al. (2013b) that calculates the ionization state of the Si IV in nonequilibrium (NEQ).

The layout of the paper is as follows. Section 2 describes the *IRIS* and SST coordinated observations, and briefly the numerical models. In Section 3, we analyze the observations showing mainly Si IV profiles, Doppler shifts, and line widths in the region of interest. In Section 4, we study the synthetic spectral profiles obtained from the numerical experiments, comparing them with the observations. Finally, Section 5 contains the conclusions and a summary.

2. Observations and Numerical Model

2.1. Coordinated Observations

For this paper, we have used coordinated observations of *IRIS* and SST obtained on 2016 September 03 from 07:49:21 to 10:03:37 UT centered on active region AR 12585 at heliocentric coordinates $(x, y) = (-561'', 44'')$ and observing angle $\mu = 0.8$.

1. The *IRIS* data set corresponds to the observation program OBSID: 3625503135. Those observations cover a maximum field of view (FOV) of $65'' \times 60''$. The spectral information is obtained through a medium-dense raster that covers $60''$ in the y direction and scans $5''.28$ in the x direction in 16 steps of $0''.33$ separation for each step, with a raster cadence of 20 s. The exposure time is 0.5 s, the spatial scale is $0''.166$ pixel^{-1}, and the spectral sampling of the FUV spectra has been binned four times in the camera from 2.7 to 11 km s^{-1} to increase the signal level. Concerning the slit-jaw images (SJI), C II 1330, Si IV 1400, and Mg II k 2796 Å were taken with a cadence of 10 s obtaining a total of 800 images in each passband. The data have been calibrated for dark current, flat-field, and geometric correction. We analyze level 2 data (De Pontieu et al. 2014) produced by SolarSoft's `iris_prep.pro` routine version 1.83, which includes an updated version of the wavelength calibration (level2 version L12-2017-04-23). When studying *IRIS* FUV spectra profiles in the following, we shall consider temporal and spatial evolution of features like intensities, relative velocities, line widths, and asymmetries. On the other hand, the absolute wavelength calibration of these observations is not good enough to allow for a determination with accuracy better than 20–25 km s^{-1} of the global Doppler shift. This is due to the lack of photospheric lines in this data set as a result of the short exposures.
2. The SST data set contains Ca II 8542 Å and Hα 6563 Å spectral scans obtained with the SST/CRISP Fabry–Pérot Interferometer (Scharmer 2006). The CRISP scans have a temporal cadence of 20 s, a spatial sampling of $0''.057$ per pixel and an FOV of $\sim 58'' \times 58''$. The diffraction limit of the SST at 6563 Å is $0''.14$. Hα was sampled at 15 line positions from -1500 mÅ to $+1500$ mÅ (FWHM transmission profile: 66 mÅ), and Ca II 8542 was sampled in the spectropolarimetric mode at 21 spectral positions between -1750 mÅ and $+1750$ mÅ offset from the line core. The wings were sparsely sampled and the line core region was sampled with equidistant steps of 70 mÅ between ± 455 mÅ (FWHM transmission profile: 107 mÅ). Taking into account the magnetic sensitivity and the wide range in formation height of the Ca II 8542 line (see, e.g., de la Cruz Rodriguez 2010), we construct photospheric polarization maps by adding the Stokes V maps of the three outer spectral positions in both wings, preserving the sign of magnetic polarity by effectively subtracting the sum of the three red wing maps from the sum of the three blue wing maps. While the Ca II 8542 line core originates from the chromosphere, the far wings originate from the photosphere, so these accumulated polarization maps serve as a proxy for the photospheric magnetic field (de la Cruz Rodríguez et al. 2012; Ortiz et al. 2014). The CRISP data were processed following the CRISPRED data reduction pipeline (de la Cruz Rodríguez et al. 2015), which includes Multi-Object Multi-Frame Blind Deconvolution image restoration (van Noort et al. 2005). The alignment with the *IRIS* data was done by scaling down the CRISP data to the *IRIS* pixel-scale and through cross-correlation of the Ca II 8542 Å wing images with the *IRIS* SJI 2796 channel. This alignment has been shown to be accurate down to the level of the *IRIS* pixel ($0''.17$, Rouppe van der Voort et al. 2015).

Figure 1 shows a fraction of the FOV of the region observed by *IRIS* and SST at ~09:39 UT. Panel (A) shows a polarization map of the Ca II 8542 Å wings that serves as a proxy of the photospheric magnetic field in active region AR 12585. Panel (B) contains the *IRIS* SJI 1400; and panel (C) is the SST image in the blue wing of Hα at -46 km s^{-1} (an accompanying movie of the figure is provided in the online version). The solid rectangle in all three panels identifies the area of interest where the events originate. Additionally, part of that region is also covered by the *IRIS* raster (see the area within the vertical dashed lines in the figure), so we have detailed Si IV spectral information from part of the surge and burst to compare with the synthetic spectra of the numerical experiment. In panel (B), the arrows mark two regions, R1 and R2, that correspond to a surge and a burst, respectively, and which are explained in detail in Section 3. At the time of the figure, approximately at 09:39 UT, two opposite polarities are colliding within the solid rectangle (see panel (A)), while in panel (B) a Si IV burst (green contour) is visible around $(x, y) = (-557'', 51'')$. Co-spatial with the upper part of the bright region in the SJI 1400 at $(x, y) = (-558'', 51'')$, we identify an intense brightening in the Hα wing in panel (C), which is highlighted with a red contour within the burst. The Hα spectral profile reveals that this is an EB (see Section 3). The blue contours in the three panels mark out dark structures visible in panel (C). Some of those dark structures correspond to Hα surges; in particular, the relevant one for this paper is marked by the R1 arrow and appears during the Si IV burst (R2). Following the darkenings in the SST images, it seems that this surge is ejected leftwards of $(x, y) \sim (-559'', 49'')$; we will refer to that location as *the footpoint of the surge* in the following.

2.2. The Numerical Experiment

In order to understand the physics of the surges and related phenomena, it is necessary to provide theoretical support to the

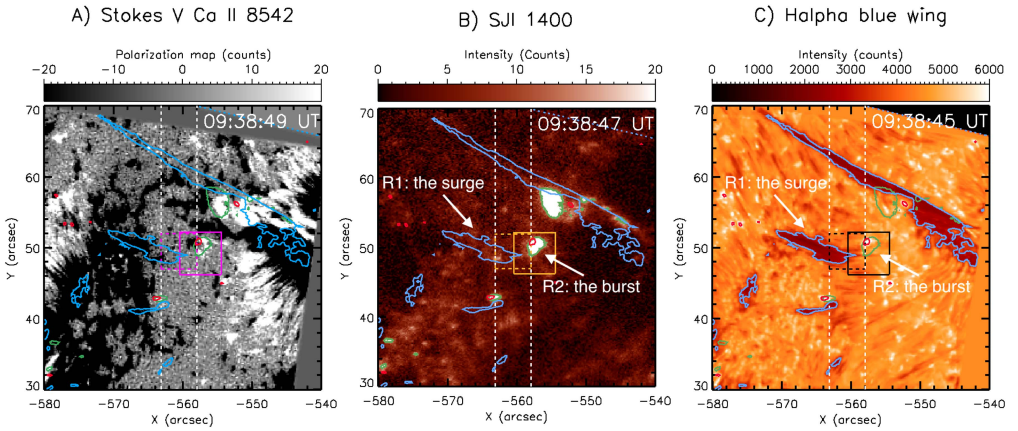

Figure 1. Context images of the active region AR 12585 on 2016 September 03 at ∼09:39 UT observed by *IRIS* and SST. (A) Stokes *V* polarization map of the far wings of Ca II 8542 Å serving as a proxy of the photospheric magnetic field. (B) *IRIS* slit-jaw image (SJI) in the Si IV 1400 Å passband. (C) SST/CRISP image in the blue wing of the Hα at −46 km s^{-1}. Bright regions in the SJI 1400 (>16 counts) are overplotted as green contours in all three panels, while the bright (6500 counts) and dark structures (3100 counts) of the Hα blue wing scan are superimposed in red and blue, respectively, to facilitate the identification. The arrows R1 and R2 point to the different regions, surge, and burst, respectively, explained in detail in Section 3. The region used for the integration for Figure 2 is marked with a solid rectangle. White dashed lines indicate the region covered by the *IRIS* raster. The area contained in the dashed rectangle is used for Figures 3 and 4. The animation of this figure shows the time evolution of the three panels from ∼08:56 UT to the end of the coordinated observations at ∼10:03 UT.

(An animation of this figure is available.)

observations. To that end, we have run two 2.5D numerical experiments in which a surge results from magnetic flux emergence and where thermal conduction and radiative transfer are treated in a self-consistent manner.

1. Concerning the code, the present experiments have been performed with the 3D RMHD Bifrost code (Gudiksen et al. 2011; Carlsson & Leenaarts 2012; Hayek et al. 2010). In addition, we have enabled a module to calculate the nonequilibrium (NEQ) ionization for silicon developed by Olluri et al. (2013b). Thus, we are able to compute the emissivity and then the synthetic spectra under optically thin conditions, as in the papers by Olluri et al. (2015) and Martínez-Sykora et al. (2016), for different orientations of the LOS (−15°, 0°, and 15°) with respect to the vertical direction z.
2. Regarding the numerical setup, the two runs are similar to the one in the NS2016 paper. The main differences are as follows: (1) we have kept the resolution of NS2016 but increased the physical domain, namely, 0.0 Mm $\leqslant x \leqslant$ 32.0 Mm and −2.6 Mm $\leqslant z \leqslant$ 30.0 Mm, where $z = 0$ Mm corresponds to the solar surface; (2) one of the current experiments has a vertical coronal magnetic field while the other is slanted; and (3) the initial axial magnetic flux is lower than in NS2016, $\Phi_0 = 6.3 \times 10^{18}$ Mx. More results about the numerical experiment will be provided in a follow-up paper (D. Nóbrega-Siverio et al. 2017, in preparation), where a deeper analysis of the theoretical aspects of the experiments is carried out.
3. Since we are interested in synthesizing Si IV for comparison purposes with the *IRIS* observations, spatial and spectral PSF (Gaussian) degradation of the theoretical data must be carried out to reduce the spectral profiles into the *IRIS* instrumental spatial and spectral resolution (0.″33 and 26 mÅ respectively). Finally, we convert the degraded line intensity from CGS units (erg s^{-1} cm^{-2} sr^{-1}) to *IRIS* photon count number (DN s^{-1}) for direct comparisons using

$$I_{IRIS} = I_{CGS}\,\frac{A\,p\,w}{r^2}\,\frac{\lambda}{h\,c}\,\frac{1}{k}, \qquad (1)$$

where $A = 2.2$ cm^2 is the effective area for wavelengths between 1389 and 1407 Å, $p = 0.''167$ is the spatial pixel size, $w = 0.''33$ is the slit width, $r = 3600 \cdot 180/\pi$ is the conversion of arcsec to radians, $\lambda = 1402.77$ Å is the wavelength of interest, h is the Planck constant, c is the speed of light, and $k = 4$ is the number of photons per DN in the case of FUV spectra (see De Pontieu et al. 2014, for the instrumental specifications about *IRIS*).

3. Observations: Results

Along the observation, we are able to distinguish two main episodes of surge activity in the SST/CRISP maps with accompanying brightenings in the SJI 1400: one taking place between 08:14 and 08:39 UT and the other between 09:27 UT and 10:03 UT, which is the end of the coordinated observation. Both episodes seem to be related to the appearance of positive polarity patches within a pre-existing negative polarity region. In this paper, we focus on the second one since the *IRIS* spectral raster covers most of it in contrast to the first episode.

3.1. Origin and Identification of the Surge and Burst

As we said in the Introduction, surges are closely related to EFRs. For this reason, we looked for evidences of episodes of magnetic flux emergence and cancellation. Figure 2 illustrates the evolution of different integrated data within the solid

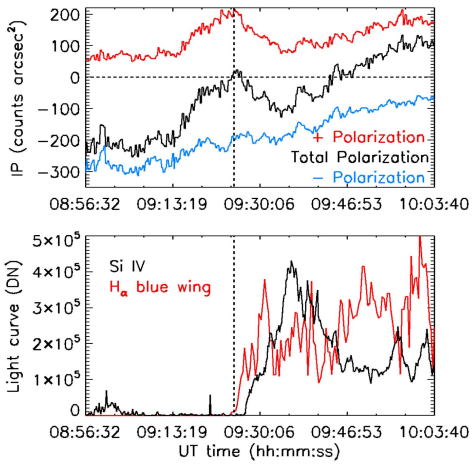

Figure 2. Curves obtained from the integration within the solid rectangle plotted in the three panels of Figure 1. Top: integrated polarizaton (IP), where the total polarization is shown in black, negative in blue, and positive polarization in red. The horizontal dashed line indicates the zero value for the polarization. Bottom: light curve of Si IV (black) and of the Hα blue wing (red). For both panels, the vertical dashed line marks the instant of the maximum polarization and the start of the brightenings.

rectangle of the three panels in Figure 1 (and the accompanying animation). The top panel of Figure 2 contains information about the magnetic flux; the black curve corresponds to the signed total flux and shows that, prior to the event, the region is dominated by the negative polarity. Around 09:13 UT, the positive polarity (red curve) increases up to four times its initial value, reaching the maximum value at 09:25 UT (vertical dashed line). This increase is due to positive polarity patches that appear within the rectangle in which we are integrating the flux. After the positive flux reaches its maximum, the total net flux decreases and, around 09:27 UT, first brightenings are observed in the SST Hα images (see panel (C) of Figure 1) and also in Ca II. The brightness increase is also evident in the bottom panel of Figure 2, where we plot the light curve of the blue wing of Hα integrated in the solid rectangle of Figure 1. Cospatially with the SST brightenings and approximately 2 minutes later, brightenings are also visible in the *IRIS* SJI 1400: the Si IV burst, which is marked in panel (B) of Figure 1 by the R2 arrow, and whose corresponding integrated light curve is illustrated in the bottom panel of Figure 2 in black color. Simultaneously and around the same region where the burst originates, a surge is discernible as a dark and elongated structure consisting of small-scale threads, first in the blue wing and then in the red wing of Hα and Ca II (see R1 arrow in panel (C) of Figure 1). Those darkenings are visible in the images in wavelength positions corresponding to $\sim$20–60 km s^{-1}. This surge has projected lengths ranging from a few megameters up to 8 Mm, while the projected width is around 1 or 2 Mm. After 25 minutes ($\sim$09:52 UT), the activity of both the Si IV burst and the surge becomes weak; nonetheless, it is enhanced again almost at the end of the coordinated observation (10:03 UT). This may suggest a recurrent behavior similar to that observed for surges (Schmieder et al. 1995; Gaizauskas 1996; Jiang et al. 2007; Uddin et al. 2012); and for *IRIS* bursts (Peter et al. 2014; Gupta & Tripathi 2015).

3.2. Spectral Properties of the Surge and Burst

In this section, we analyze the surge and the accompanying burst, i.e., the structures labeled R1 and R2 in Figure 1. To that end, in panels (B) and (C) of Figure 1, we select an area (dashed rectangle) that coincides horizontally with the region covered by the *IRIS* raster, namely, $-563\farcs2 \leqslant x \leqslant -558\farcs0$ and located vertically between $47\farcs0 \leqslant y \leqslant 52\farcs0$. Detailed maps of the intensity peak of Si IV 1402.77 Å and Hα at -46 km s^{-1} within that rectangle are shown as panels (A) and (B), respectively, in Figure 3. Furthermore, the figure contains spectral profiles for the various locations marked with symbols in panels (A) and (B): two for the surge (R1a and R1b, where we have averaged four spatial pixels in order to increase the signal-to-noise ratio), and three for the burst (R2a, R2b, and R2c). Those profiles are drawn as solid curves and correspond to the lines of Si IV 1402.77 Å (left column) and Hα (right column). Furthermore, the left panels contain a Gaussian fit to the Si IV 1402.77 Å profile (red dashed curve), and a reference average profile (black dashed–dotted line), which is calculated for the whole FOV and length of the observation.

On the other hand, and to extend the analysis, Figure 4 contains maps, also at $\sim$09:39 UT, of (A) the maximum intensity, $I_{\rm max}$, of the Si IV 1402.77 Å profile; (B) the Doppler shift v_D; (C) the line width σ; and (D) the R(ed)–B(lue) asymmetry, which is the difference between the integral of the two wings of the profile in the same velocity ranges, in this case, between 50 and 80 km s^{-1} (see De Pontieu et al. 2009; Martínez-Sykora et al. 2011; Tian et al. 2011, for further details about the R-B asymmetry calculation). The variables v_D, σ, and R-B are obtained from the Gaussian fit centered at the spectral position of the peak of the profile. The lower four panels contain the same variables but after being binned twice in each direction, thus getting a better signal-to-noise ratio and facilitating the identification of the surge in Si IV. An animation of this figure is available online.

3.2.1. R1: the Surge

The region selected for Figure 3 contains about one-third of the surge (R1), which is identifiable as a dark structure in the Hα image between $y = 47''$ and $y = 50''$. The Hα profiles R1a,b underneath show a dark blue wing with respect to the reference profile. Those two profiles correspond to two different locations of the surge: the brightest point of Si IV 1402.77 Å within the surge (blue diamond, hereafter R1a), and a fixed position around $x = -562\farcs5$ and $y = 48\farcs5$ (blue cross, R1b). In both locations, we can identify significant emission in Si IV that, as far as we know, has not been reported before in the literature. The main properties of this region concerning Si IV are as follows.

1. The emission in Si IV is sporadic and we see it mostly when the surge appears in the blue wing of Hα, in particular, between 09:34 UT and 09:41 UT (see the animation of Figure 3).
2. The Si IV intensity within the surge is weak in comparison to the burst, which could be the reason why it has not been reported before. This is evident in panels (A) and (E) of Figure 4 if we compare the values within the red contour (the burst) with the ones inside the blue

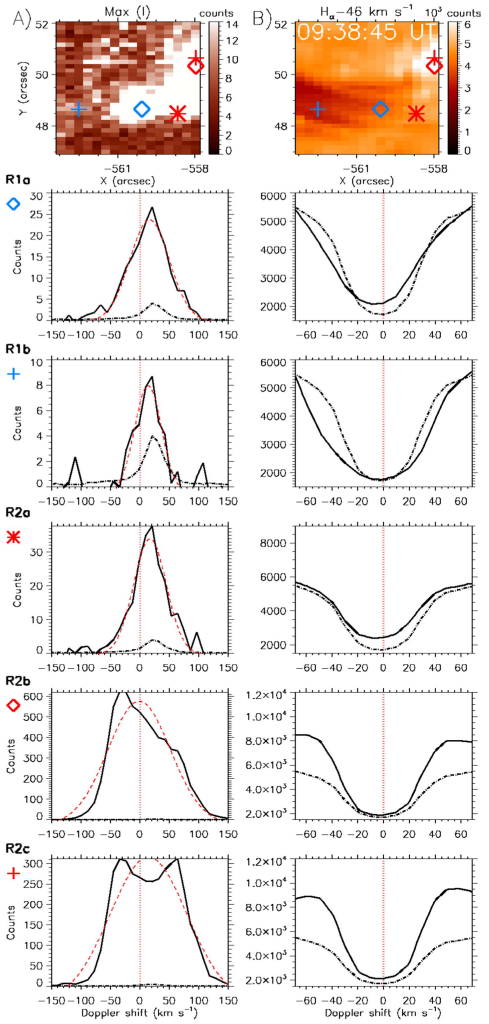

Figure 3. (A) Raster intensity peak map of the Si IV 1402.77 Å profile. (B) Image at the blue wing of Hα (−46 km s^{-1}). Various locations of regions R1 and R2 are indicated by blue and red symbols, respectively, and their corresponding profiles are shown below panels (A) and (B). The left column illustrates Si IV 1402.77 Å profiles (black solid line), the Gaussian fit to them (red dashed curve), and the reference average profile (black dashed–dotted line). The right column illustrates the Hα profiles in the various regions (solid line) and the reference average profile (dashed–dotted line). For R1 panels, we have averaged four pixels in order to increase the signal-to-noise ratio of this region. The animation of this figure shows the time evolution of the profiles of each region from ∼09:30 UT until ∼09:51 UT.

(An animation of this figure is available.)

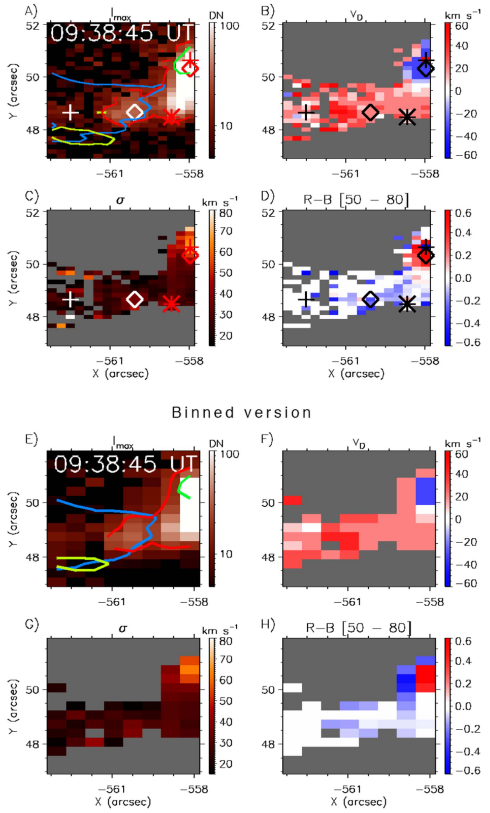

Figure 4. Four upper panels are maps of various features of the Si IV spectral profiles. (A) Raster intensity peak of the Si IV 1402.77 Å profile at ∼09:39 UT with overlying contours indicating the burst (red contour, where $I_{max} > 16$ DN); the EB (green); the surge in the Hα blue wing (blue); and in the red wing (yellow). (B) Doppler shift v_D in km s^{-1}, where the spectral position corresponding to the maximum intensity is used as the line centroid; (C) line width σ in km s^{-1}; and (D) R-B asymmetry between 50 and 80 km s^{-1} normalized to the peak intensity. A gray color mask is overplotted in panels (B)–(D) in places outside the burst and surge, and where the intensity is below 5 counts and σ is below 16 km s^{-1}. The four lower panels show the same quantities after a spatial binning by a factor of two in each direction. The animation of this figure contains the time evolution of the panels from ∼09:30 UT until ∼09:51 UT.

(An animation of this figure is available.)

Table 1
Temporal Averages of Si IV 1402.77 Å for (1) Peak Intensity I_{peak} with Respect to That of the Reference Profile $I_{peak,0}$, Doppler Shift v_D, and Line Width σ

Region	$\langle I_{peak}/I_{peak,0}\rangle$	$\langle v_D\rangle$ (km s^{-1})	$\langle\sigma\rangle$ (km s^{-1})
R1a	5.2 ± 1.4	20.2 ± 10.4	22.9 ± 5.3
R1b	1.9 ± 0.5	22.7 ± 20.5	29.6 ± 9.4

contour (the surge). During the event, the ratio between the peak of the Si IV profile and the one of the reference profile (black dashed–dotted line in Figure 3) is on average around 5.2 in R1a and 1.9 in R1b (see Table 1), with maximum values of 8.9 and 2.7 respectively.

3. Given its definition, R1a, the brightest Si IV location within the surge, moves with time, but we have found

that it is mostly located near the region that we have called *the footpoint of the surge* in Section 2.1 (see the animation of Figure 3). It can also be seen that R1a is a small-scale brightening of a few pixels at most. This suggests that *IRIS* does not completely resolve the spatial structure of R1a. The location of the brightest Si IV emission that is near the footpoints is reproduced in the numerical experiments and could be a characteristic feature of the surges. In fact, in the experiments we also provide a possible reason why R1a is sometimes not so close to the footpoints (Section 4.2.1).

4. In the observed surge, Si IV shows mainly redshifted profiles (see panels R1a and R1b in Figure 3 and panels (B) and (F) of Figure 4). In order to illustrate this quantitatively, we calculate average values of v_D for the two regions R1a and R1b when the Si IV intensity is larger than 5 counts and σ is at least 16 km s^{-1}, i.e., when the Si IV signal is greater than the reference average profile. The results are shown in Table 1. We see that the Si IV emission within the surge shows redshifts with an average value around 20–23 km s^{-1}. (Note that the relative Doppler velocity is blueshifted around 2 km s^{-1} only with respect to the reference profile.)
5. Within the surge, the line width σ is around 23–29 km s^{-1} (see panel (C) in Figure 4 and the corresponding average in Table 1). Those values are approximately a factor of 4 greater than the corresponding value of the width just for thermal broadening ($\sigma_{\rm th} = 6.86$ km s^{-1} taking the temperature formation peak at $\log(T) = 4.90$ in statistical equilibrium). We calculate the nonthermal line broadening σ_{nt} following De Pontieu et al. (2015) with

$$\sigma_{nt} = \sqrt{\sigma^2 - \sigma_{\rm th}^2 - \sigma_{\rm inst}^2}, \quad (2)$$

where $\sigma_{\rm inst} = 3.9$ km s^{-1}. The obtained nonthermal widths, 21.45 and 28.52 km s^{-1} for R1a and R1b, respectively, are on the upper range of the typical values for an active region (see De Pontieu et al. 2015); nevertheless, we would need more Si IV observations to carry out a statistical analysis in order to know whether this is an intrinsic characteristic of the surges or not.
6. Concerning panel (D) of Figure 4, we find some R-B asymmetry mainly to the blue side in the surge footpoints. This is more evident in panel (H) of the figure, which contains a version of panel (D) spatially binned by a factor two in both directions. The found R-B asymmetry implies that a small fraction of the surge plasma is moving with velocities greater than 50 km s^{-1} relative to the profile peak.

3.2.2. R2: the Burst

The other region we have analyzed is the part of the burst (R2) for which we have *IRIS* spectral profiles. The three lower rows of Figure 3 show the profiles in three different locations: the brightest Si IV point between $x = -558\farcs67$ and $x = -557\farcs97$, which corresponds to locations within the burst close to the surge footpoints (red asterisk, hereafter R2a); at the location within the burst that has the maximum Si IV emission (red diamond, R2b), and at the brightest point in the Hα wings at 46 km s^{-1} within the area of the Si IV burst (red cross, R2c). In the following, we describe the main properties of this region.

1. R2a can be considered the transition between the surge and the burst. In this region, the Si IV profiles repeatedly change in time between being blueshifted and redshifted, with small Doppler velocities and line widths of ± 30 km s^{-1} (see the accompanying movies of Figures 3 and 4). In Si IV, this region is slightly brighter than R1, but weaker than the following ones. The latter can be said also for Hα, which is characterized by showing some enhancement, both in the wings and core, but not at the same level as R2b and R2c.
2. Regarding R2b and R2c, the Si IV spectra are characterized by multicomponent profiles, see the corresponding panels in Figure 3; the blue component of the profiles is usually the brightest one, as shown in panel (B) of Figure 4, where the peak of the profile is blueshifted; the profiles are broad, see panel (C), where $\sigma > 60$ km s^{-1}, and they show strong asymmetry to the red, see panel (D). The polarization map in Figure 1 reveals that R2c mostly coincides with the location where the two underlying opposite polarities collide. This situation is often interpreted in the observational literature by assuming that the two components of the Si IV profiles correspond to bidirectional flows due to magnetic reconnection. Further evidence about magnetic reconnection and ejection of plasmoids is provided by Rouppe van der Voort et al. (2017) who analyze the same *IRIS* and SST observations but include spectrally resolved Ca II K imaging from the new CHROMIS Fabry–Pérot instrument at the SST.

   During the event, the brightest Si IV (R2b) is usually located close to the brightest Hα wing (R2c) in the upper part (solar *Y*-axis) of the burst in Si IV, and they can even overlap on a few occasions. Interestingly, between 09:45:30 and 09:46:10, when the surge is visible in the red wing of Hα, R2b moves down in the *Y*-axis approximately 2″, while R2c holds in the same position. This may indicate motion of plasma emitting strongly in Si IV. The two-component profiles described above and this motion of the brightest point in Si IV within the burst are addressed in Section 4.2.2.

We have also carried out a brief study of the other spectral lines observed by *IRIS* and found that R2b and R2c show absorption features superimposed on the Si IV 1393.76 Å line that correspond to Ni II 1393.33 Å redshifted around 13 km s^{-1}. We looked for further evidence in the *IRIS* spectra and also detected absorption of Ni II 1335.20 Å in the C II profile. Similar absorption features have been reported in *IRIS* lines by other authors like Schmit et al. (2014), Peter et al. (2014), Kim et al. (2015), Vissers et al. (2015), and Tian et al. (2016), which indicate that there is overlying dense and cold plasma on top of the Si IV source. Concerning the other *IRIS* lines, there are brightenings in the wings of Mg II h and k lines with small enhancement in the cores, which is akin to what was described by Tian et al. (2016) about *IRIS* bursts and point to heating of chromospheric plasma. There is also evidence of emission in the triplet of subordinate lines of Mg II at 2798.75 and 2798.82 Å, indicating an abrupt temperature increase in the lower chromosphere (see Pereira et al. 2015). The *IRIS* profiles do not show

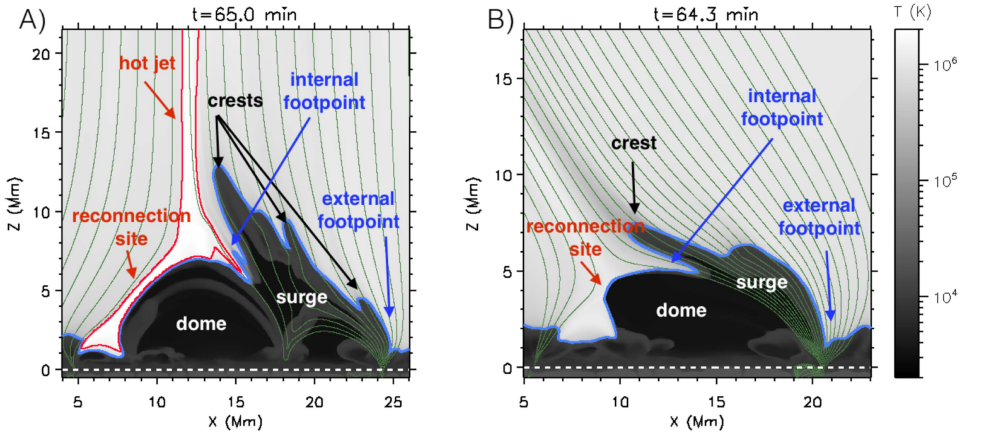

Figure 5. 2D temperature maps of the surge experiments showing the context and the regions of interest. (A) The vertical coronal magnetic field experiment at $t = 65.0$ minute. (B) The slanted coronal magnetic case at $t = 64.3$ minute. Additionally, magnetic field lines are overimposed in green and temperature contours are added for $T = 10^{4.9}$ K (blue) and $T = 1.2 \times 10^6$ K (red).

the forbidden O IV 1401.2 and 1399.8 Å lines, so we cannot use them for density diagnostics as carried out by Olluri et al. (2013a), Polito et al. (2016), or Martínez-Sykora et al. (2016). There is no evidence, either, of Fe XII at 1349 Å, which forms around 1.5 MK. The lack of O IV and Fe XII is likely due to the very short exposure time of this observation (0.5 s) since those lines are fainter and require longer exposure times (De Pontieu et al. 2014).

With respect to the spectra obtained by SST, in Figure 3, we see enhanced wings in the Hα profiles both in R2b and in R2c, which resemble the profiles found by Kim et al. (2015) in *IRIS* bursts. In the associated movie, we can see that the Hα profiles can show extremely enhanced wings, while the core is mostly kept unperturbed, as in EB profiles.

4. Numerical Experiment: Results

In this section, we analyze synthetic profiles from the numerical experiments introduced in Section 2.2 in order to compare them with the previously described observations, thus attempting to provide a theoretical understanding of the phenomena studied. The layout of this section is as follows: (1) a general description of the time evolution of the experiments, and (2) the synthesis and comparison with the *IRIS* observations.

4.1. A Brief Description of the Time Evolution

The general features of the time evolution of these experiments are qualitatively similar to those described by NS2016. In the present paper, we focus on the advanced phases of the evolution, when the magnetized emerged plasma that has expanded into the solar atmosphere collides with the pre-existing coronal field, and a surge is obtained as an indirect consequence of magnetic reconnection processes.

Figure 5 shows the context of the numerical simulations through a temperature map for each experiment: panel (A), the vertical experiment at $t = 65.0$ minute, and panel (B), the slanted one at $t = 64.3$ minute. In panel (A), we can see the emerged plasma with a dome shape between $8 \leqslant x \leqslant 18$ Mm; a coronal hot jet, with a classical Eiffel-tower shape (see the red contour) and maximum temperatures of $T \sim 2$–3 MK; and the surge, which is the cool and elongated structure, as in NS2016, located on the right side of the dome. The surge has been produced by a peeling-like mechanism during the nonstationary magnetic reconnection process. This process drags away and ejects plasma from the dome, sometimes as plasmoids, giving rise to structures that resemble crests. The inner part of the surge is composed of elongated thread-like structures of different density that are a consequence of the collision and subsequent merging of plasmoids with the surge. Besides that, there is also a detachment mechanism that splits and separates the surge from the emerged dome (see the details about this process in NS2016). This occurs at a height of around 5 or 6 Mm on the side of the surge closest to the reconnection site, referred to in the following as the *internal side* of the surge. Consequently, we call that region the *internal footpoint* of the surge (as marked by an arrow in the figure). Another interesting region for the comparison with the observations is the base of the external region of the surge: we call this the external footpoint of the numerical surge, and it is marked by another arrow in the figure. In panel (B), the slanted experiment, the emerged dome is located at $10 \leqslant x \leqslant 20$ Mm, and the coronal jet has lower temperatures ($T < 1.2$ MK). In this case, the surge does not end up totally detaching from the dome, which could be a consequence of the magnetic field configuration in the corona. In the follow-up paper (D. Nóbrega-Siverio et al. 2017, in preparation), an in-depth study of the physics taking place in this phenomenon is carried out, including the role of the entropy sources and the consequences of the NEQ ionization of silicon and oxygen for the emissivity.

4.2. Analysis of the Synthetic Spectra

With a view to identifying the different observational features explained in the paper (Section 3.2) with structures and phenomena in the experiments, in the following, we

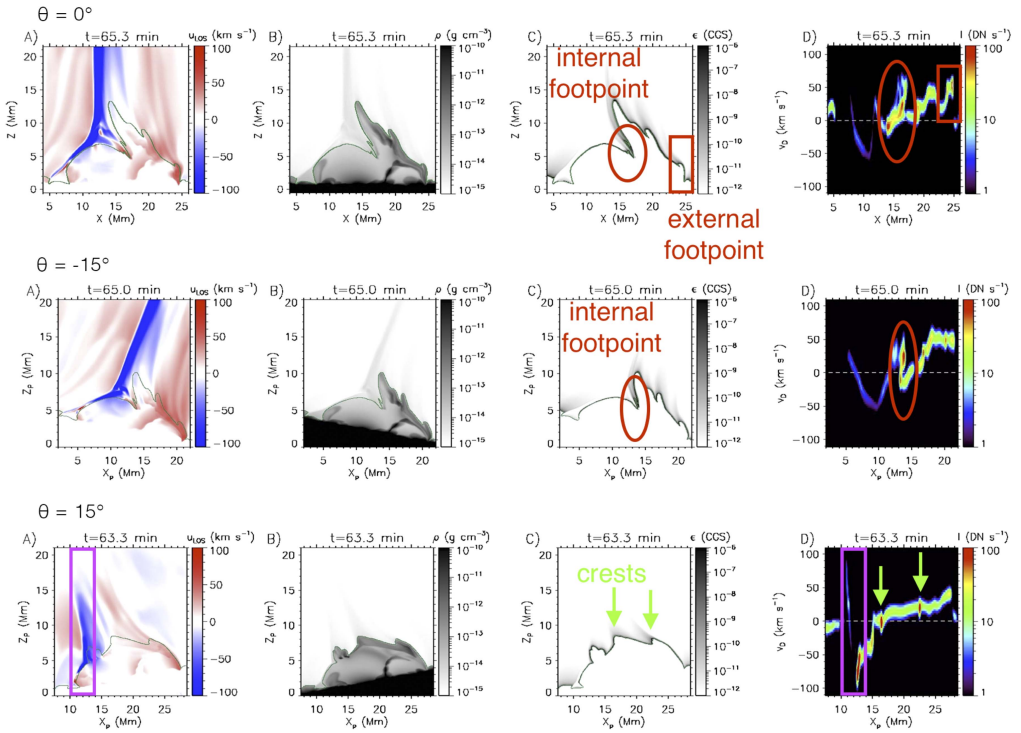

Figure 6. 2D maps of the vertical experiment at different times for various LOS θ. (A) Velocity along the LOS, $u_{\rm LOS}$; (B) density, ρ; (C) emissivity, ϵ, for Si IV in CGS units (erg cm^{-3} sr^{-1} s^{-1}); and (D), synthetic spectral intensity, I (see Equation (1)), along the LOS θ. Temperature of the peak emission for SE ($\log(T) = 4.90$ K) is overplotted as a green contour. In the $\theta \neq 0$ rows, Z_p and X_P are, respectively, the vertical and horizontal coordinates of the rotated figures. The animation of this figure shows the time evolution of the surge from its origin ($t = 61$ minute) up to its decay phase ($t = 70.7$ minute) in the vertical experiment for the three LOS.
(An animation of this figure is available.)

analyze the synthetic Si IV 1402.77 Å spectra obtained from the numerical data. The surge in the experiments produces spectral features that resemble those from Region R1 in the *IRIS* Si IV observations (Section 3.2.1). In turn, the region near the magnetic reconnection site, whose location is marked in Figure 5 for both experiments, produces spectral features that resemble the burst (R2) described in Section 3.2.2. In order to establish the relation between the numerical and observational features for the surge and burst, we use Figures 6 and 7, which correspond to the vertical and slanted magnetic field experiments respectively. The different rows correspond to different inclination angles for the LOS. Exploring different inclinations is important since they impact the obtained intensities as seen in the following. The panels in each row contain (A) the velocity along the LOS, $u_{\rm LOS}$; (B) the density, ρ; (C) the Si IV emissivity, ϵ; and (D) the synthetic spectral intensity, I, derived from Equation (1). In the $\theta \neq 0$ panels, x_P and z_P are, respectively, the horizontal and vertical coordinates of the rotated figures. Note that, to facilitate the explanation, we are choosing somewhat different times for each row. Animations of the Figures 6 and 7 are provided online.

4.2.1. The Surge

In the following, we separately analyze various characteristic regions of the surge.

(a) The internal footpoint. For the vertical field experiment (Figure 6, $\theta = 0°$ and $\theta = -15°$), in panel (D) at $x \sim 16.5$ Mm and $x_P \sim 13.5$ Mm, respectively, there is a typical spectrum of the internal footpoint obtained through integration along an LOS near and parallel to the transition region at the internal boundaries of the surge. Regarding the slanted experiment (Figure 7, $\theta = 0°$ row), in panel (D), approximately between $11 \leqslant x \leqslant 14$ Mm, we can see also a clear example of the spectrum emanating from the internal footpoint of the surge. This region is composed of plasma strongly emitting in Si IV, (see panels C) that during the event moves from the reconnection site to the internal footpoint. The plasma here is mostly descending due to the enhanced pressure gradient that pushes it down when going through the post-shock region (see NS2016); as a consequence, the spectra show mainly redshifted profiles. We note that the internal footpoint is usually brighter than the rest

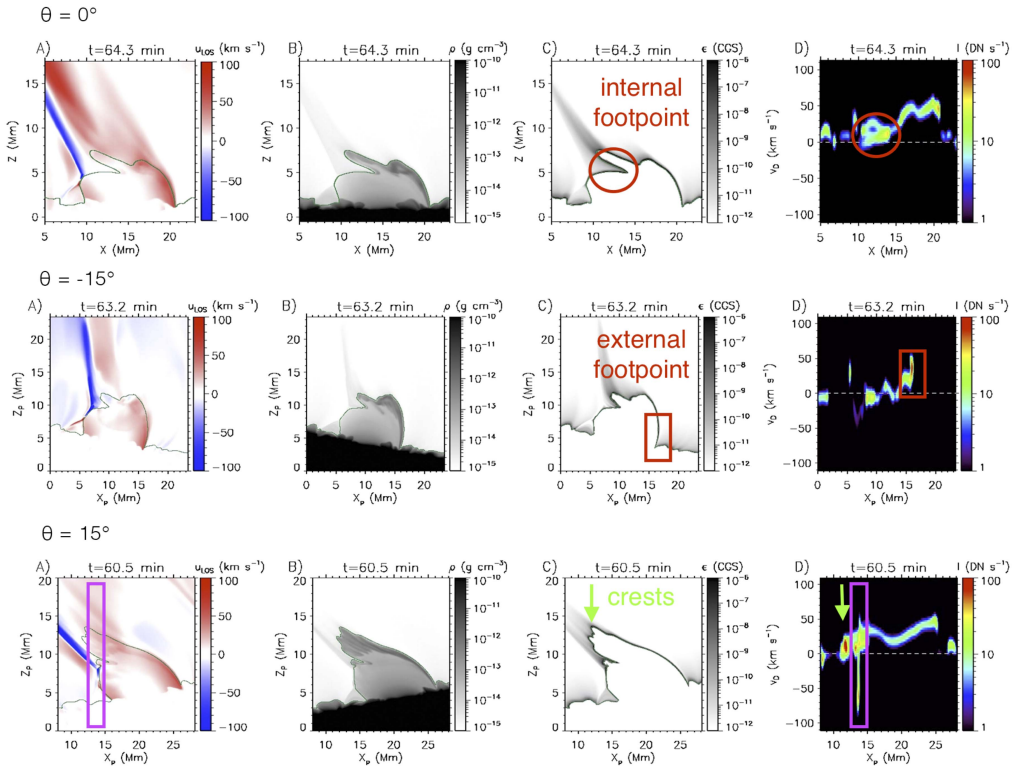

Figure 7. Same 2D maps as in Figure 6 but for the slanted experiment. The animation of this figure shows the time evolution of the surge from its origin (in this case, $t = 58$ minute) up to its decay phase ($t = 68$ minute) for the three LOS.

(An animation of this figure is available.)

of the surge. In the animations of the vertical experiment, we can see that the intensity of this region varies depending on the LOS and can be greatly enhanced when integrating parallel to the transition region of the internal footpoint.

The features mentioned above fit with the results of the *IRIS* observation (Section 3.2.1) for region R1a (the brightest region within the surge), which is mostly located around the observational footpoints. The deviations from this behavior are explained in the subsequent items.

(b) The external footpoint. Figure 6 shows that in that region (marked in the figure by a red rectangle) we can also find brightenings with intensities between 30 and 112 DN s^{-1}. The intensity depends again on the geometry, i.e., it is enhanced when the parallel direction of the transition region of the surge coincides with the LOS. This dependence can be checked by looking at the three different LOS θ of the same figure. In this region, the Doppler shift v_D has values around 20–60 km s^{-1} to the red. A similar result is found for the external footpoint of the slanted experiment (see, e.g., the region marked with the circle in the row $\theta = -15^\circ$ of Figure 7).

Concerning the observations, the above result strengthens the conclusion of Section 3.2.1 that bright Si IV points within the surge are mostly located at its footpoints. Note that in the current observations we cannot distinguish whether the brightenings of R1a come from the internal or external footpoints.

(c) The crests. Representative cases for the spectra of the surge *crests* can be found in the $\theta = 15^\circ$ row of the vertical experiment (marked with green arrows in Figure 6), which shows: (a) a crest in its ascending phase approximately at $x_P = 15$ Mm, with intensities around 40 DN s^{-1} and blueshifted; (b) a much brighter one with blue and redshifted components although with small velocities ($x_P = 17$ Mm); and (c) the last one, which is also bright but only shows redshift ($x_P = 22.5$ Mm). At $x_P = 13.0$ Mm, the magnetic reconnection process is leading to another crest as a result of the ejection of plasma upwards with large velocities (see panel (A)). Regarding the slanted experiment (Figure 7), the $\theta = 15^\circ$ row shows a crest example between $11 \leqslant x_P \leqslant 13$ Mm. In this case, we find that before $t = 59.0$ minute, the crest is a bright feature on the blue side of the spectrum with

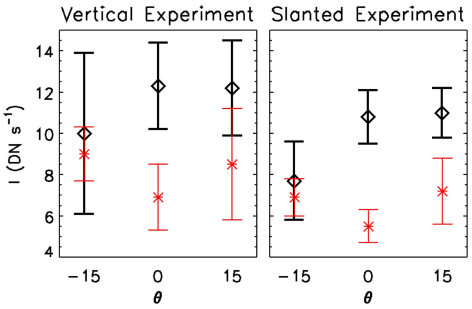

Figure 8. Average intensities for the three different LOSs of the less bright regions of the surge (black diamonds) and of the *quiet* transition region (red asterisks) for both experiments. The error bars are obtained from the standard deviation.

absolute v_D of <30 km s^{-1}; nonetheless, as time advances on (e.g., $t = 60.5$ minute), the whole surge falls down and the crest then shows redshifted profiles with velocities on the same order. At later stages of the evolution, the crest moves to the right side of the dome and it is not easy to isolate it to integrate the emissivity without going through other interesting sites like the magnetic reconnection region.

With respect to the comparison with the observations, in Section 3.2.1, we argued that R1a, which was defined as the pixel with the brightest Si IV emission within the surge, although mostly located near the footpoints, can sometimes be found further away. Now we realize that those excursions from the observational footpoint region can correspond to instants in which the brightest Si IV emission is produced in the crests of the surge instead of in the footpoints themselves.

(d) The rest of the surge. Let us focus now on the less bright regions of the surge. In Figures 6 and 7, we see that the lowest intensities within the surge are ∼10 DN s^{-1}. We would like to explore whether even those regions are intrinsically brighter or not than an average transition region. In order to show this quantitatively, we have carried out a statistical analysis in *quiet* transition regions, i.e., places far away from the locations affected by the magnetic reconnection and the subsequent surge. In those regions, we calculate the average peak intensity during 10 minutes; in the less bright regions of the surge, we average the minimum of the peak intensities within the numerical surge, also during 10 minutes. The resulting intensities and their standard deviations are shown in Figure 8 for the three LOSs used in the experiments. The diamonds correspond to the less bright regions of the surge; the asterisks correspond to the *quiet* transition region. Comparing those values, one could tentatively conclude that even the less bright regions of the surge seem to be slightly brighter than an average transition region; nonetheless, that statement is not fully conclusive given the large size of the standard deviation in some of the cases.

Concerning the *IRIS* observations, the fixed position R1b (Section 3.2.1) showed that in Si IV the surge was brighter than the average by a factor of 1.9 (see Table 1). In fact, in Figure 4 and the associated movie, the whole surge is above the peak intensity of the average profile. In the numerical experiments, the comparison between intensities from a *quiet* transition region and the less bright regions in the surge tentatively appears to be in accordance with the observations, although more statistics from other experiments would be needed for a stronger conclusion.

4.2.2. The Burst

After analyzing the spectra of the surge, in this section, we describe the associated burst. In our numerical experiments, we have associated the burst with being the reconnection site. This identification is due to the similarity between the observed features and what is explained in the following. Further evidence of the relation between the reconnection site and bursts is found in the recent paper by Hansteen et al. (2017), where the authors show, through synthesis diagnostics of 3D simulations, that the bursts can be triggered in the mid and low chromosphere owing to the reconnection between different emerging bipolar magnetic fields.

In this paper, a good example of the burst is found at $x_P = 14$ Mm for the slanted experiment (Figure 7) for $\theta = 15°$, which is an LOS parallel to the transition region at the reconnection site. Panel (A) shows that in that region (pink rectangle) there is a bidirectional flow with large upflow velocities, up to 85 km s^{-1}, and downflow velocities of <60 km s^{-1}. In panel (D), we notice that the corresponding synthetic profile shares characteristics described in the observation for R2b (the brightest region of the Si IV burst): broad profiles with both red and blue components reaching large Doppler shifts. In the accompanying movie, we see that the blue component is usually brighter than the red one, which is also something found in the observation (see Section 3.2.2). Turning now to the vertical experiment, an example of the burst in a direction not parallel to the reconnection site can be found in the $\theta = 15°$ row of Figure 6. Within the pink rectangle in panel (A), we see a downflow between $10.0 \leqslant x_P \leqslant 11.5$ Mm, and a strong upflow around $11.5 \leqslant x_P \leqslant 13.0$ Mm. The synthetic intensity shows large Doppler shifts for both components but with the blue component being brighter. In both experiments, we see that the plasma emitting in Si IV moves from the reconnection site to the detachment region where the internal footpoint of the surge is formed. This pattern of motion occurs repeatedly, a feature also found in the observation in R2b (see the second bullet point of Section 3.2.2). Finally, in the vertical experiment, there are also complex profiles due to the formation of plasmoids and subsequent cascade. The latter feature is addressed in more detail by Rouppe van der Voort et al. (2017) using the vertical numerical experiment and comparing it with plasmoids observed with CHROMIS at the SST.

5. Discussion

In this paper, we have used coordinated observations from *IRIS* and SST to study an Hα surge and accompanying Si IV burst episode occuring in active region AR 12585 on 2016 September 03. During the event, we found for the first time emission of Si IV within the surge and provide details about the properties of the surge and burst. In order to give a theoretical interpretation of the observations, we performed 2.5D RMHD numerical experiments of magnetic flux emergence through the

granular cells right below the surface up to the atmosphere. The experiments were carried out with Bifrost using an extra module of the code that calculates the Si IV population in NEQ ionization. During the experiments, surges and bursts are obtained as a direct and indirect consequence of magnetic reconnection processes. We then compute synthetic spectra and compare with the observations.

In the following, we discuss some observational and theoretical features of the surge and burst and also some limitations of the present research.

5.1. Observations

Analyzing the light curves (Section 3.1), we have detected that in this case the surge and Si IV burst can be linked spatially and temporally to opposite polarity patches that converge and collide. Moreover, an EB is visible in close vicinity just prior to the start of the burst and remains active during the whole lifetime of the burst. It appears likely that all of these different phenomena share a common physical origin.

The most striking feature of the observation is the finding of emission in Si IV within the surge. Previous papers (e.g., Kim et al. 2015 and Huang et al. 2017) had only addressed the coexistence of surges, seen in Hα and Ca II 8542 Å, and Si IV brightenings, but without identifying evidences of Si IV within the surge. Our finding implies that surges, which are traditionally associated with chromospheric lines, have enough impact in the transition region to be detectable. Furthermore, this result together with the one by Madjarska et al. (2009), where the surge was associated with highly non-Gaussian line profiles in O V and N V, qualitatively increases the interest of studying transition region lines for diagnosis of chromospheric phenomena. The Si IV emission found in our surge is not strong, its intensity is around a factor of 2–5 brighter than a quiet-Sun typical Si IV profile, and sporadic: we detect it mostly in the rising phase of the surge, when it is visible in the blue wing of Hα (Section 3.2.1). The lack of Si IV in the decay phase of the surge may be due to cooling of the plasma so it is no longer emitting in Si IV or too weak to be detectable in short exposure time observations like the present one. Another interesting feature is that the brightest emission in Si IV within the domain of the surge is located near its footpoints. Moreover, the profiles are mainly redshifted with asymmetries to the blue. This reflects the complexity of the surge region, where in the same LOS we can find cool surge plasma visible in the blue wing of Hα, which indicates rising motion, and hotter plasma emitting in Si IV, that is mainly descending, while there is a small fraction of large upflow velocities relative to the profile peak. The surge is otherwise of a canonical type: it is visible as an elongated and dark structure first in the blue and then in the red wings of Hα and Ca II, with projected lengths of several megameters, and Doppler velocities of a few tens of kilometers per second (Section 3.1). Concerning the Si IV burst (Section 3.2.2), we see typical burst characteristics as reported in the literature: the burst appears in regions on the surface where magnetic flux regions of opposite polarity converge and collide, it has broad profiles due to the presence of blue and red components, absorption features superimposed on the Si IV lines, brightenings in the wings of Mg II h and k lines with small enhancement in the cores, and enhanced wings in Hα.

A full multi-diagnostic study of surges is challenging since it requires coordinated observations from different instruments. Moreover, full spectral coverage requires the *IRIS* raster to coincide both spatially and temporally with the region where the events are occurring, which reduces the number of available observations for a statistical analysis. In our case, a severe limitation is the short exposure time of this observation (0.5 s), so lines like O IV 1401.2 and 1399.8 Å cannot be used for density diagnostics since they require longer exposure times to be detectable (De Pontieu et al. 2014). Furthermore, the raster does not cover the whole surge, so we do not have a complete data set of the surge for a more complete comparison and questions about the emissivity in Si IV at the upper part of the surge remain open.

5.2. Numerical Experiments

In the paper, Si IV spectral synthesis has been used for the first time to study surges (Section 4.2.1) and the associated burst (Section 4.2.2). We have found that our models are able to reproduce some of the main features of the observations as summarized in the following.

1. The brightest points in Si IV within the surge correspond to the location around the footpoints of the surge. The excursions of the brightest patch from the observed surge footpoints are identified with the crests in the surge.
2. The synthetic Si IV profiles obtained in the experiment for the surge are mainly redshifted and the values fit with the observed Doppler shifts.
3. The less bright regions of the surge in Si IV seem to be brighter than an average transition region and match tentatively with what was found in the observations.
4. Our experiments provide a temporal and spatial relation between the surge and the burst. Both are a natural consequence of magnetic reconnection between emerged plasma and the pre-existing coronal magnetic field.
5. The motions observed with *IRIS* from the brightest region in the Si IV burst to the surge footpoints can be identified in the numerical experiments through plasma strongly emitting in Si IV that moves from the reconnection site to the internal footpoint of the surge.
6. The two-component profiles of the observed burst are characterized by large velocities and by the fact that the blue component is usually brighter than the red one: this is also found in the numerical experiments. The main difference between theory and observations concerns the burst intensity, which is substantially larger in the observations. A possible reason for the discrepancy is the lack of numerical resolution (Innes et al. 2015; Guo et al. 2017).

In the numerical experiments, we see that the orientation of the LOS plays an important role for the diagnosis. The resulting spectral intensity in the transition region lines can be enhanced by an important factor when the LOS runs parallel (or almost) to the local transition region. This is something to take into account for future interpretations from observations.

In spite of the good agreement with the observations, our current numerical experiments are not free from limitations, which are related to the challenging conditions in chromospheric plasma and associated radiative transfer. The experiments lack nonequilibrium ionization of hydrogen and helium, which could impact the properties of the emerged plasma and subsequent surge (Leenaarts et al. 2007; Golding et al. 2014). They also lack ambipolar diffusion, which has recently been shown to be key to obtaining related phenomena, like type II spicules (Martínez-Sykora et al. 2017). Moreover, our

experiments are 2.5D, but 3D modeling would be necessary to capture the full complexity of those phenomena, as was shown recently for bursts and EBs by Hansteen et al. (2017), and to be able to accurately synthesize the Hα line (Leenaarts et al. 2012). Proper Hα synthesis is important, e.g., to identify the numerical threads in the inner part of the surge (Section 4.1) with observed thread-like structures (Nelson & Doyle 2013; Li et al. 2016), or to provide a theoretical explanation for the shocks associated with surges (Yang et al. 2014).

We gratefully acknowledge financial support from the Spanish Ministry of Economy and Competitiveness (MINECO) through projects AYA2011-24808 and AYA2014-55078-P, as well as from NASA contract NNG09FA40C (*IRIS*) and NASA grants NNH15ZDA001N-HSR and NNX16AG90G. *IRIS* is a NASA small explorer mission developed and operated by LMSAL with mission operations executed at NASA Ames Research center and major contributions to downlink communications funded by ESA and the Norwegian Space Centre. The Swedish 1-m Solar Telescope is operated on the island of La Palma by the Institute for Solar Physics (ISP) of Stockholm University in the Spanish Observatorio del Roque de los Muchachos of the Instituto de Astrofísica de Canarias. We also acknowledge the computer resources and assistance provided at the MareNostrum (BSC/CNS/RES, Spain) and TeideHPC (ITER, Spain) supercomputers. Finally, the authors are grateful to Gregal Vissers for his constructive comments during the Hinode-11/*IRIS*-8 science meeting.

ORCID iDs

D. Nóbrega-Siverio https://orcid.org/0000-0002-7788-6482
J. Martínez-Sykora https://orcid.org/0000-0002-0333-5717
L. Rouppe van der Voort https://orcid.org/0000-0003-2088-028X

References

Asai, A., Ishii, T. T., & Kurokawa, H. 2001, ApJL, 555, L65
Bong, S.-C., Cho, K.-S., & Yurchyshyn, V. 2014, JKAS, 47, 311
Brooks, D. H., Kurokawa, H., & Berger, T. E. 2007, ApJ, 656, 1197
Canfield, R. C., Reardon, K. P., Leka, K. D., et al. 1996, ApJ, 464, 1016
Cao, T.-j., Xu, A.-a., & Tang, Y.-h. 1980, ChA, 4, 143
Carlsson, M., & Leenaarts, J. 2012, A&A, 539, A39
Chae, J., Qiu, J., Wang, H., & Goode, P. R. 1999, ApJL, 513, L75
Chen, H. D., Jiang, Y. C., & Ma, S. L. 2008, A&A, 478, 907
de la Cruz Rodriguez, J. 2010, PhD thesis, Stockholm Univ.
de la Cruz Rodríguez, J., Löfdahl, M. G., Sütterlin, P., Hillberg, T., & Rouppe van der Voort, L. 2015, A&A, 573, A40
de la Cruz Rodríguez, J., Socas-Navarro, H., Carlsson, M., & Leenaarts, J. 2012, A&A, 543, A34
De Pontieu, B., McIntosh, S., Martinez-Sykora, J., Peter, H., & Pereira, T. M. D. 2015, ApJL, 799, L12
De Pontieu, B., McIntosh, S. W., Hansteen, V. H., & Schrijver, C. J. 2009, ApJL, 701, L1
De Pontieu, B., Title, A. M., Lemen, J. R., et al. 2014, SoPh, 289, 2733
Gaizauskas, V. 1996, SoPh, 169, 357
Golding, T. P., Carlsson, M., & Leenaarts, J. 2014, ApJ, 784, 30
Grubecka, M., Schmieder, B., Berlicki, A., et al. 2016, A&A, 593, A32
Gu, X. M., Lin, J., Li, K. J., et al. 1994, A&A, 282, 240
Gudiksen, B. V., Carlsson, M., Hansteen, V. H., et al. 2011, A&A, 531, A154
Guglielmino, S. L., Bellot Rubio, L. R., Zuccarello, F., et al. 2010, ApJ, 724, 1083
Guo, L.-J., De Pontieu, B., & Peter, H. 2017, Natur, submitted
Gupta, G. R., & Tripathi, D. 2015, ApJ, 809, 82
Hansteen, V. H., Archontis, V., Pereira, T. M. D., et al. 2017, ApJ, 839, 22
Hayek, W., Asplund, M., Carlsson, M., et al. 2010, A&A, 517, A49
Huang, Z., Madjarska, M. S., Scullion, E. M., et al. 2017, MNRAS, 464, 1753
Innes, D. E., Guo, L.-J., Huang, Y.-M., & Bhattacharjee, A. 2015, ApJ, 813, 86
Jiang, Y. C., Chen, H. D., Li, K. J., Shen, Y. D., & Yang, L. H. 2007, A&A, 469, 331
Jibben, P., & Canfield, R. C. 2004, ApJ, 610, 1129
Judge, P. G. 2015, ApJ, 808, 116
Kim, Y.-H., Yurchyshyn, V., Bong, S.-C., et al. 2015, ApJ, 810, 38
Kirshner, R. P., & Noyes, R. W. 1971, SoPh, 20, 428
Kurokawa, H., Liu, Y., Sano, S., & Ishii, T. T. 2007, in ASP Conf. Ser. 369, New Solar Physics with Solar-B Mission, ed. K. Shibata, S. Nagata, & T. Sakurai (San Francisco, CA: ASP), 347
Leenaarts, J., Carlsson, M., Hansteen, V., & Rutten, R. J. 2007, A&A, 473, 625
Leenaarts, J., Carlsson, M., & Rouppe van der Voort, L. 2012, ApJ, 749, 136
Li, Z., Fang, C., Guo, Y., et al. 2016, ApJ, 826, 217
Liu, W., Berger, T. E., Title, A. M., & Tarbell, T. D. 2009, ApJL, 707, L37
Liu, Y., & Kurokawa, H. 2004, ApJ, 610, 1136
Madjarska, M. S., Doyle, J. G., & de Pontieu, B. 2009, ApJ, 701, 253
Martínez-Sykora, J., De Pontieu, B., Hansteen, V., & McIntosh, S. W. 2011, ApJ, 732, 84
Martínez-Sykora, J., De Pontieu, B., Hansteen, V. H., et al. 2017, Sci, 356, 1269
Martínez-Sykora, J., De Pontieu, B., Hansteen, V. H., & Gudiksen, B. 2016, ApJ, 817, 46
Nelson, C. J., & Doyle, J. G. 2013, A&A, 560, A31
Nishizuka, N., Shimizu, M., Nakamura, T., et al. 2008, ApJL, 683, L83
Nóbrega-Siverio, D., Moreno-Insertis, F., & Martínez-Sykora, J. 2016, ApJ, 822, 18
Olluri, K., Gudiksen, B. V., & Hansteen, V. H. 2013a, ApJ, 767, 43
Olluri, K., Gudiksen, B. V., & Hansteen, V. H. 2013b, AJ, 145, 72
Olluri, K., Gudiksen, B. V., Hansteen, V. H., & De Pontieu, B. 2015, ApJ, 802, 5
Ortiz, A., Bellot Rubio, L. R., Hansteen, V. H., de la Cruz Rodríguez, J., & Rouppe van der Voort, L. 2014, ApJ, 781, 126
Pereira, T. M. D., Carlsson, M., De Pontieu, B., & Hansteen, V. 2015, ApJ, 806, 14
Peter, H., Tian, H., Curdt, W., et al. 2014, Sci, 346, 1255726
Polito, V., Del Zanna, G., Dudík, J., et al. 2016, A&A, 594, A64
Robustini, C., Leenaarts, J., de la Cruz Rodriguez, J., & Rouppe van der Voort, L. 2016, A&A, 590, A57
Rouppe van der Voort, L., De Pontieu, B., Pereira, T. M. D., Carlsson, M., & Hansteen, V. 2015, ApJL, 799, L3
Rouppe van der Voort, L., De Pontieu, B., Scharmer, G. B., et al. 2017, ApJL, submitted
Roy, J.-R. 1973, SoPh, 32, 139
Rust, D. M. 1976, RSPTA, 281, 353
Rutten, R. J., Vissers, G. J. M., Rouppe van der Voort, L. H. M., Sütterlin, P., & Vitas, N. 2013, Journal of Physics Conference Series, 440, 012007
Scharmer, G. B. 2006, A&A, 447, 1111
Scharmer, G. B., Bjelksjo, K., Korhonen, T. K., Lindberg, B., & Petterson, B. 2003, Proc. SPIE, 4853, 341
Schmahl, E. J. 1981, SoPh, 69, 135
Schmieder, B., Mein, P., Martres, M. J., & Tandberg-Hanssen, E. 1984, SoPh, 94, 133
Schmieder, B., Shibata, K., van Driel-Gesztelyi, L., & Freeland, S. 1995, SoPh, 156, 245
Schmit, D. J., Innes, D., Ayres, T., et al. 2014, A&A, 569, L7
Shimizu, T., Katsukawa, Y., Kubo, M., et al. 2009, ApJL, 696, L66
Tian, H., McIntosh, S. W., De Pontieu, B., et al. 2011, ApJ, 738, 18
Tian, H., Xu, Z., He, J., & Madsen, C. 2016, ApJ, 824, 96
Uddin, W., Schmieder, B., Chandra, R., et al. 2012, ApJ, 752, 70
van Noort, M., Rouppe van der Voort, L., & Löfdahl, M. G. 2005, SoPh, 228, 191
Vargas Domínguez, S., Kosovichev, A., & Yurchyshyn, V. 2014, ApJ, 794, 140
Vissers, G. J. M., Rouppe van der Voort, L. H. M., & Rutten, R. J. 2013, ApJ, 774, 32
Vissers, G. J. M., Rouppe van der Voort, L. H. M., Rutten, R. J., Carlsson, M., & De Pontieu, B. 2015, ApJ, 812, 11
Wang, J. f., Zhou, T. h., & Ji, H. s. 2014, ChA&A, 38, 65
Watanabe, H., Vissers, G., Kitai, R., Rouppe van der Voort, L., & Rutten, R. J. 2011, ApJ, 736, 71
Yang, H., Chae, J., Lim, E.-K., et al. 2013, SoPh, 288, 39
Yang, H., Chae, J., Lim, E.-K., et al. 2014, ApJL, 790, L4
Zhang, J., Wang, J., & Liu, Y. 2000, A&A, 361, 759
Zhang, Q. M., & Ji, H. S. 2014, A&A, 561, A134
Zhelyazkov, I., Zaqarashvili, T. V., Chandra, R., Srivastava, A. K., & Mishonov, T. 2015, AdSpR, 56, 2727

4

On the importance of the nonequilibrium ionization of Si IV and O IV and the line-of-sight in solar surges

In the previous chapter, we found Si IV emission within the observed surge and analyzed its different signatures. Additionally, as a first approach to explain the observational findings, we performed forward modeling of our numerical models. Thanks to that, in the synthetic spectral profiles we found some counterparts with the observational features, e.g., the location of the Si IV brightenings within the surge and the characteristic Doppler shifts. However, there was an open question concerning the theoretical explanation of the origin of those spectral features and the reason for the enhanced brightness in the surge was missing. For this reason, the aim of this chapter is to reconcile theoretical-numerical experiments with observations, carrying out a thorough analysis of our realistic models to faithfully explain not only the observations shown in Chapter 3, but also to provide predictions for future ones. To that end, we buried ourself in the already presented 2.5D numerical experiments that contain NEQ ionization of silicon. Moreover, in order to step forward in the theoretical knowledge of surges, an improvement was introduced by also including the NEQ ionization of oxygen. We highlight the relevance of taking into account departures from statistical equilibrium in the number density of the main ions of silicon and oxygen in the transition region. Through statistical analysis, we show the differences of the UV emissivity within the surge with respect to a quiet-sun TR. In addition, based on the spectral synthesis of our numerical data, we address the relevance of line-of-sight effects when studying optically thin lines for surges.

The results and conclusions of this chapter are summarized in the following:

- The main result of this chapter is the finding that assuming statistical equilibrium in the computations would produce an absence of Si IV and O IV ions in most of the TR

of the surge. We consequently conclude that the consideration of NEQ is necessary to get the proper population levels of the ions and, therefore, the right emissivity to interpret TR observations of surges.

- Through a statistical analysis of the layers with the highest emission in relevant lines of Si IV and O IV, we find that the surge emits in Si IV more than a standard TR, which could explain why we could detect Si IV within the surge domain in the IRIS observations of the previous chapter, and has a larger emissivity ratio of Si IV to O IV.
- By means of detailed Lagrange tracing, we are able to determine the sources of the enhanced emissivity in the plasma. In particular, we see that during the surge formation, optically thin losses and heat conduction are key mechanisms with very short timescales that lead to large departures from statistical equilibrium.
- Finally, we calculate synthetic profiles to understand previous observational results and predict future ones, concluding that line-of-sight effects have important implications for surges observations: given the involved geometry of the surge, the line-of-sight can cut the emitting layer at small angles and/or cross it multiple times, causing prominent, spatially intermittent brightenings both in Si IV and O IV.

The above results and conclusions were published by Nóbrega-Siverio et al. (2018) in May 2018 in the volume 858 of *The Astrophysical Journal (ApJ)* with the title **On the Importance of the Nonequilibrium Ionization of Si IV and O IV and the line-of-sight in Solar Surges**. This paper is attached in the following pages and can also be found in the ADS:
`http://adsabs.harvard.edu/abs/2018ApJ...858....8N`

The Astrophysical Journal, 858:8 (16pp), 2018 May 1 https://doi.org/10.3847/1538-4357/aab9b9

On the Importance of the Nonequilibrium Ionization of Si IV and O IV and the Line of Sight in Solar Surges

D. Nóbrega-Siverio[1,2], F. Moreno-Insertis[1,2], and J. Martínez-Sykora[3,4]
[1] Instituto de Astrofisica de Canarias, Via Lactea, s/n, E-38205 La Laguna (Tenerife), Spain; dnobrega@iac.es, fmi@iac.es
[2] Department of Astrophysics, Universidad de La Laguna, E-38200 La Laguna (Tenerife), Spain
[3] Lockheed Martin Solar and Astrophysics Laboratory, Palo Alto, CA 94304, USA; juanms@lmsal.com
[4] Bay Area Environmental Research Institute, Moffett Field, CA 94035, USA
Received 2018 February 26; revised 2018 March 23; accepted 2018 March 23; published 2018 April 26

Abstract

Surges are ubiquitous cool ejections in the solar atmosphere that often appear associated with transient phenomena like UV bursts or coronal jets. Recent observations from the *Interface Region Imaging Spectrograph* show that surges, although traditionally related to chromospheric lines, can exhibit enhanced emission in Si IV with brighter spectral profiles than for the average transition region (TR). In this paper, we explain why surges are natural sites to show enhanced emissivity in TR lines. We performed 2.5D radiative-MHD numerical experiments using the Bifrost code including the nonequilibrium (NEQ) ionization of silicon and oxygen. A surge is obtained as a by-product of magnetic flux emergence; the TR enveloping the emerged domain is strongly affected by NEQ effects: assuming statistical equilibrium would produce an absence of Si IV and O IV ions in most of the region. Studying the properties of the surge plasma emitting in the Si IV λ1402.77 and O IV λ1401.16 lines, we find that (a) the timescales for the optically thin losses and heat conduction are very short, leading to departures from statistical equilibrium, and (b) the surge emits in Si IV more and has an emissivity ratio of Si IV to O IV larger than a standard TR. Using synthetic spectra, we conclude the importance of line-of-sight effects: given the involved geometry of the surge, the line of sight can cut the emitting layer at small angles and/or cross it multiple times, causing prominent, spatially intermittent brightenings in both Si IV and O IV.

Key words: magnetohydrodynamics (MHD) – methods: numerical – Sun: atmosphere – Sun: chromosphere – Sun: transition region

Supporting material: animations

1. Introduction

The solar atmosphere contains a wide variety of chromospheric ejections that cover a large range of scales: from the smallest ones with maximum size of a few megameters, such as penumbral microjets (e.g., Katsukawa et al. 2007; Drews & Rouppe van der Voort 2017) or spicules (Hansteen et al. 2006; De Pontieu et al. 2007; Pereira et al. 2012, among others), up to ejections that can reach, in extreme cases, several tens of megameters, like surges (e.g., Canfield et al. 1996; Kurokawa et al. 2007; Guglielmino et al. 2010; Yang et al. 2014) and macrospicules (Bohlin et al. 1975; Georgakilas et al. 1999; Murawski et al. 2011; Kayshap et al. 2013). Surges, in particular, are often associated with magnetic flux emergence from the solar interior. They are typically observed as darkenings in images taken in the Hα blue/red wings with line-of-sight (LOS) velocities of a few to several tens of kilometers per second, and they are usually related to other explosive phenomena like EUV and X-ray jets, UV bursts, and Ellerman bombs (see Nóbrega-Siverio et al. (2017, hereafter NS2017, and references therein). Although observationally known for several decades now, the understanding of surges has progressed slowly, and various aspects, such as their impact on the transition region (TR) and corona concerning the mass and energy budget, are still poorly known.

From the theoretical point of view, the first explanation of the surge phenomenon came through 2.5D numerical models (Shibata et al. 1992; Yokoyama & Shibata 1995, 1996), where a cold ejection was identified next to a hot jet as a consequence of a magnetic reconnection process between the magnetic field in plasma emerged from the interior and the preexisting coronal field. Nishizuka et al. (2008) used a similar numerical setup to associate the surge with jet-like features seen in Ca II H + K observations by means of morphological image comparisons. Further 2.5D models that include the formation of a cool chromospheric ejection are those of Jiang et al. (2012) (canopy-type coronal magnetic field) and Yang et al. (2013, 2018), who study the cool jets resulting from the interaction between moving magnetic features at the base of their experiment and the preexisting ambient field in the atmosphere. Turning to 3D models, in the magnetic flux emergence experiment of Moreno-Insertis & Galsgaard (2013), a dense wall-like surge appeared surrounding the emerged region, with temperatures from 10^4 K to a few times 10^5 K and speeds around 50 km s^{-1}. MacTaggart et al. (2015) found similar velocities for the surges in their 3D model of flux emergence in small-scale active regions. The availability of a radiation-MHD code like Bifrost (Gudiksen et al. 2011) has opened up the possibility of much more detailed modeling of the cool ejections than before. Bifrost has a realistic treatment of the material properties of the plasma, calculates the radiative transfer in the photosphere and chromosphere, and includes the radiative and heat conduction entropy sources in the corona. Using that code, Nóbrega-Siverio et al. (2016, hereafter NS2016) argued that entropy sources play an important role during the surge formation and showed that a relevant fraction of the surge could not be obtained in previous and more idealized experiments.

The realistic treatment of surges may require an even larger degree of complication. The solar atmosphere is a highly dynamical environment; the evolution sometimes occurs on

The Astrophysical Journal, 858:8 (16pp), 2018 May 1

short timescales that bring different atomic species out of equilibrium ionization, thus complicating both the modeling and the observational diagnostics (e.g., Griem 1964; Raymond & Dupree 1978; Joselyn et al. 1979; Hansteen 1993). For hydrogen, for instance, using 2D numerical experiments, Leenaarts et al. (2007, 2011) found that the temperature variations in the chromosphere can be much larger than for statistical equilibrium (SE), which has an impact on, e.g., its coolest regions (the so-called cool pockets). For helium, Golding et al. (2014, 2016) described how nonequilibrium (NEQ) ionization leads to higher temperatures in wavefronts and lower temperatures in the gas between shocks. For heavy elements, Bradshaw & Mason (2003), Bradshaw & Cargill (2006), Bradshaw & Klimchuk (2011), and Reep et al. (2016) showed, through 1D hydrodynamic simulations, that there are large departures from SE balance in cooling coronal loops, nanoflares, and other impulsive heating events that affect the EUV emissivity. Through 3D experiments, Olluri et al. (2013b) found that deduced electron densities for O IV can be up to an order of magnitude higher when NEQ effects are taken into account. Also in 3D, Olluri et al. (2015) discussed the importance of the NEQ ionization of coronal and TR lines to reproduce absolute intensities, line widths, and ratios, among others, observed by, e.g., Chae et al. (1998), Doschek (2006), and Doschek et al. (2008). De Pontieu et al. (2015) were able to explain the correlation between nonthermal line broadening and intensity of TR lines only when including NEQ ionization in their 2.5D numerical experiments. Martínez-Sykora et al. (2016) studied the statistical properties of the ionization of silicon and oxygen in different solar contexts: quiet Sun, coronal hole, plage, quiescent active region, and flaring active region, finding similarities with the observed intensity ratios only if NEQ effects are taken into account. Given their highly time-dependent nature and the relevance of the heating and cooling mechanisms in their evolution, surges are likely to be affected by NEQ ionization. Motivated by this fact, NS2017 included the NEQ ionization of silicon to compare synthetic Si IV spectra of two 2.5D numerical experiments with surge observations obtained by the *Interface Region Imaging Spectrograph* (*IRIS*; De Pontieu et al. 2014) and the Swedish 1-m Solar Telescope (SST; Scharmer et al. 2003). The results showed that the experiments were able to reproduce major features of the observed surge; nonetheless, the theoretical aspects to understand the enhanced Si IV emissivity within the numerical surge and its properties were not addressed in that publication.

The aim of the present paper is to provide theoretical explanations concerning the relevance of the NEQ ionization for surges and the corresponding impact on the emissivity of TR lines. We use 2.5D numerical experiments carried out with the Bifrost code (Gudiksen et al. 2011), including the module developed by Olluri et al. (2013a) that solves the time-dependent rate equations to calculate the ionization states of different elements, thus allowing for departures from SE. Here we apply this module to determine the ionization levels of silicon and oxygen. We conclude that consideration of NEQ is necessary to get the proper population levels of the ions and, consequently, the right emissivity to interpret observations. A statistical analysis of temperature is provided to constrain the plasma properties involved in the emissivity of relevant lines of Si IV and O IV within the surges. Through detailed Lagrange tracing, we are able to determine the origin of the emitting plasma and the role of the optically thin radiation and thermal conduction to explain the departure of SE of the relevant ions. Furthermore, we compute synthetic profiles to understand previous observational results and predict future ones, highlighting the surge regions that are more likely to be detected and addressing the importance of the angle of LOS.

The layout of the paper is as follows. Section 2 describes the physical and numerical models. Section 3 explains the general features of the time evolution of the experiments. In Section 4, we show the main results of the paper splitting the section in (a) the relevance of the NEQ ionization of Si IV, and also O IV, in surges (Section 4.1); (b) the consequences of the NEQ ionization for the surge plasma emitting in those TR lines, analyzing its properties and comparing them with a generic quiet TR (Section 4.2); and (c) the origin of the NEQ plasma, addressing the role of the entropy sources (Section 4.3). In Section 5, we have calculated absolute intensities and synthetic spectral profiles for diagnostic purposes and comparison with observations, emphasizing also the importance of the surge geometry and LOS. Finally, Section 6 contains a summary and conclusions.

2. The Physical and Numerical Model

We have run two 2.5D numerical flux emergence experiments in which surges are a natural consequence of magnetic reconnection processes. Those two experiments were also used by NS2017 and Rouppe van der Voort et al. (2017) to compare the synthetic profiles with the complex profiles observed with *IRIS* and SST.

This section is divided into two parts: (1) the numerical code, and (2) the description of the model underlying our experiments.

2.1. The Numerical Code

The two experiments have been carried out with the 3D radiation-MHD (R-MHD) Bifrost code (Gudiksen et al. 2011; Hayek et al. 2010; Carlsson & Leenaarts 2012), which treats the radiative transfer from the photosphere to the corona and thermal conduction in a self-consistent manner (see also NS2016 for further details of this code applied to surge experiments). Furthermore, we have enabled in the code a module developed by Olluri et al. (2013a) to follow the NEQ ionization states of elements with atomic number greater than 2. This module solves the rate equations for those elements using the temperature, mass density, electronic number density n_e, and velocity values of the simulation without modifying the results of the R-MHD calculation, so there is no feedback, e.g., on the energy equation terms such as the optically thin losses (see the discussion in Section 6.1). In particular, we have employed it to calculate the NEQ ionization fraction for silicon and oxygen, using abundances from Asplund et al. (2009), 7.52 and 8.69, respectively, in the customary astronomical scale, where 12 corresponds to hydrogen.

2.2. Description of the Models

2.2.1. Physical Domain and Initial Condition

In the two experiments, we began with a statistically stationary 2D snapshot that spans from the uppermost layers of the solar interior to the corona and whose physical domain is 0.0 Mm $\leqslant x \leqslant$ 32.0 Mm and -2.6 Mm $\leqslant z \leqslant$ 30.0 Mm, where

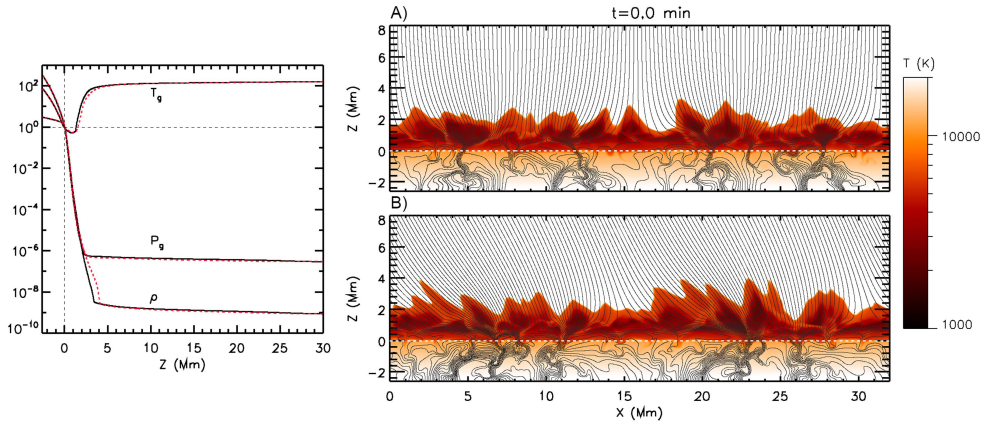

Figure 1. Left: horizontal averages for the initial stratification of ρ, P_g, and T normalized to their photospheric values at $z = 0$ Mm, namely, $\rho_{\rm ph} = 3.1 \times 10^{-7}$ g cm^{-3}, $P_{g_{\rm ph}} = 1.1 \times 10^5$ erg cm^{-3}, and $T_{\rm ph} = 5.7 \times 10^3$ K. The solid black line represents the stratification for the vertical coronal field experiment; the red dotted line, for the slanted one. The horizontal and vertical dotted lines mark the reference normalization values at $z = 0$ Mm. Right: 2D maps for the initial temperature, with magnetic field lines in black for the vertical experiment (top) and slanted experiment (bottom). The maps only show temperatures below 2×10^4 K (although the range varies from 1660 K up to ∼1 MK) and heights between -2.6 Mm $\leqslant z \leqslant$ 8.0 Mm (the top of the domain reaches $z = 30$ Mm). The solar surface is roughly at $z = 0$ Mm (white dashed horizontal line).

$z = 0$ Mm corresponds to the solar surface. The grid is uniform in the x-direction with $\Delta x = 31$ km, but it is nonuniform in the vertical direction in order to better resolve the photosphere and chromosphere: the vertical grid spacing is 20 km from the photosphere to the TR and increases gradually in the corona up to 147 km at the top of the domain.

The left panel of Figure 1 contains the horizontal averages for the initial density, ρ, gas pressure, P_g, and temperature, T, for both experiments normalized to photospheric values, namely, $\rho_{\rm ph} = 3.1 \times 10^{-7}$ g cm^{-3}, $P_{g_{\rm ph}} = 1.1 \times 10^5$ erg cm^{-3}, and $T_{\rm ph} = 5.7 \times 10^3$ K. The corona has a temperature around 1 MK and a magnetic field with a strength of 10 G, with the difference that one of the experiments (hereafter *the vertical experiment*) has a vertical magnetic field in the corona, while in the other (*the slanted experiment*) the magnetic field in the corona is inclined 30° with respect to the vertical direction (see magnetic field lines superimposed in black in the 2D temperature maps for the initial snapshot in Figure 1).

2.2.2. Chemical Elements Calculated in NEQ and Their Spectral Lines

We have used the NEQ module of Olluri et al. (2013a) mentioned in Section 1 to compute the NEQ ionization of silicon in both numerical experiments. Furthermore, in the vertical experiment we also calculate the NEQ ionization of oxygen, with the goal of predicting future observational results. Once the NEQ populations are obtained, we are able to compute the emissivity using

$$\epsilon_\lambda = \frac{h\,c}{4\,\pi\,\lambda}\, n_u\, A_{\rm ul}, \qquad (1)$$

where h is the Planck constant, c is the light speed, λ is the wavelength of the spectral line, n_u is the population density of the upper level of the transition (i.e., the number density of emitters), and $A_{\rm ul}$ is the Einstein coefficient for spontaneous de-excitation given by

$$A_{\rm ul} = \frac{8\,\pi^2\,e^2}{m_e\,c}\,\frac{1}{\lambda^2}\,\frac{g_l}{g_u}\,f_{lu}, \qquad (2)$$

where e is the electron charge, m_e the electron mass, g_l and g_u the statistical weights of the lower and upper states, respectively, and $f_{\rm lu}$ the oscillator strength. The units used in this paper for the emissivity ϵ are erg cm^{-3} sr^{-1} s^{-1}. For the sake of compactness, we will refer to it in the following as $\epsilon_{\rm CGS}$.

Since we are interested in understanding the response of the TR to chromospheric phenomena like surges, we have chosen the following *IRIS* lines: Si IV λ1402.77, which is the weakest of the two silicon resonance lines, and O IV λ1401.16, the strongest of the forbidden oxygen lines that *IRIS* is able to observe. The corresponding formation temperature peaks in SE, $T_{\rm SE}$, and other relevant parameters to calculate the Einstein coefficient (Equation (2)) and the corresponding emissivity (Equation (1)) of these lines are shown in Table 1. Under optically thin conditions, Si IV λ1393.76 is twice as strong as λ1402.77, so the results we obtain in this paper can also be applied to Si IV λ1393.76. Furthermore, the study of Si IV λ1402.77 can provide theoretical support to our previous paper NS2017. In turn, the choice of the λ1401.16 line for oxygen is because the O IV lines are faint and require longer exposure times to be observed (De Pontieu et al. 2014). Thus, in order to make any prediction that could be corroborated in future *IRIS* analysis, we focus on the strongest of the oxygen lines, which has a better chance of being detected. For simplicity, hereafter we refer to the Si IV λ1402.77 and O IV λ1401.16 emissivities as the Si IV and O IV emissivities, respectively.

Table 1
Relevant Parameters for the Studied Emission Lines

Line	T_{SE} (K)	g_u	g_l	f_{lu}	n_u/ϵ_λ
Si IV λ1402.77	$10^{4.9}$	2	2	2.7×10^{-1}	974
O IV λ1401.16	$10^{5.2}$	6	4	5.1×10^{-7}	7.62×10^{8}

Table 2
Parameters of the Initial Twisted Magnetic Tube for Both Experiments

x_0 (Mm)	z_0 (Mm)	R_0 (Mm)	q (Mm^{-1})	B_0 (kG)
15.0	−2.8	0.10	2.4	20

2.2.3. Boundary Conditions

We are imposing periodicity at the side boundaries; for the vertical direction, characteristic conditions are implemented at the top, whereas an open boundary is maintained at the bottom, keeping a fixed value of the entropy of the incoming plasma. Additionally, in order to produce flux emergence, we inject a twisted magnetic tube through the bottom boundary following the method described by Martínez-Sykora et al. (2008). The parameters of the tube (specifically, the initial location of the axis, x_0 and z_0; the field strength there, B_0; the tube radius R_0; and the amount of field line twist, q) are identical in both experiments and given in Table 2. The total axial magnetic flux is $\Phi_0 = 6.3 \times 10^{18}$ Mx, which is in the range of an ephemeral active region (Zwaan 1987). Details about this kind of setup are provided in NS2016.

3. General Features of the Time Evolution of the Experiments

The numerical experiments start with the injection of the twisted magnetic tube through the bottom boundary ($t = 0$ minutes). Within the convection zone, the tube rises with velocities of $\lesssim$2 km s^{-1} and suffers deformations due to the convection flows, mainly in the regions where the downflows are located. The twisted tube continues rising until it reaches the surface. There, the magnetized plasma accumulates until it develops a buoyancy instability ($t \approx 40$ minutes) in a similar way to that explained by NS2016.

The subsequent phases of evolution are characterized by the emergence and expansion of the magnetized plasma into the solar atmosphere, producing a dome-like structure of cool and dense matter ($t \sim 50$ minutes). During the expansion process, the dome interior becomes rarefied owing to gravitational flows. Simultaneously, the magnetic field of the emerged plasma collides with the preexisting coronal ambient field, and as a consequence, nonstationary magnetic reconnection occurs, forming and ejecting several plasmoids. Our vertical experiment has recently been used by Rouppe van der Voort et al. (2017) to show that the Si IV spectral synthesis of those plasmoids is able to reproduce the highly broadened line profiles, often with non-Gaussian and triangular shapes, seen in *IRIS* observations.

As an indirect consequence of the magnetic reconnection, a surge is obtained in both experiments. This is illustrated in Figure 2 through temperature maps with overlying magnetic field lines for each experiment: panel (a) shows the vertical experiment at $t = 65.0$ minutes, and panel (b) shows the slanted one at $t = 64.3$ minutes. Those are representative instants when the surge is clearly distinguishable as an elongated structure detached from the dome. For later reference, different regions have been marked in the figure that will be seen below to correspond to prominent features of the surge in terms of NEQ ionization and brightness in the spectra: the internal footpoint, which is located at the base of a wedge created by the detachment process that separates the surge from the dome (NS2016); the external footpoint, which is just the external boundary of the surge; and the flanks and top of the crests. Although not directly discussed in this paper, another region is probably worth mentioning, namely, the hot jet: in the vertical experiment, it is shown clearly through the red temperature contour of $T = 1.2 \times 10^6$ K; in the slanted one, the temperatures of the high-speed collimated ejection are not distinguishable from the rest of the corona. The difference between both experiments may be due to the fact that the slanted case has a denser emerged dome and, perhaps, the entropy sources in it are less efficient in heating the plasma that passes through the magnetic reconnection site.

4. The Role of the Nonequilibrium (NEQ) Ionization

The importance of the NEQ ionization is studied in this section from a triple perspective: (a) the comparison of the NEQ number densities with those calculated under the SE approximation (Section 4.1), (b) the consequences for the emissivity of the plasma (Section 4.2), and (c) the key mechanisms that cause the departure from SE in the surge plasma (Section 4.3).

4.1. The SE and NEQ Number Densities

The results of the current paper are obtained by solving the equation rates for the relevant ionization states of Si and O, i.e., taking into account NEQ effects using the Olluri et al. (2013a) module mentioned in earlier sections: the number densities of emitters n_u thus calculated will be indicated with the symbol n_{NEQ}. In order to test the accuracy of the SE approximation, we have also calculated the n_u that would be obtained imposing SE in the Olluri et al. (2013a) module: those will be indicated with the symbol n_{SE}. The accuracy or otherwise of the SE approximation is measured here through the following ratio:

$$r = \frac{n_{SE} - n_{NEQ}}{n_{SE} + n_{NEQ}}. \quad (3)$$

The parameter r varies between -1 and 1; its meaning is as follows:

(a) If $r \approxeq 0$, the number density of emitters obtained imposing SE would be approximately equal to the one allowing NEQ rates ($n_{SE} \approxeq n_{NEQ}$), so in those regions the SE approximation to calculate the state of ionization would be valid.
(b) If clearly $r < 0$, this means that $n_{SE} < n_{NEQ}$, so the approximation of SE ionization would underestimate the real population. As r becomes more negative, the NEQ effects would be more prominent and the SE approximation would become less accurate. In the extreme case ($r = -1$), the assumption of SE would mistakenly result in an absence of ions in the ionization state of interest!
(c) On the other hand, if $r > 0$, it follows that $n_{SE} > n_{NEQ}$, so the computation of the ionization in SE would be wrong again, but in this case because it would overestimate the real population. When $r = 1$, SE would give

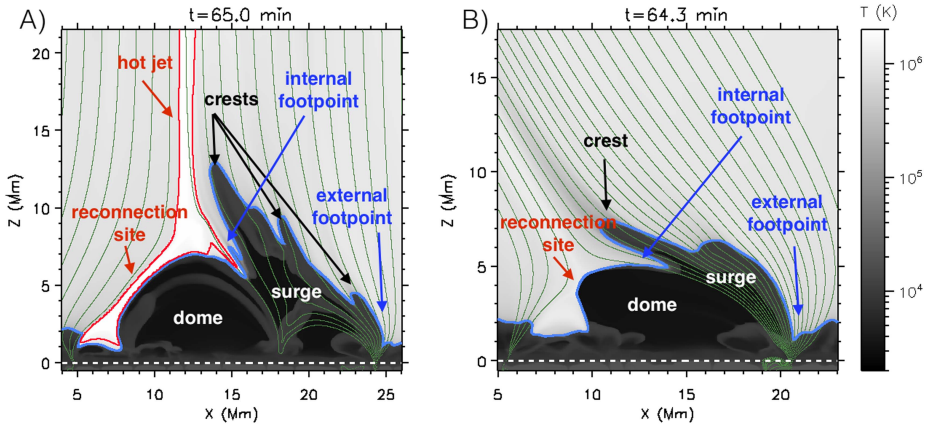

Figure 2. Image (taken from NS2017) showing 2D temperature maps for the context of the surge experiments and the regions of interest. (a) Vertical coronal magnetic field experiment at $t = 65.0$ minutes. (b) Slanted coronal magnetic case at $t = 64.3$ minutes. Additionally, magnetic field lines (green) and temperature contours for the $T_{SE} = 7.9 \times 10^4$ of Si IV K (blue) and for $T = 1.2 \times 10^6$ K (red) are added.

as a result a totally fictitious population, since the full NEQ calculation indicates that there are no ions!

The ratio r is plotted in Figure 3 for the two experiments described in this paper. The upper panels in each block contain 2D maps of r, namely, for panel (a) Si IV in the slanted experiment at $t = 64.3$ minutes, for panel (b) Si IV in the vertical experiment at $t = 65$ minutes, and for panel (c) O IV also in the vertical experiment at $t = 65$ minutes. To limit the diagram to the relevant regions, a gray mask is overplotted, and only those pixels with emissivity obtained from the NEQ computation above a threshold ($\epsilon_{CGS} \geqslant 10^{-10}$) are being shown. The bottom panel in each block contains a line plot for the median M of the absolute value of r in the regions not covered by the mask in each column. Using the absolute value of the ratio elucidates the areas where NEQ ionization is important, either because SE underestimates ($r < 0$) or overestimates ($r > 0$) the real number density of emitters n_u. In the figure, two regions can be clearly distinguished:

1. The quiet transition region (hereafter QTR). We define it as the TR that has not been perturbed by the flux emergence and subsequent surge and/or jet phenomena. The horizontal extent of the QTR is marked in the figure with dashed vertical lines and corresponds to the region located between $0.0 \leqslant x \leqslant 2.0$ Mm and 22.0 Mm $\leqslant x \leqslant 32.0$ Mm for the slanted experiment and between $0.0 \leqslant x \leqslant 3.0$ Mm and 26.5 Mm $\leqslant x \leqslant 32.0$ Mm for the vertical one. In this domain, r mostly shows negative values (blue color in the image) in a thin layer in the TR ($z \sim 2$ Mm). The corresponding M value is on average between 0.2 and 0.3 (horizontal dashed line in red in the panels), which indicates that both Si IV and O IV suffer significant departures from SE.

2. The second region corresponds to the main result of this section: the emerged domain, namely, the dome and surge, is severely affected by the NEQ ionization for both silicon and oxygen (see the dark blue color, which corresponds to $r \approx -1$, and corresponding M value close to 1). The value $r \approx -1$ is found in cold regions with $T \sim 2 \times 10^4$ K and also in hot domains ($T \sim 5 \times 10^5$ K). Also, on the left of the surge, we also find some regions where $r > 0$ (red), especially in the slanted experiment, which indicates that the SE approximation is overestimating the real population. Since our main goal is to study the surge, we focus on its surroundings and, in particular, on the domain marked in the figure with solid lines, i.e., 8.5 Mm $\leqslant x \leqslant$ 21.0 Mm for the slanted experiment and 11.0 Mm $\leqslant x \leqslant$ 25.5 Mm for the vertical one. In the following, we refer to this range as the enhanced transition region (ETR). In the associated 1D panels, we see that M shows larger values than in the QTR; in fact, the median reaches values close to one in many places of the ETR. There are some specific locations within the ETR where M shows substantially lower values, e.g., $x = 16.2$ Mm or $x = 18.1$ Mm in panels (b) and (c). Looking at the 2D panels, we realize that in those locations part of the TR has r close to zero (white patch above the blue line). Consequently, the median in that vertical column decreases. Note, however, that even in those locations the M values in the ETR are larger than, or at least comparable to, the largest ones found in the QTR. This finding highlights the relevance of including the NEQ calculation for eruptive phenomena like surges, since without it the calculated Si IV and O IV populations would be totally erroneous. This would translate into wrong emissivity values and therefore mistaken synthesis diagnostics.

4.2. Characterizing the Plasma in NEQ

Having studied the NEQ effects on the two different domains of our experiments (ETR, QTR), we now turn to the associated question of the emissivity, in particular, for the Si IV and O IV lines. To that end, we start by showing 2D maps of the emissivity in Figure 4 (upper panel in each block) for the same instants as in Figure 3. In this case, we have constrained the maps to values of $\epsilon_{CGS} > 10^{-8}$, just to focus on the layer with the largest emission, which is the natural candidate to be observed. Since the emitting layer is really thin, we are adding small 2D maps at the bottom of each block containing a

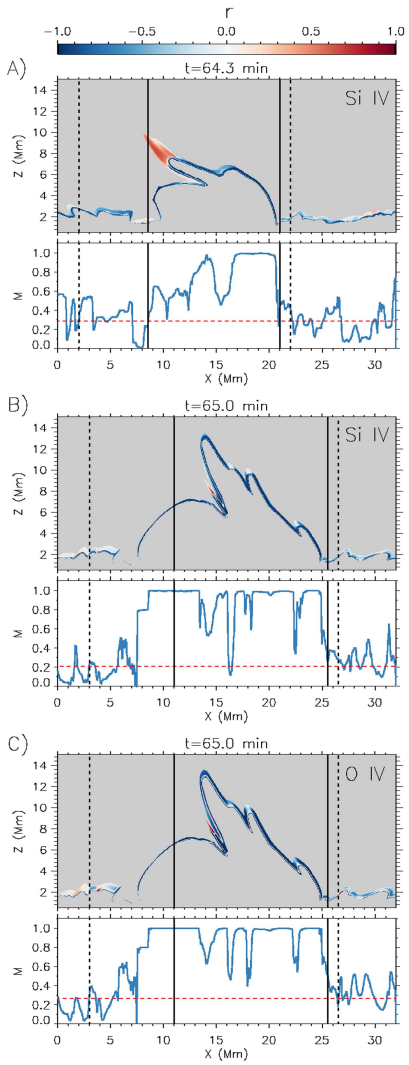

Figure 3. 2D maps of the ratio r from Equation (3) for the Si IV population for (a) the slanted experiment at $t = 64.3$ minutes and (b) the vertical one at $t = 65.0$ minutes. Panel (c) shows r for the O IV population in the vertical experiment at $t = 65.0$ minutes. A gray color mask is overplotted where the emissivity obtained from the NEQ computation is $\epsilon_{\rm CGS} < 10^{-10}$. Below each 2D map, the median M of $|r|$ in the high-emissivity region (i.e., outside of the mask) is shown. Solid and dashed vertical lines delimit the ETR and QTR regions, respectively. The horizontal line in the M panels marks the average value of M within the QTR.

blowup of the emissivity, ϵ, and, additionally, of the temperature, T; electronic number density, n_e; and the ratio between the Si IV and O IV emissivities, R_ϵ. More precisely, for each vertical column we define a height coordinate H centered at the position [called $z_{\rm max}(x)$ in the following] of the maximum emissivity in that column,

$$H = z - z_{\rm max}, \quad (4)$$

and use it, instead of z, in the maps. For clarity, in the top panel we have indicated the location of $z_{\rm max}$ at selected columns using symbols. Since emissivities can be converted into number densities of emitters n_u via simple multiplication with a constant factor (Equation (1) and Table 1), a color bar with n_u for both Si IV and O IV has been added in the figure.

By comparing the two emissivity panels in each block of Figure 4 (see also associated movie), we find that the region of high emissivity at the footpoints and crests of the surge covers a larger vertical range than in other regions. This is mainly caused by the varying mutual angle of the vertical with the local tangent to the TR, so, in some sense, it is an LOS effect; full details of different LOS effects are discussed in Section 5.2. Inspecting the lower panels of ϵ of each block, some locations (e.g., the internal footpoint, $x \approx 15$ Mm, in O IV at $t = 65.0$ minutes) are seen to have enhanced emissivity by a factor of two or three in comparison to the maximum values usually seen at positions of the QTR and ETR; nonetheless, this behavior is sporadic as seen in the accompanying movie.

We also notice that both Si IV and O IV show similar values of emissivity, in spite of the huge contrast in the corresponding number density of emitters (see second color scale at the upper right corner of the image). This is due to the difference in the oscillator strengths $f_{\rm lu}$, which for O IV is six orders of magnitude weaker than for Si IV (see Table 1). In panels (b4) and (c4), we have plotted the emissivity ratio of Si IV to O IV, R_ϵ, finding that the typical values in the locations with the highest emissivity within the ETR are around 2 (although it can reach up to factors around 5), while in the QTR the average R_ϵ is close to 1. On the other hand, in the locations with low emissivity and high temperature, especially in the QTR, we appreciate that R_ϵ is lower than unity, which is not surprising since O IV can be found at higher temperatures. Note that this is a ratio of emissivities and does not correspond to the intensity ratio commonly used for density diagnostics (e.g., Hayes & Shine 1987; Feldman et al. 2008; Polito et al. 2016).

We cannot find in the emissivity maps the same sort of drastic contrast between QTR and ETR that we found for the r parameter in the previous section; nonetheless, we do appreciate differences between both regions in terms of temperature and electronic number density: the range of T and n_e in the ETR is larger than in the QTR. This is especially evident in the hot and low-density part, where the T and n_e of the ETR reach values around 1 MK and 10^9 cm^{-3}, respectively (note that the n_e provided is obtained from local thermodynamic equilibrium [LTE] since the ionization of the main contributors for electrons, such as hydrogen and helium, is computed in LTE according to the equation-of-state table of Bifrost). In order to further explore those differences, we resort to a statistical study of the values of emissivity and temperature in the different regions (QTR, ETR) and for the two ions, which is presented in the following. The statistics is based on all plasma elements with $\epsilon_{\rm CGS} \geqslant 10^{-8}$ in the time span between surge formation ($t = 55.0$ minutes) and decay ($t = 70.7$ minutes). The resulting sample contains 4×10^6 elements. Figure 5 shows the corresponding joint probability density functions (JPDFs) for emissivity ϵ and temperature T

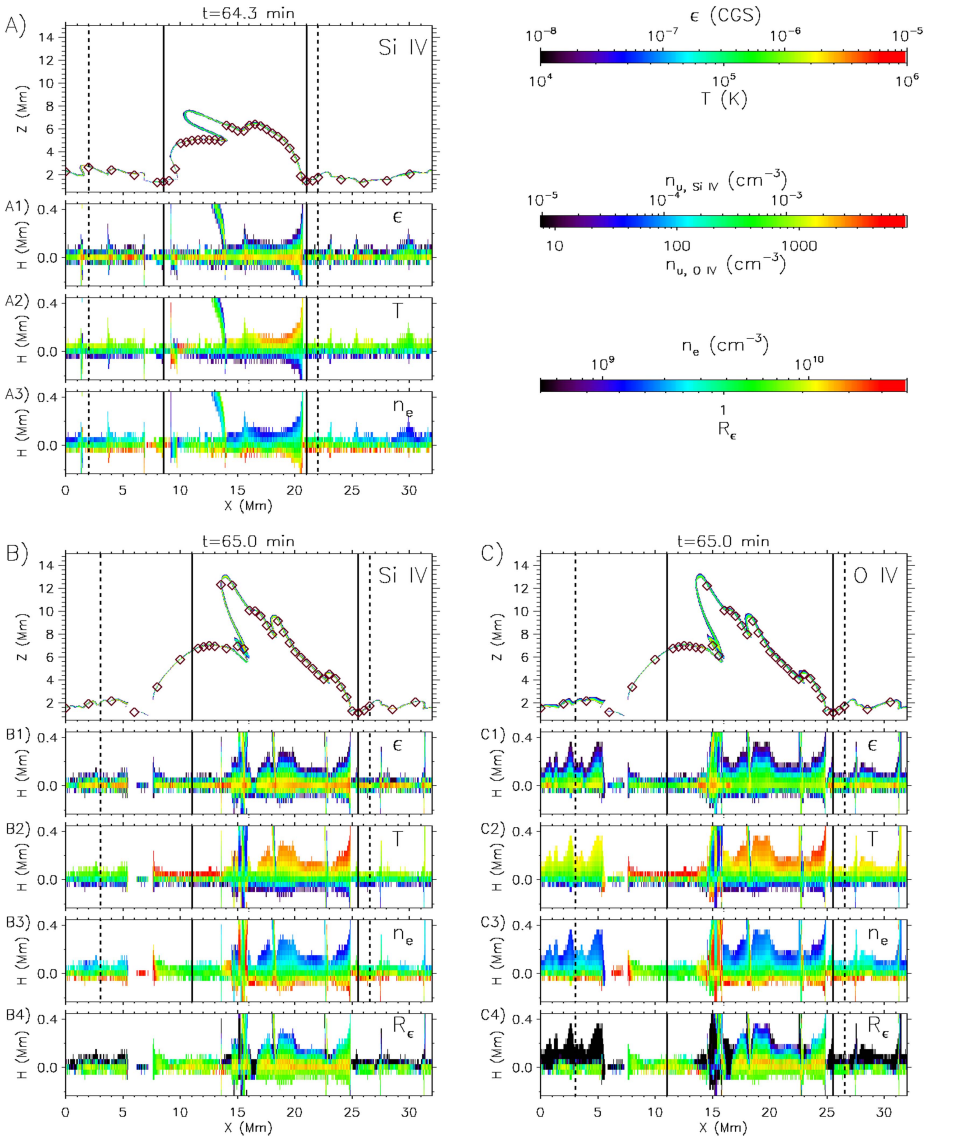

Figure 4. Maps of the 2D emissivity ϵ for (a) Si IV in the slanted experiment, (b) Si IV in the vertical one, and (c) O IV also for the vertical experiment. Diamonds have been superimposed on the region of high emissivity to mark the position of z_{max} (see Equation (4)). A color scale at the upper right of the figure contains the translation from emissivity to number densities of emitters n_u. In each of the blocks, secondary panels for ϵ, T, and n_e have been inserted that use H as the vertical scale. Additionally, a panel of the ratio of the Si IV and O IV emissivities, R_ϵ, is added for panels (b) and (c). All the maps only show places where $\epsilon_{CGS} \geqslant 10^{-8}$. The instants in the panels and the vertical lines are the same as in Figure 3. The accompanying animation shows the time evolution of the three experiments from the early stages of the surge until its decay phase.

(An animation of this figure is available.)

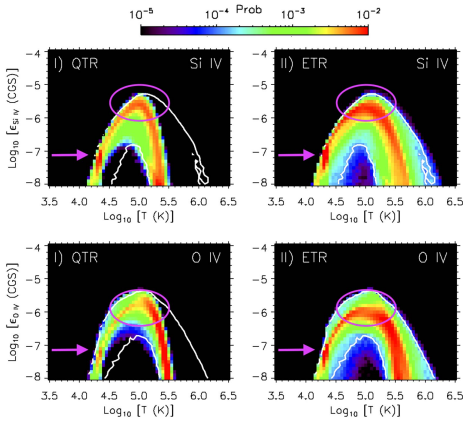

Figure 5. JPDFs of emissivity and temperature in the QTR and ETR in the vertical experiment for Si IV (top row) and O IV (bottom row) for the time range $t = 55.0$–70.7 minutes. The size of the sample is 4×10^6 elements. The white lines are isocontours of probability equal to 10^{-4} in the ETR distribution. The areas marked by ovals and arrows are discussed in the text.

for the vertical experiment. For Si IV we could also show results for the statistical distributions for the slanted experiment, but the resulting JPDFs are very similar to those presented here. This similarity suggests that, although the vertical and slanted experiments differ in terms of magnetic configuration, size of the emerged dome, and shape of the surge (compare the two panels of Figure 2), the results described below could be applicable to different surge scenarios. In the following, we explain the results first for Si IV (Section 4.2.1) and then for O IV (Section 4.2.2).

4.2.1. Plasma Emitting in Si IV

We start analyzing the QTR and ETR distributions for the Si IV emissivity (see top row of Figure 5). The main result is that in the region with the largest emissivity values the ETR is more densely populated than the QTR (see the region marked by a pink oval around $\epsilon_{CGS} \sim 10^{-5.6}$), i.e., the boundaries of the surges are more likely to show signal in Si IV observations than the QTR. This helps explain why, in the *IRIS* observations of our previous paper NS2017, we could detect the surge as an intrinsically brighter structure than the rest of the TR. Furthermore, both the QTR and ETR have the greatest values of emissivity in the temperature range between $10^{5.0}$ and $10^{5.1}$ K. This differs from what one would expect in SE, where the maximum emissivity is located at the peak formation temperature ($T_{SE} = 10^{4.9}$ K; see Table 1), again an indicator of the importance of taking into account NEQ effects. Additionally, the distribution for both QTR and ETR is more spread in temperature than what one would expect from a TR distribution computed in SE (see, e.g., Figure 15 of Olluri et al. 2015). The mass density found for both QTR and ETR around the maximum Si IV emissivity is $\rho \sim 6.3 \times 10^{-15}$ g cm^{-3}.

As part of the analysis, we have also found other features worth mentioning:

1. The ETR has a broader temperature distribution than the QTR. In order to illustrate this fact, all the panels of Figure 5 contain isolines in white for the probability 10^{-4} in the ETR. The comparison of those contours with the QTR distribution shows that the ETR has a wider distribution in temperature, especially above $10^{5.5}$ K. Although not shown in the figure, the mass density values for most of the emitting plasma (more precisely: the mass density values with probability above 10^{-4}) are constrained to similar ranges for both the QTR and ETR: approximately at $[2.0 \times 10^{-15}, 7.9 \times 10^{-14}]$ g cm^{-3} for the vertical experiment and at $[1.0 \times 10^{-15}, 6.0 \times 10^{-14}]$ g cm^{-3} for the slanted one.
2. A secondary probability maximum is located at $\epsilon_{CGS} \sim 10^{-7.2}$ and $T \sim 10^{4.3}$ K (see the arrows in the panels). This corresponds to the temperature of the second ionization of helium according to the LTE equation of state of Bifrost: the energy deposited in the plasma is used to ionize the element instead of heating the plasma. Including the NEQ ionization of helium should scatter the density probability in temperatures, as shown by Golding et al. (2016) in the TR of their numerical experiments (the equivalent to our QTR); nevertheless, the NEQ computation of helium and a detailed discussion of their effects are beyond the scope of this paper.

4.2.2. Plasma Emitting in O IV

Focusing now on the statistical properties of the O IV emission (see bottom row of Figure 5), we see that, as for Si IV, the probability distributions for both QTR and ETR differ from what we could expect for an SE distribution, since they are centered at temperatures between $10^{4.9}$ and $10^{5.0}$ K instead of $T_{SE} = 10^{5.2}$ K (see Table 1). Furthermore, the ETR and QTR distributions are also broader in temperature than what one would expect from SE. Further noteworthy features of the plasma emitting in O IV are as follows:

1. The QTR exhibits larger probability than the ETR ($>10^{-3}$) in the maximum values of the emissivities ($\epsilon_{CGS} = 10^{-5.8}$); nevertheless, this fact changes around $\epsilon_{CGS} = 10^{-6.0}$, where the ETR shows larger emissivity (compare the region within the colored oval). Due to this complex behavior, we need to integrate the emissivity to know whether the ETR can be detected as a brighter structure compared to the QTR. In Section 5 we discuss this fact while analyzing the obtained synthetic profiles.
2. The ETR shows emissivity in O IV in a larger range of temperatures than the QTR, which is akin to the result for Si IV described in Section 4.2.1. This difference in the ranges is apparent mainly in hot coronal temperatures comparing the probability contours of the ETR (in white) with the QTR distribution.
3. We find the same secondary probability maximum as in the Si IV panels at the temperature of the second ionization of helium (see the pinks arrows).
4. Comparing the O IV panels with the Si IV ones, we see that the O IV distribution is more populated in hot temperatures and, correspondingly, lower densities. This is something we could expect since the ionization of this particular oxygen ion occurs at higher temperatures than Si IV.

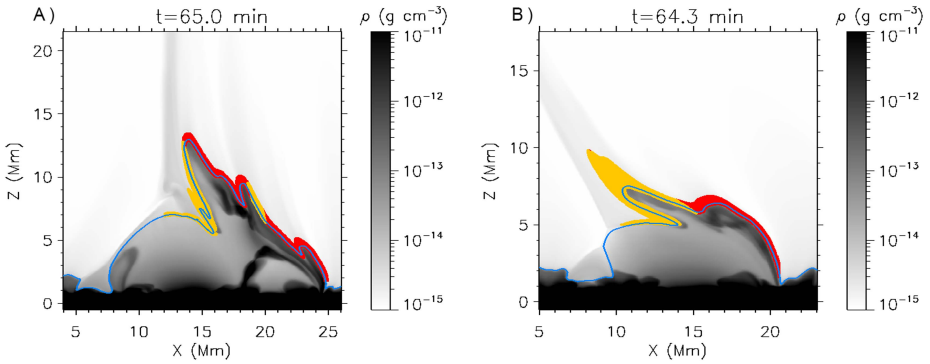

Figure 6. Density map showing the basic distribution of the (approximately) 6000 Lagrange tracers used in the text, distributed into two parts drawn with yellow and red dots corresponding to the two populations discussed in Section 4.3. The accompanying animation shows the evolution of the Lagrange tracers in the two experiments from early stages of the surge formation ($t \approx 55.0$ minutes) until its decay phase ($t \approx 70.0$ minutes).

(An animation of this figure is available.)

4.3. Lagrange Tracing: How the Entropy Sources Affect the NEQ Ionization

We focus now on the role of the entropy sources in the emissivity and NEQ ionization. To that end, we follow in time ≈6000 plasma elements of the ETR through Lagrange tracing. In the following, we explain the setup for the Lagrange elements (Section 4.3.1) and the results obtained from their tracing (Section 4.3.2).

4.3.1. The Choice of the Lagrange Elements

The Lagrange elements are selected at a given instant, corresponding to an intermediate evolutionary stage when the surge is clearly distinguishable as a separate structure from the dome. The selected instants are $t = 64.3$ minutes for the slanted experiment and $t = 65.0$ minutes for the vertical experiment, which are the same times used for Figures 2, 3, and 4. In order to focus on the domain in and near the surge, we limit the selection to the rectangular areas: $12.0 \leqslant x \leqslant 25.2$, $2.2 \leqslant z \leqslant 15.0$ (vertical experiment); and $7.0 \leqslant x \leqslant 19.0$, $5.0 \leqslant z \leqslant 15.0$ and $19.0 \leqslant x \leqslant 20.5$, $1.5 \leqslant z \leqslant 15.0$ (slanted experiment). On those rectangles we lay a grid with uniform spacing $\Delta x = \Delta z = 40$ km: the Lagrange elements are chosen among the pixels in that grid. A further criterion is then introduced: we are interested in studying the origin and evolution of the plasma elements with strong emission in Si IV and O IV. Thus, a lower bound in the Si IV and O IV emissivity is established, namely, $\epsilon_{CGS} > 10^{-10}$, discarding all the pixels with emissivities below that value at the instants mentioned in the previous bullet point. The resulting choice of Lagrange tracers is shown in Figure 6 as red and yellow dots (the colors serve to distinguish the populations described below). Once the distribution is set, we then follow the tracers backward in time for 10 minutes, to study their origin, and forward in time for 5.7 minutes, to see the whole surge evolution until the decay phase, with a high temporal cadence of 0.2 s (see the accompanying animation to Figure 6).

4.3.2. Plasma Populations and Role of the Entropy Sources

Studying the time evolution of the Lagrange tracers, in particular their thermal properties, one can distinguish two populations that are the source of the Si IV and O IV emission: one originating in the emerged dome (yellow plasma population in Figure 6), and the other one originating in the corona (red population). By carefully inspecting the tracers of each population, we find that their behavior is well defined: the major difference between the elements within the same population is not the nature or order of the physical events described below, but rather the starting time of the evolution for each tracer. Figure 7 contains the time evolution of different quantities as measured following a representative Lagrange element of each population, namely, temperature, T (green); Si IV emissivity, $\epsilon_{\rm Si\,IV}$ (dark blue); O IV emissivity, $\epsilon_{\rm O\,IV}$ (light blue); characteristic time of the optically thin losses, $\tau_{\rm thin}$ (black); and characteristic time for the thermal conduction, $\tau_{\rm Spitz}$ (red).

The first population (top panel of Figure 7, corresponding to the elements marked in yellow in Figure 6) starts as cool and dense plasma coming from the emerged dome with extremely low emissivity (see the curves for the temperature in green, and for the emissivities in dark and light blue). At some point that plasma approaches the reconnection site and passes through the current sheet, thereby suffering strong Joule and viscous heating and quickly reaching TR temperatures. The sharp spike in the Si IV and O IV emissivity (blue curves) around $t \sim 62.5$ minutes corresponds to this phase: the temperature increase leads to the appearance of those ionic species, but, as the plasma continues being heated, it reaches high temperatures (maximum around 10^6 K) and the number densities n_u of Si IV and O IV decrease again. At those high temperatures the entropy sinks become efficient, with short characteristic times: see the red ($\tau_{\rm Spitz}$) and black ($\tau_{\rm thin}$) curves. The plasma thus enters a phase of gradual cooling, going again through TR temperatures, renewed formation of the Si IV and O IV ions, and increase in the corresponding emissivity (broad maximum in the blue curves in the right half of the panel). The plasma elements, finally, cool

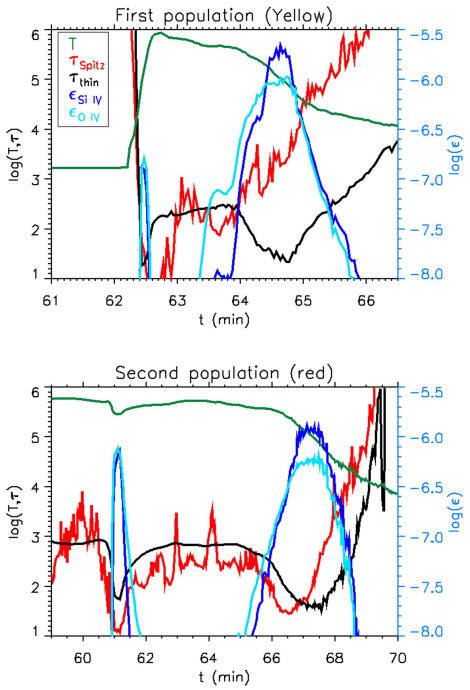

Figure 7. Time evolution of key physical quantities for representative Lagrange tracers in the vertical experiment of Figure 5. Top: Lagrange element coming from the emerged dome (yellow population in Figure 6). Bottom: Lagrange originating in the corona (red population in Figure 6). The curves show (left ordinate axis) the logarithm of temperature T (green), of the characteristic time of the optically thin losses τ_{thin} (black), and of the characteristic time for the thermal conduction τ_{Spitz} (red) and (right ordinate axis) the logarithm of the Si IV emissivity (dark blue) and of the O IV emissivity (light blue). All quantities are in CGS units.

down to chromospheric temperatures, with the emissivity decreasing again to very low values.

The defining feature of *the second population* (bottom panel of Figure 7, red dots in Figure 6) is that it originates in the corona as apparent in the temperature curve (green). This population starts at heights far above the reconnection site, with standard coronal temperature and density. During the magnetic reconnection process, its associated field line changes connectivity, becoming attached to the cool emerged region. Consequently, a steep temperature gradient arises along the field line, so the thermal conduction starts to cool down the plasma; given the temperature range, also the optically thin losses contribute to the cooling, although to a lesser extent (see the τ_{Spitz} and τ_{thin} curves around $t \sim 61$ minutes, in red and black, respectively). The temperature drops to values around $T \sim 10^{5.5}$ K, which, according to the JPDFs of Figure 5, makes it sufficiently likely that the Si IV and O IV emissivities from the Lagrange element are high. This explains the large increase, by a few orders of magnitude, in the blue emissivity curves around $t \sim 61$ minutes (although a small factor of $\sim$4 is due to the simultaneous increase in the mass density, which is reflected in a linear fashion in the emissivity). This cooling to TR temperatures, however, is short-lived: as the plasma element itself passes near the current sheet, it can be heated because of the Joule and viscous terms, and the temperature climbs again to values where the emissivities are low—hence the sharp spike in the blue curves between $t \sim 61$ and 61.5 minutes. There ensues a phase of gradual cooling from $t \sim 64$ minutes onward, similar to what happened to the previous population, with characteristic cooling times of a few to several hundred seconds (see red and black curves), passage through TR temperatures, broad maximum in the emissivity curves, and the plasma finally reaching chromospheric temperatures.

In our previous paper (NS2016) we found that surges were constituted by four different populations according to their thermal evolution. In the current paper, we see that only two of them, labeled Populations B and D in NS2016, are behind the enhanced emissivity of TR lines like those from silicon and oxygen discussed here. The other two populations described by NS2016 (A and C) keep cool chromospheric temperatures during their evolution and do not play any role for the TR elements.

Using the Lagrange tracing method developed here, we can produce conclusive evidence of enhanced Si IV and O IV emissivity and occurrence of fast evolution due to short timescales in the entropy sources associated with heat conduction or optically thin radiative cooling. Figure 8 contains double PDFs for ϵ_{CGS} versus τ_{thin} (left panels) and τ_{Spitz} (right panels) using as a statistical sample the values of those quantities for all Lagrange tracers along their evolution. The choice of the ionic species (Si IV, O IV) and experiment (slanted, vertical) in the panels is as in Figures 3 and 4. The figure clearly shows that when the entropy sources act on short timescales, the (Si IV, O IV) emissivities are large. In fact, the maximum values of ϵ_{CGS} correspond to characteristic cooling times between 20 and 100 s for τ_{thin} and between 4 and 40 s for τ_{Spitz}. Those changes are fast enough for the ionization levels of those elements to be far from SE.

5. Observational Consequences

In NS2017, different observed Si IV signatures within the surge were analyzed. Moreover, counterparts to the observational features were identified in the synthetic spectral profiles obtained from the numerical model; however, a theoretical analysis to understand the origin of the spectral features and the reason for the brightness in the various regions of the surge was not addressed. In the following subsection a theoretical study is carried out trying to quantify the impact of the NEQ ionization of silicon and oxygen on the spectral and total intensities and the observational consequences thereof (Section 5.1). Then, given the involved geometry of the surge, the particular LOS for the (real or synthetic) observation turns out to be crucial for the resulting total intensity and spectra. This is studied in Section 5.2.

5.1. Synthetic Profiles

Figure 9 contains the synthetic profiles obtained by integrating the emissivity along the LOS for different wavelengths in the Si IV λ1402.77 and O IV λ1401.16 spectral region and for the vertical experiment. The three rows of the figure correspond to different inclination angles θ for the LOS:

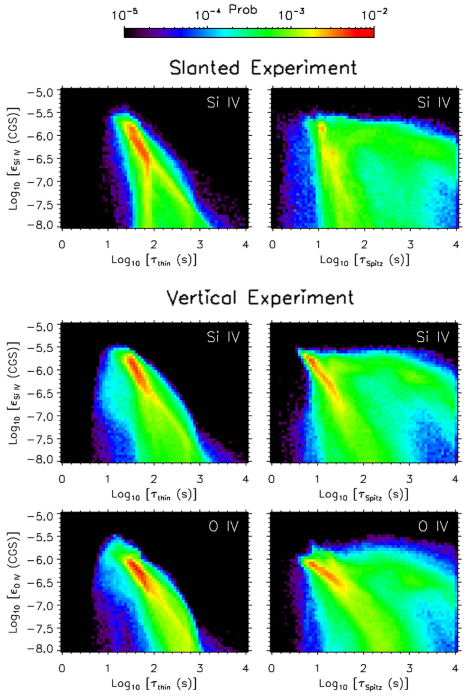

Figure 8. JPDFs for the Si IV and O IV emissivity of the Lagrange tracers over 15.7 minutes vs. the characteristic time of the optically thin losses ($\tau_{\rm thin}$; left column) and the thermal conduction ($\tau_{\rm Spitz}$; right column).

from top to bottom, 0°, −15°, and 15°, respectively. The panels in each row contain (a) the context of the experiment through a 2D map of the O IV emissivity; (b) the synthetic spectral intensity for Si IV, with the spectral dimension in ordinates and in the form of Doppler shifts from the central wavelength; and (c) the corresponding synthetic spectral intensity for O IV. Those spectra are obtained taking into account the Doppler shift due to the plasma velocity and applying a spatial and spectral PSF (Gaussian) degradation as explained in detail by Martínez-Sykora et al. (2016, their Section 3.1) and by NS2017 (their Section 2.2). In this way, we will be able to directly compare the results with *IRIS* observations. In order to ease the identification of the LOS in each panel, we have added to the labels on it the symbols 0, −, and +, respectively, for $\theta = 0°$, − 15°, and 15°. In the middle and bottom rows of the image, x_P and z_P are, respectively, the horizontal and vertical coordinates of the rotated figures.

To extend the analysis, it is also of interest to consider the total emitted intensity for each vertical column, i.e.,

$$I_\epsilon(x) = \int_{z_0}^{z_f} \epsilon \, dz, \qquad (5)$$

which, following Equation (1), is equal to the column density of the emitting species along the LOS (except for a constant factor). Equation (5) has been calculated separately for Si IV and O IV and with the emissivities obtained assuming either NEQ or SE ionization, to better gauge the importance of disregarding the NEQ effects. The results are shown in the middle and bottom panels of Figure 10 for Si IV and O IV, respectively. The top panel of the image contains the 2D map of the emissivity for Si IV for context identification. Combining Figures 9 and 10, we are able to discern and describe characteristic features of the spectral profiles:

1. The most prominent feature in the synthetic profiles of Figure 9 is the brightening associated with the location of the internal footpoint of the surge. In the corresponding movie, we can see how that footpoint is formed at around $t = 64$ minutes, as the surge detaches from the emerged dome. During those instants, the associated synthetic profiles are characterized by large intermittent intensities and bidirectional behavior with velocities of tens of kilometers per second, as apparent, e.g., in the (b0) and (c0) panels at $x \in [15, 16]$ Mm. In Si IV and O IV (panels (b) and (c)), we find that the internal footpoint is usually the brightest region, although there are some instants in which the brightest points can be located in the crests or the external footpoint. This is a potentially important result from the observational point of view because it can help us to unravel the spatial geometry of the surge in future observational studies: if strong brightenings are detected in Si IV and also in O IV within the surge, it would be reasonable to think that they correspond to the internal footpoint of the surge. In this region, the intensity ratio between Si IV and O IV ranges between 2 and 7, approximately. Note that, in general, the intensity ratio values vary depending on the observed region and features (Martínez-Sykora et al. 2016).

   In Section 5.2 we will see that LOS effects play a major role in causing the large brightness of the internal footpoint (and other bright features) compared to the rest of the surge. Here we consider the parallel question of the role of NEQ: what would be obtained for the intensity of the internal footpoint if SE were assumed? Comparing the values for Si IV in Figure 10 (middle panel, $13.8 \leqslant x \leqslant 16.1$), there is roughly a factor of two, on average, between the NEQ and SE intensities; for O IV (bottom panel), there is no major difference in the intensity between both calculations. One could conclude that while NEQ is important for the Si IV diagnostics, SE could be applied for the O IV case; nonetheless, even in the latter case, although the NEQ and SE intensities are similar, one would make a mistake in the determination of derived quantities like the number densities of emitters (Section 4.1) and temperatures (Section 4.2).

   Further distinctive brightenings in the spectral profiles appear at the site of the crests and of the external footpoint of the surge. The brightness of those regions is clear in the Si IV profiles (panels (b0), (b−), and (b+) of Figure 9) through their large intensity and is sometimes comparable to or greater than that of the internal footpoint (see, e.g., the locations at $x \sim 13$, 18, 23, and 25 Mm in the top row, or $x \sim 14$, 19, and 25 Mm in the bottom row). In the O IV profiles (panels (c0), (c−), and (c+), although faint in comparison with Si IV (around a factor of five less intense), most of those features are still

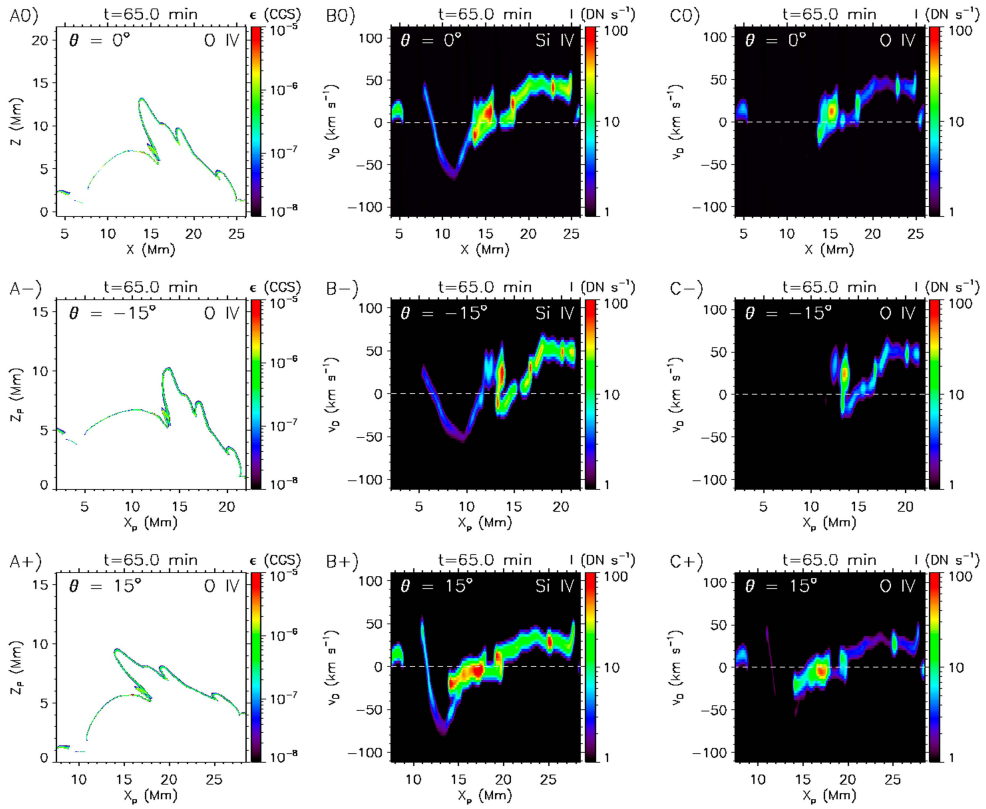

Figure 9. Synthetic profiles for the vertical experiment at different times for various LOS (θ). (a) 2D map of the ϵ_{CGS} for O IV to show the context; (b) synthetic spectral intensity for Si IV; (c) synthetic spectral intensity for O IV. To identify the LOS of each panel, we have added the symbols 0, −, and +, respectively, for $\theta = 0°$, $-15°$, and $15°$. In the $\theta \neq 0$ rows, z_P and x_P are, respectively, the vertical and horizontal coordinates of the rotated figures. The animation of this figure shows the time evolution of the surge from its origin ($t = 61$ minutes) up to its decay phase ($t = 70.7$ minutes) in the vertical experiment for the three LOSs.
(An animation of this figure is available.)

slightly brighter than the rest of the surge. This difference in intensities between Si IV and O IV can also be used to understand the observations: if strong signals are observed in Si IV associated with some moderate signal in O IV, it could indicate that we are detecting the crests or the external footpoint. Concerning the NEQ/SE comparison of the intensity (Figure 10), the crests and footpoints show the same behavior as the internal footpoint.

2. The intensity of the rest of the surge is small in comparison with that of the footpoints and crests just described, so we wonder whether one could see it as a bright structure in actual observations and distinguish it from the rest of the TR. In the middle panel of Figure 10, comparing the I_ϵ values for Si IV within the ETR against those in the QTR, we can see that all the regions in the surge have a higher intensity than the QTR; outside of the brightest features, the excess emission of Si IV in the surge may be just a factor of two or three above the QTR, but that can provide enough contrast to tell the two regions apart observationally, as found in NS2017. Note, importantly, that there is a large difference between the NEQ and SE results for Si IV in the surge, up to a factor of 10, so the SE assumption would seriously underestimate the intensity. In fact, in most of the places Si IV would be similar to or fainter than O IV if SE were valid as shown also, e.g., by Dudík et al. (2014) and Dzifčáková et al. (2017). On the other hand, for O IV (bottom panel), the prominent features are the footpoints and crests of the surge, while the other parts have I_ϵ comparable to the QTR. As a consequence and from an observational point of view, while in Si IV we could find enhanced emission in the whole surge (which is compatible with the NS2017 observation), for O IV only

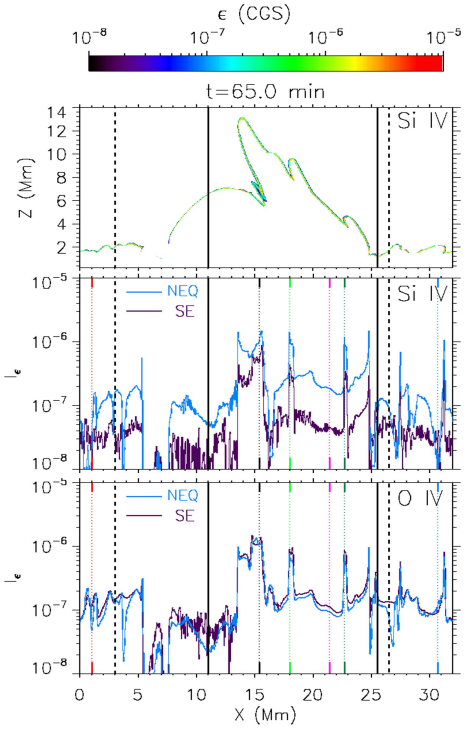

Figure 10. Top panel: 2D map of the Si IV emissivity. The vertically integrated intensity I_ϵ is shown for both Si IV (middle panel) and O IV (bottom panel) assuming NEQ ionization (light-blue line) and SE (purple line). Solid and dashed lines are overplotted in the image to delimit the ETR and QTR regions as in previous figures. Dotted vertical lines are superimposed in the middle and bottom panels correspondingly to the cuts shown in Figure 11.

the brightest regions would stand out, namely, the internal footpoints and, to a lesser extent, the crests and external footpoints.

The underlying reason for the enhanced brightness of all those features, mainly the footpoints and crests of the surges, is not just the presence of additional numbers of ions due to NEQ effects: the complex geometry of the surge TR has important consequences when integrating the emissivity along the LOS to obtain intensities. This is discussed in the next section.

5.2. The Role of the LOS

The observation of TR lines generated in the surge strongly depends on the particular LOS. We show this here through two different effects:

(a) The alignment of the LOS with respect to the orientation of the surge's TR. We can appreciate this effect, e.g., in panel (a0) of Figure 9. There, considering, e.g., the crests situated at $x = 13.5$, 18, or 23 Mm, we see that a vertical LOS grazing the left side of the crest will include contributions from a much larger length of the TR than if the crossing were perpendicular or nearly so. The same can be said of the external footpoint at $x = 24.8$ Mm and also of the internal footpoint around $x = 16$ Mm. This effect clearly enhances the brightenings seen in those values of x in panels (b0) and (c0). Further evidence can be found by checking the I_ϵ curves in the middle and bottom panels of Figure 10; in fact, since the effect is purely geometrical, the contribution to brightness can be seen in both the NEQ and SE curves in the two panels of the figure. Varying the angle of the LOS, we can reach enhancement factors between 2 and 4; nonetheless, discerning which part of that factor is exclusively due to the LOS is complicated, since variations in the angle of integration imply integrations along slightly different emitting layers. Additionally, the inclination of the LOS with respect to the surge's TR may be important for the apparent horizontal size of the brightenings. This can be seen through comparison of the three rows of Figure 9: considering the size of the brightening associated with the internal footpoint, we see that it covers a larger horizontal range in the $\theta = 0°$ and $\theta = 15°$ cases (top and bottom rows) than in the $\theta = -15°$ case (middle row), since the good alignment of the latter is lost in the former.

(b) The multiple crossings of the TR by individual LOSs. Given that the TR of the surge is folded, there are horizontal ranges in which the LOS crosses it more than once (typically three times, in some limited ranges even five times). Given the optically thin approximation, the emitted intensity in those LOSs may be a few, or several, times larger than the value in a single crossing.

To further illustrate those two effects, we use Figure 11. The top panel contains a 2D map of the Si IV emissivity in which vertical cuts in different regions of interest are overplotted through colored and labeled lines. The corresponding Si IV emissivity distribution along those cuts is shown in panel (b). Additionally, a similar plot but for the O IV distribution is shown in panel (c). Those vertical cuts are also shown in panels (b) and (c) of Figure 10 for comparison purposes. The light- and dark-green cuts (numbers 3 and 5) are typical examples of the effect of the tangency between the LOS and the surge's TR at the crests: note the enhanced width of the maximum on the right in those two cuts due to tangency effects. Those cuts and the one in black (number 2) further show the effect of multiple crossings of the TR by the LOS. In particular, the LOS drawn in black crosses the folded TR near the internal footpoint four times (5.5 Mm $< z <$ 8 Mm), and an additional time at the top of the surge ($z \sim 11$ Mm). For the sake of completeness, we have added a dashed line for the crests (3 and 5) in the middle and bottom panels showing the emissivity if SE had been assumed: the thickness of the high-emissivity TR would be much smaller. Finally, in contrast to all the foregoing cases, the rest of the surge (pink line, label 4) and the QTR (red and blue lines, labels 1 and 6, respectively) show a simpler geometry: there is no TR-LOS alignment, and there is just a single crossing.

6. Discussion

In this paper, we have carried out two 2.5D radiative-MHD numerical experiments of magnetic flux emergence through

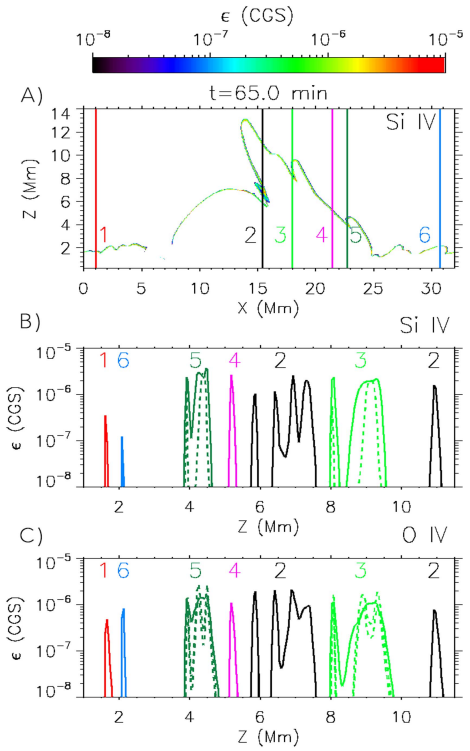

Figure 11. Illustration of the multiple crossings of the TR by a single LOS. (a) 2D map of the Si IV emissivity, with colored and labeled lines overplotted in regions of interest. The lines corresponds to different vertical cuts used in panels (b) and (c). (b) Si IV emissivity vs. the height Z for the different vertical cuts shown in the 2D map. (c) Same as panel (B), but for the O IV emissivity. Additionally, for the cuts labeled 3 and 5 we have added as a dashed line the corresponding emissivity if SE had been assumed.

granular convection and into the solar atmosphere. The experiments were performed with Bifrost, including an extra module of the code that computes the NEQ ionization of silicon and oxygen. The time evolution of the two experiments leads to the formation of a cool and dense surge. We have studied the relevance of the NEQ ionization for the presence of Si IV and O IV in the periphery of the surge and how it affects the corresponding emissivities. The properties of the surge plasma emitting in Si IV and O IV were then characterized and compared with those of the general TR plasma outside of the surge. We have also analyzed the role of the heat conduction and optically thin radiative cooling in the NEQ ionization. Furthermore, through forward modeling, we have understood different features of the synthetic spectral profiles of Si IV and O IV, explaining the importance of the shape of the TR surrounding the surge combined with the different possible angles of the LOS and providing predictions for future observational studies.

In the following, we first address the implications of the importance of the NEQ ionization in numerical experiments of eruptive phenomena in which heating and cooling are key mechanisms (Section 6.1). We then discuss their relevance for present and future observations (Section 6.2).

6.1. On the Importance of the Nonequilibrium (NEQ) Ionization

The main result of this paper is that the envelope of the emerged domain, more specifically, of the dome and surge, is strongly affected by NEQ ionization (Section 4.1). Focusing on the boundaries of the surge, comparing the number densities of emitters computed via detailed solution of the NEQ rate equations with those obtained assuming SE, we have concluded that the SE assumption would produce an erroneous result in the population of Si IV and O IV, mainly because it leads to a gross underestimate of the number density of emitters. The TR outside of the flux emergence site is also affected by NEQ, but to a smaller extent.

The above result has consequences in the corresponding emissivity (Section 4.2) and therefore in the interpretation of the observations. By means of statistical analysis, we have shown that the boundaries of the surge have greater values of the Si IV emissivity than the region outside of the flux emergence site. Correspondingly, we have given the name enhanced TR (ETR) to the former and quiet TR (QTR) to the latter (Section 4.2.1). This difference is part of the explanation of why the surge is a brighter structure than the rest of the TR in the *IRIS* observations by NS2017. Furthermore, the joint probability distributions for emissivity and temperature are not centered at the peak formation temperature of Si IV or O IV in SE (see $T_{\rm SE}$ in Table 1 and Section 4.2.2). This reinforces earlier results (e.g., Olluri et al. 2015) about the inaccuracies inherent in the process of deducing temperature values from observations in TR lines using SE considerations.

In Section 4.3 we have found that there are two different populations concerning the thermal evolution that leads to the Si IV and O IV emissivity. They have very different origins (one in the emerged plasma dome, the other in coronal heights), but both are characterized by the fact that they go through a period of rapid thermal change caused by the optically thin losses and thermal conduction: the maximum values of the Si IV and O IV emissivity in them are related to short characteristic cooling times: 20–100 s for $\tau_{\rm thin}$ and around 4–40 s for $\tau_{\rm Spitz}$. Those characteristic times are compatible with the theoretical results by Smith & Hughes (2010), who found that for typical densities of the active corona and the TR the solar plasma can be affected by NEQ effects if changes occur on timescales shorter than about 10–100 s. Those results highlight the role of optically thin losses and thermal conduction because (a) they provide the physical mechanism to diminish the entropy and, consequently, obtain plasma with the adequate temperatures to form ions of Si IV or O IV ($\sim 10^5$ K); and (b) they are fast enough to produce important departures from SE. On the other hand, the ion populations calculated through the present NEQ module in Bifrost are not used in the energy equation of the general R-MHD calculation (see Section 2.1), so this could underestimate the effects of the entropy sinks in the experiments. In fact, Hansteen (1993) found deviations of more than a factor of two in the optically thin losses when considering NEQ effects in his loop model, so $\tau_{\rm thin}$ could be even more efficient.

Our results indicate that surges, although traditionally described as chromospheric phenomena, show important emission in TR lines due to the NEQ ionization linked to the quick action of the cooling processes, so the response of the TR is intimately tied to the surge dynamics and energetics. In fact, the same statement may apply for other eruptive phenomena, in which impulsive plasma heating and cooling occurs (see Dudík et al. 2017, for a review of NEQ processes in the solar atmosphere).

6.2. Understanding Observations and Predictions for the Future

From the number density of emitters and emissivity results of Section 4 we gather that calculating heavy-element populations directly through the rate equations instead of via the assumption of SE can be important to understand the observations of surges (and of other fast phenomena that reach TR temperatures in their periphery like spicules (De Pontieu et al. 2017) or UV bursts (Hansteen et al. 2017). In that section, analyzing the Si IV and O IV emissivities of the plasma elements, we find that the ratio between them is approximately 2 in the regions with the highest emission within the ETR. Even though the intensity ratio is more commonly used (Hayes & Shine 1987; Feldman et al. 2008; Polito et al. 2016, among others), the emissivity ratio can also be a valuable tool to understand the behavior of the ions in different regions of the Sun. In particular, we see that in the ETR this ratio is larger than in the TR that has not been perturbed by the flux emergence and subsequent surge and/or jet phenomena (QTR).

To provide theoretical support to the NS2017 observations and predictions for future ones, in Section 5 we have therefore computed the synthetic profiles of Si IV λ1402.77 and O IV λ1401.16, taking into account the Doppler shift because of the plasma velocity and degrading the spatial and spectral resolutions to the *IRIS* ones. An LOS integration of the emissivities has also been carried out, to provide a measure for the total intensity emitted by the different regions of the surge. The strongest brightenings in Si IV and O IV have been located at the site of the internal footpoint, followed by the crests and the external footpoint (Figure 9, Section 5.1). The intensity ratio between Si IV and O IV in those regions is approximately 5 (although it can range from 2 to 7). Those values are between those for a coronal hole and a quiescent active region obtained by Martínez-Sykora et al. (2016), which is consistent since we are mimicking an initial stratification similar to a coronal hole in which a total axial magnetic flux in the range of an ephemeral active region (Zwaan 1987) has been injected. The comparison of the total intensity for the NEQ and SE cases (Figure 10, Section 5.1) leads to a further indication of the importance of using NEQ equations to determine the number density of Si IV: the NEQ calculation yields intensities coming out of the surge that are a factor of between two and 10 larger than when SE is assumed. For O IV, instead, the NEQ and SE calculations yield similar integrated intensities. For O IV, therefore, the NEQ calculations are important mainly to determine derived quantities like number densities of emitters n_u (Section 4.1) and temperatures (Section 4.2). In addition, we have found that for Si IV all the regions in the surge have a greater intensity than the QTR: this can explain why the surge can be observationally distinguished from the QTR, as found in the NS2017 paper.

The high brightness of various features in the surge has been seen to arise in no small part from different LOS effects tied to the peculiarly irregular shape of its TR, and, in particular, to its varying inclination and the folds that develop in it (Section 5.2). On the one hand, whenever LOS and the tangent plane to the TR are not mutually orthogonal, the issuing intensity collects emissivity from a larger number of plasma elements in the TR (alignment effect); on the other hand, given that the surge's TR is variously folded, forming crests and wedges, the LOS crosses the emitting layer multiple times (multiple-crossing effect). The alignment and multiple-crossing effects are quite evident in the footpoints and crests. This explains their remarkable brightness and makes clear their potential as beacons to indicate the presence of those special features in surge-like phenomena when observed in TR lines like Si IV (Figure 11). Additionally, the multiple crossings can also have an impact on the observed Doppler shifts since we could be integrating various emitting layers with different dynamics. So, when confronted with a TR observation of a region where a surge is taking place, the detection of strong brightenings in Si IV and O IV could help unravel the geometry of the surge. Furthermore, since the internal footpoint of the surge is close to the reconnection site, we might also find observational evidences of reconnection in the neighborhood. This provides theoretical support to the location of the brightenings in the *IRIS* observations by NS2017. In addition, if strong signals are observed in Si IV related to some moderate signal in O IV, they could correspond to the crests and the external footpoint of the surge; nonetheless, the rest of the surge structure could be only differentiated from the TR in Si IV.

We gratefully acknowledge financial support by the Spanish Ministry of Economy and Competitiveness (MINECO) through projects AYA2011-24808 and AYA2014-55078-P, as well as by NASA through grants NNX16AG90G, NNH15ZDA001N, and NNX17AD33G and by NSF grant AST1714955 and contract NNG09FA40C (*IRIS*). We also acknowledge the computer resources and assistance provided at the MareNostrum (BSC/CNS/RES, Spain) and TeideHPC (ITER, Spain) supercomputers, where the calculations have been carried out, and at the Pleiades cluster (computing projects s1061, s1472, and s1630 from the High End Computing division of NASA), where relevant code developments have been made. Finally, the authors are grateful to Dr. Peter R. Young for his suggestions during the *Hinode*-11/*IRIS*-8 science meeting, and also to Dr. Jaroslav Dudík for his constructive comments to improve the paper.

ORCID iDs

D. Nóbrega-Siverio https://orcid.org/0000-0002-7788-6482
J. Martínez-Sykora https://orcid.org/0000-0002-0333-5717

References

Asplund, M., Grevesse, N., Sauval, A. J., & Scott, P. 2009, ARA&A, 47, 481
Bohlin, J. D., Vogel, S. N., Purcell, J. D., et al. 1975, ApJL, 197, L133
Bradshaw, S. J., & Cargill, P. J. 2006, A&A, 458, 987
Bradshaw, S. J., & Klimchuk, J. A. 2011, ApJS, 194, 26
Bradshaw, S. J., & Mason, H. E. 2003, A&A, 401, 699
Canfield, R. C., Reardon, K. P., Leka, K. D., et al. 1996, ApJ, 464, 1016
Carlsson, M., & Leenaarts, J. 2012, A&A, 539, A39
Chae, J., Schühle, U., & Lemaire, P. 1998, ApJ, 505, 957

De Pontieu, B., De Moortel, I., Martinez-Sykora, J., & McIntosh, S. W. 2017, ApJL, 845, L18
De Pontieu, B., McIntosh, S., Hansteen, V. H., et al. 2007, PASJ, 59, 655
De Pontieu, B., McIntosh, S., Martinez-Sykora, J., Peter, H., & Pereira, T. M. D. 2015, ApJL, 799, L12
De Pontieu, B., Title, A. M., Lemen, J. R., et al. 2014, SoPh, 289, 2733
Doschek, G. A. 2006, ApJ, 649, 515
Doschek, G. A., Warren, H. P., Mariska, J. T., et al. 2008, ApJ, 686, 1362
Drews, A., & Rouppe van der Voort, L. 2017, A&A, 602, A80
Dudík, J., Del Zanna, G., Dzifčáková, E., Mason, H. E., & Golub, L. 2014, ApJL, 780, L12
Dudík, J., et al. 2017, SoPh, 292, 100
Dzifčáková, E., Vocks, C., & Dudík, J. 2017, A&A, 603, A14
Feldman, U., Landi, E., & Doschek, G. A. 2008, ApJ, 679, 843
Georgakilas, A. A., Koutchmy, S., & Alissandrakis, C. E. 1999, A&A, 341, 610
Golding, T. P., Carlsson, M., & Leenaarts, J. 2014, ApJ, 784, 30
Golding, T. P., Leenaarts, J., & Carlsson, M. 2016, ApJ, 817, 125
Griem, H. R. 1964, Plasma Spectroscopy (New York: McGraw-Hill)
Gudiksen, B. V., Carlsson, M., Hansteen, V. H., et al. 2011, A&A, 531, A154+
Guglielmino, S. L., Bellot Rubio, L. R., Zuccarello, F., et al. 2010, ApJ, 724, 1083
Hansteen, V. 1993, ApJ, 402, 741
Hansteen, V. H., Archontis, V., Pereira, T. M. D., et al. 2017, ApJ, 839, 22
Hansteen, V. H., De Pontieu, B., Rouppe van der Voort, L., van Noort, M., & Carlsson, M. 2006, ApJ, 647, L73
Hayek, W., Asplund, M., Carlsson, M., et al. 2010, A&A, 517, A49+
Hayes, M., & Shine, R. A. 1987, ApJ, 312, 943
Jiang, R.-L., Fang, C., & Chen, P.-F. 2012, ApJ, 751, 152
Joselyn, J. A., Munro, R. H., & Holzer, T. E. 1979, ApJS, 40, 793
Katsukawa, Y., Berger, T. E., Ichimoto, K., et al. 2007, Sci, 318, 1594
Kayshap, P., Srivastava, A. K., Murawski, K., & Tripathi, D. 2013, ApJL, 770, L3
Kurokawa, H., Liu, Y., Sano, S., & Ishii, T. T. 2007, in ASP Conf. Ser. 369, New Solar Physics with Solar-B Mission, ed. K. Shibata, S. Nagata, & T. Sakurai (San Francisco, CA: ASP), 347
Leenaarts, J., Carlsson, M., Hansteen, V., & Gudiksen, B. V. 2011, A&A, 530, A124
Leenaarts, J., Carlsson, M., Hansteen, V., & Rutten, R. J. 2007, A&A, 473, 625
MacTaggart, D., Guglielmino, S. L., Haynes, A. L., Simitev, R., & Zuccarello, F. 2015, A&A, 576, A4
Martínez-Sykora, J., De Pontieu, B., Hansteen, V. H., & Gudiksen, B. 2016, ApJ, 817, 46
Martínez-Sykora, J., Hansteen, V., & Carlsson, M. 2008, ApJ, 679, 871
Moreno-Insertis, F., & Galsgaard, K. 2013, ApJ, 771, 20
Murawski, K., Srivastava, A. K., & Zaqarashvili, T. V. 2011, A&A, 535, A58
Nishizuka, N., Shimizu, M., Nakamura, T., et al. 2008, ApJL, 683, L83
Nóbrega-Siverio, D., Martínez-Sykora, J., Moreno-Insertis, F., & Rouppe van der Voort, L. 2017, ApJ, 850, 153
Nóbrega-Siverio, D., Moreno-Insertis, F., & Martínez-Sykora, J. 2016, ApJ, 822, 18
Olluri, K., Gudiksen, B. V., & Hansteen, V. H. 2013a AJ, 145, 72
Olluri, K., Gudiksen, B. V., & Hansteen, V. H. 2013b ApJ, 767, 43
Olluri, K., Gudiksen, B. V., Hansteen, V. H., & De Pontieu, B. 2015, ApJ, 802, 5
Pereira, T. M. D., De Pontieu, B., & Carlsson, M. 2012, ApJ, 759, 18
Polito, V., Del Zanna, G., Dudík, J., et al. 2016, A&A, 594, A64
Raymond, J. C., & Dupree, A. K. 1978, ApJ, 222, 379
Reep, J. W., Warren, H. P., Crump, N. A., & Simões, P. J. A. 2016, ApJ, 827, 145
Rouppe van der Voort, L., De Pontieu, B., Scharmer, G. B., et al. 2017, ApJL, 851, L6
Scharmer, G. B., Bjelksjo, K., Korhonen, T. K., Lindberg, B., & Petterson, B. 2003, SPIE, 4853, 341
Shibata, K., Nozawa, S., & Matsumoto, R. 1992, PASJ, 44, 265
Smith, R. K., & Hughes, J. P. 2010, ApJ, 718, 583
Yang, H., Chae, J., Lim, E.-K., et al. 2014, ApJL, 790, L4
Yang, L., He, J., Peter, H., et al. 2013, ApJ, 777, 16
Yang, L., Peter, H., He, J., et al. 2018, ApJ, 852, 16
Yokoyama, T., & Shibata, K. 1995, Natur, 375, 42
Yokoyama, T., & Shibata, K. 1996, PASJ, 48, 353
Zwaan, C. 1987, ARA&A, 25, 83

5

Code development to speed up ambipolar diffusion calculations and preliminar results.

In Section 1.3.4 of the Introduction, we briefly explained that partial ionization effects and collisional decoupling can noticeably affect the low solar atmosphere and, consequently, the associated phenomena such as type-II spicules (Martínez-Sykora et al., 2017) or those in connection with flux emergence (Leake & Arber, 2006; Arber et al., 2007; Leake & Linton, 2013). As mentioned in Section 1.4.1, in the Bifrost code there is an available module developed by Martínez-Sykora et al. (2012) that includes the ambipolar diffusion and Hall terms in the calculations; however, the inclusion of both terms imposes strong constraints with respect to the timestep of the computations. In this chapter, we explain the new Fortran module we have developed as part of the thesis to extend the capabilities of the Bifrost code concerning this problem. In particular, the module contains a numerical method called Super Time-Stepping (STS; Alexiades et al., 1996) to speed up the calculations that take into account the ambipolar diffusion. The layout of this chapter is as follows. Section 5.1 details the relevant equations for the ambipolar and Hall terms. In Section 5.2, we describe the STS method, together with its implementation in the Bifrost code and the validation tests. Finally, Section 5.3 shows some preliminary results in relation to flux emergence and surges obtained with this new module.

5.1 The generalized Ohm's law

As anticipated in Section 1.3.4, there is a way to relax the MHD approximation to take into account the relative speed and associated friction between neutrals, ions and electrons, in Ohm's law without having to add extra equations to the system, i.e., still treating the plasma as a single fluid. Ohm's law is basically a relation between the electric field and the electric current that makes it possible to overcome the difficulties of dealing with multifluid plasmas. In a reference frame locally moving with a plasma element, it can be shown (see,

e.g., Mitchner & Kruger, 1973) that the relation between the electric current and electric field is given by

$$\mathbf{E}' = \tilde{\eta}_{Hall}(\mathbf{J}' \times \mathbf{B}') - \tilde{\eta}_{amb}(\mathbf{J}' \times \mathbf{B}') \times \mathbf{B}' + \eta \mathbf{J}', \tag{5.1}$$

where $\mathbf{E}'$ is the electric field, $\mathbf{B}'$ the magnetic field, and $\mathbf{J}'$ the current density all measured in that reference frame. This is called the generalized Ohm's law. The coefficient η is the standard ohmic diffusion given by

$$\eta = \frac{m_e \nu_{e,ni}}{n_e e^2}, \tag{5.2}$$

$\hat{\eta}_{amb}$ is the ambipolar diffusion coefficient described by

$$\hat{\eta}_{amb} = \frac{\eta_{amb}}{B^2} = \frac{(\rho_n/\rho)^2}{\rho_i \nu_{in}} = \frac{(\rho_n/\rho)^2}{\rho_n \nu_{ni}}, \tag{5.3}$$

and the Hall coefficient $\tilde{\eta}_{Hall}$ is defined as

$$\tilde{\eta}_{Hall} = \frac{1}{e n_e}, \tag{5.4}$$

where e is the electron charge; n_e the density number of electrons; m_e the electron mass; ρ_n the neutral mass density; ρ the total mass density; $\nu_{e,ni}$ the total collision frequency between electrons and neutrals and ions; and, finally, ν_{in} and ν_{ni} are the ion-neutral and neutral-ion collision frequencies, respectively

5.1.1 The induction equation

Going over now to the laboratory reference frame where the plasma element is moving with a velocity $\mathbf{u}$, the electric field, the electric current and the magnetic field are given by $\mathbf{E} = \mathbf{E}' - \mathbf{u} \times \mathbf{B}$, $\mathbf{J} = \mathbf{J}'$, and $\mathbf{B} = \mathbf{B}'$, respectively. Using Faraday induction equation and Equation (5.1), one obtains a generalized induction equation, namely,

$$\frac{\partial \mathbf{B}}{\partial t} = \nabla \times \left[\mathbf{u} \times \mathbf{B} - \tilde{\eta}_{Hall}(\mathbf{J} \times \mathbf{B}) + \tilde{\eta}_{amb}(\mathbf{J} \times \mathbf{B}) \times \mathbf{B} - \eta \mathbf{J} \right] \tag{5.5}$$

This induction equation contains two new terms in comparison with the one from the classic resistive MHD: a term proportional to $\mathbf{J} \times \mathbf{B}$, which includes the changes in the magnetic field due to the Hall effect; and another one proportional to $(\mathbf{J} \times \mathbf{B}) \times \mathbf{B}$, which is related to the changes of the magnetic field owing to ambipolar diffusion. Those terms cannot lead to changes in the magnetic topology and, consequently, neither produce magnetic reconnection. This can be seen if we define

$$\mathbf{u}_{amb} = \tilde{\eta}_{amb}(\mathbf{J} \times \mathbf{B}) \tag{5.6}$$

and

$$\mathbf{u}_{Hall} = -\tilde{\eta}_{Hall} \mathbf{J} \tag{5.7}$$

for the ambipolar and Hall term, respectively. With those notations,

$$\frac{\partial \mathbf{B}}{\partial t} = \nabla \times \left[\left(\mathbf{u} + \mathbf{u}_{_{Hall}} + \mathbf{u}_{_{amb}} \right) \times \mathbf{B} - \eta \mathbf{J} \right] \tag{5.8}$$

which means that the magnetic field is no longer frozen into the plasma flow, but it is frozen into a pseudo-flow with speed $\mathbf{u} + \mathbf{u}_{_{Hall}} + \mathbf{u}_{_{amb}}$; when $\eta = 0$, the topology is preserved and there is no magnetic reconnection.

5.1.2 The energy equation

In general, the power exerted by the electromagnetic field on the plasma is given by $\mathbf{J}' \cdot \mathbf{E}'$. Substituting the generalized Ohm's law (Equation 5.1), we see that, in addition to the classic ohmic dissipation ηJ^2, there appears a new term that leads to an irreversible entropy increase, namely,

$$Q_{_{amb}} = \eta_{_{amb}} J_\perp^2, \tag{5.9}$$

where $J_\perp$ is the current component perpendicular to the magnetic field. This dissipation term is associated with the collisions between neutrals and ions and, hereafter, we refer to it as ambipolar dissipation. As a consequence, when taking into account ion-neutral interaction effects, a new entropy source has to be added to the energy equation as follows:

$$\frac{\partial e}{\partial t} = -\nabla \cdot (e\mathbf{u}) - P \nabla \cdot \mathbf{u} + \eta J^2 + \eta_{_{amb}} J_\perp^2 + Q_{_{rad}} + Q_{_{Spitz}} \tag{5.10}$$

where e is the internal energy per unit volume, P the gas pressure, $Q_{_{rad}}$ represents all the entropy sources due to radiation terms, and $Q_{_{Spitz}}$ is the entropy source due to the thermal Spitzer conductivity. Note that the Hall term does not cause any energy dissipation since it is perpendicular to $\mathbf{J}$.

5.1.3 Collision cross sections and frequencies

Collision cross sections and frequencies are important quantities when determining the rate at which electrons and the different ions and neutrals interact with each other. Martínez-Sykora et al. (2012) showed that the approximation chosen to determine the values of collision cross sections and frequencies is crucial for ion-neutral interaction effects: there are significant discrepancies in the ambipolar diffusion coefficient depending on the assumption considered. Consequently, this leads to different results for the thermal properties of the solar atmosphere, primarily in the chromosphere where the ambipolar diffusion is more relevant (Martínez-Sykora et al., 2015).

In order to obtain the most accurate calculation so far, we have included the state-of-the-art approximation of the mentioned parameters. This implementation has already been used by Martínez-Sykora et al. (2016a); De Pontieu et al. (2017a); Martínez-Sykora et al. (2017); De Pontieu et al. (2017b); Martínez-Sykora et al. (2017) and is detailed in the following.

- *Collision frequency.*
  The collision frequency $\nu_{_{ni}}$ between neutrals n and charged particles i follows the

description given by Spitzer (1956):

$$\nu_{ni} = n_i \sigma_{ni} \left(\frac{8 K_B T}{\pi \mu_{ni}} \right)^{1/2} \qquad n = 1, 2; \quad i = 1, ..., 16 \tag{5.11}$$

where σ_{ni} is the cross section between a given neutral and ion; n_i is the number density of the ion i; $K_B = 1.381 \times 10^{-16}$ erg K^{-1} is the Boltzmann constant, T the temperature, and $\mu_{ni} = m_n m_i / (m_n + m_i)$ is the reduced mass of the neutral and ion species. In the above equation, we only consider two types of neutrals: neutral hydrogen (subindex $n = 1$) and neutral helium ($n = 2$). For the ions, we only take into account the first ionization of the 16 most abundant elements in the Sun.

- *Cross sections.*
  Concerning the cross sections σ_{ni}, we use tabulated tables that provide their dependence with temperature for the following collisions: p-H, proton and neutral hydrogen; p-He, proton and neutral helium; and He^+ - He, single ionized helium and neutral helium (see Vranjes & Krstic, 2013, and references therein). The rest of the collision cross sections are not well-known, so we adopt the same assumption as made by Vranjes et al. (2008): we take the cross section between hydrogen (or helium) and heavy ions multiplied by m_i/m_H (or m_i/m_{He}).

5.2 Super Time-Stepping (STS) method

The solution of diffusion problems, such as thermal conduction or ambipolar diffusion via explicit numeric schemes is intrinsically difficult due to the parabolic nature of the corresponding differential equations. According to the Courant-Friedrichs-Lewy (CFL) criterion (Courant et al., 1928), the maximum timestep, Δt_{CFL}, for the numerical solution of parabolic problems using explicit schemes decreases as the square of the spatial resolution Δx, i.e.,

$$\Delta t_{CFL} \propto \frac{\Delta x^2}{u}, \tag{5.12}$$

where u represents the fastest characteristic wave velocity of the system. Wherever high spatial resolution is required, this quadratic dependence can strongly limit the calculation speed in comparison with MHD computations, whose Δt is linearly dependent on Δx. As a consequence, high-resolution experiments of diffusion problems are virtually imposible to carry out explicitly. An alternative would be to use an implicit or semi-implicit scheme; nonetheless, this approach also presents strong limitations concerning memory usage and, moreover, its implementation in numerical codes is non-trivial.

The Super Time-Stepping (STS; Alexiades et al., 1996) is a technique that can be used to accelerate explicit parabolic calculations. It is based on the stability properties of the Chebyshev polynomials, which relaxes the CFL condition and allows us to take a larger timestep, Δt_{STS}, given by

$$\Delta t_{STS} = \frac{n}{2\sqrt{\nu}} \left[\frac{(1+\sqrt{\nu})^{2n} - (1-\sqrt{\nu})^{2n}}{(1+\sqrt{\nu})^{2n} + (1-\sqrt{\nu})^{2n}} \right] \Delta t_{CFL} \ , \tag{5.13}$$

which is divided into n sub-timesteps τ_i as follows:

$$\Delta t_{STS} = \sum_{i=1}^{n} \tau_i \quad \text{with} \quad \tau_i = \Delta t_{CFL} \left[(\nu - 1) \cos\left(\frac{\pi(2i-1)}{2n} \right) + (\nu + 1) \right]^{-1} , \tag{5.14}$$

where Δt_{CFL} is the timestep of the parabolic problem given by the classic CFL condition, $\nu \in (0, 1)$ is a damping factor, and n is a positive integer. It is important to note that the intermediate values computed along the n sub-timesteps have no approximating properties: it is only after the whole Δt_{STS} has been reached that the results approximate the solution and, consequently, have a physical meaning.

The above expressions can be easily implemented to improve the calculation efficiency of ambipolar diffusion experiments (see, e.g., O'Sullivan & Downes, 2006, 2007; Choi et al., 2009) or to solve the thermal conduction problem (Meyer et al., 2012; Iijima & Yokoyama, 2015); nevertheless, the drawback is that the STS is a first order scheme in time. In addition, the method has two free parameters, n and ν, and it is necessary to carefully choose their values to optimize the performance while keeping numerical stability. The maximum ratio $\Delta t_{STS}/\Delta t_{CFL}$ that can be reached for any given n corresponds to the following limit:

$$\lim_{\nu \to 0} \frac{\Delta t_{STS}}{\Delta t_{CFL}} = \lim_{\nu \to 0} \frac{n}{2\sqrt{\nu}} \left[\frac{(1+\sqrt{\nu})^{2n} - (1-\sqrt{\nu})^{2n}}{(1+\sqrt{\nu})^{2n} + (1-\sqrt{\nu})^{2n}} \right] = n^2 \tag{5.15}$$

In this limit, the CFL criterion would need n^2 steps to reach one Δt_{STS}, while the STS method requires just n, as explained above (Equation 5.14). Assuming a similar computing load for each step (whether in the STS or in the CFL-limited calculation), this implies that the STS method would be n times faster than the simple CFL-limited one. However, it is necessary to impose a lower threshold for ν, since $\nu = 0$ is a stability limit, and choosing small values of ν can make the STS method very sensitive to round-off errors (Alexiades et al., 1996). In the next subsection, we explain the choices made for ν and n for the module developed in this thesis.

5.2.1 Implementation of the STS method in the Bifrost code

In this section, we show how to deal with the STS implementation and the choice of the n and ν parameters.

Operator splitting

Operator splitting is a standard technique to advance in time the solution at each timestep separately for groups of terms that contain different physics (hence with different numerical requirements). In our case, the induction and energy equations (Equations 5.5 and 5.10, respectively) are separated and solved over a timestep Δt determined by the minimum of the two following values: 1) the standard Δt given by the MHD and radiation terms considered in the Bifrost code (see Gudiksen et al., 2011, for further details); and 2) the Δt imposed by the ambipolar and Hall terms that appear in the generalized Ohm's law from Equation

(5.1). Thanks to the operator splitting, it is possible to simplify the overall solution process while keeping the code modular.

In this thesis, in particular, we take advantage of the operator splitting to solve separately the ambipolar diffusion term using, when necessary, the STS method. In order to determine whether the STS method can be applied, let us assume a system in which

$$\Delta t_{MHD,CFL} = C\,\Delta t_{AD,CFL}, \quad C \in \mathbb{R}^{+}. \tag{5.16}$$

In this equation, $\Delta t_{MHD,CFL}$ is the timestep given by the CFL criterion for the standard MHD part, and $\Delta t_{AD,CFL}$, the one for the ambipolar diffusion term. For any acceleration method, like the STS, to be of interest, it is obviously necessary that $\Delta t_{MHD,CFL} > \Delta t_{AD,CFL}$, i.e., $C > 1$.

Choice of the free parameters n and ν

In the literature, there is no thorough analysis of the choice of the n and ν parameters, so the use of STS method is not precisely specified. In the following, we detail various aspects that should be considered.

1. Δt_{STS} cannot be larger than the timestep imposed by the general MHD and radiation terms, i.e., $\Delta t_{MHD,CFL}$, since the time advance of the system is limited by the minimum of all applicable timestep conditions. Consequently,

$$\Delta t_{AD,CFL} \leq \Delta t_{STS} \leq \Delta t_{MHD,CFL}\ . \tag{5.17}$$

   This condition can be rewritten using Equations (5.16) and 5.13:

$$1 \leq \frac{n}{2\sqrt{\nu}}\left[\frac{(1+\sqrt{\nu})^{2n}-(1-\sqrt{\nu})^{2n}}{(1+\sqrt{\nu})^{2n}+(1-\sqrt{\nu})^{2n}}\right] \leq C \tag{5.18}$$

   with $\nu \in (0,1)$ and $C > 1$. The above is the minimum requirement to apply the STS method. Note that for $n = 1$ the function at the center of the inequality is below 1 for all $\nu > 0$, so, since n is an integer, Equation (5.18) implies $n \geq 2$.

2. We now tighten the lower bound of Equations (5.17) and (5.18) as follows: for the STS method to be computationally advantageous, its n substeps must permit a greater advance in time than n times the timestep $\Delta t_{AD,CFL}$. Thus, in Equation (5.17) we set $n\Delta t_{AD,CFL} < \Delta t_{STS}$, so the lower bound of Equation (5.18) becomes

$$n < \frac{n}{2\sqrt{\nu}}\left[\frac{(1+\sqrt{\nu})^{2n}-(1-\sqrt{\nu})^{2n}}{(1+\sqrt{\nu})^{2n}+(1-\sqrt{\nu})^{2n}}\right] \tag{5.19}$$

   For simplicity, in the following we call $f(n,\nu)$ the term on the right of the above expression, and we show that this constraint imposes a maximum value for ν. To that end, in Figure 5.1 we have plotted $f(n,\nu)$ against n for different values of ν (dashed lines). In the image, the solid red curve is $f(n,\nu) = n^2$, which corresponds to the limit

of stability ($\nu = 0$). The solid black curve is simply the straight $f(n, \nu) = n$ that allows us to discern which the combinations of n and ν verify the above inequality. As seen in the figure, $f(n, \nu) = n$ roughly coincides with the curve $\nu = 0.25$. In fact, through a limit analysis of $f(n, \nu)/n$,

$$\lim_{n\to\infty} \frac{1}{2\sqrt{\nu}} \left[\frac{(1+\sqrt{\nu})^{2n} - (1-\sqrt{\nu})^{2n}}{(1+\sqrt{\nu})^{2n} + (1-\sqrt{\nu})^{2n}} \right] = \frac{1}{2\sqrt{\nu}}, \tag{5.20}$$

we find that the constraint $f(n, \nu)/n = 1$ give us an asymptotic limit of ν, namely, $\nu = 0.25$: the maximum value of ν that results from the optimization constraint imposed in this bullet. In the code, to avoid working with asymptotic limits, we use as the upper limit of ν, the one obtained for the lowest n possible ($n = 2$), namely, $\nu < \sqrt{5} - 2$.

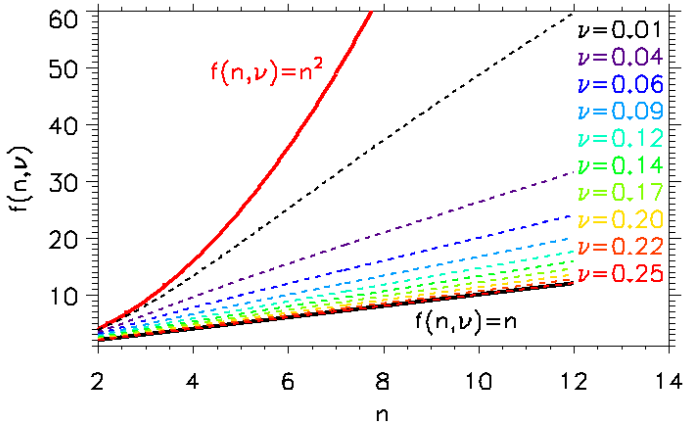

FIGURE 5.1— Plot showing $f(n, \nu)$ versus n for different values of ν (dashed curves). Solid lines represent $f(n, \nu) = n^2$ (red) and $f(n, \nu) = n$ (black).

3. There is also a strong constraint concerning the use of large n. In principle, it would be mathematically possible to have any value of n; nonetheless, numerically, large values of n can be problematic. This is because during the n sub-cycling shown in Equation (5.14), the inner values obtained within the loop do not have any physical meaning and they can reach very large values that compromise the accuracy of the calculations due to the limited precision. There are three ways to alleviate this problem: (a) increasing from single to double precision, which allows calculations with larger values of n but requiring more memory; (b) introducing a fancy normalization, which helps to avoid Infinity or !NAN values but increases the number of operations and complicates its implementation; (c) imposing a strict maximum of n according to the experience. The latter is the solution we have adopted and requires some testing to discern the valid n

that will keep stable the simulations. From experiments similar to those that we have run during the course of this thesis, we find that n starts to be problematic above 12, approximately. In order to ensure greatest stability, we have decided to impose as a maximum $n = 10$. This, together with the previous considerations, gives us the two following ranges we must fulfill: $0 < \nu < \sqrt{5} - 2$ and $2 \leq n \leq 10$. In Figure 5.2, the valid parameter-space derived from those ranges is shown within the three solid red lines of the image.

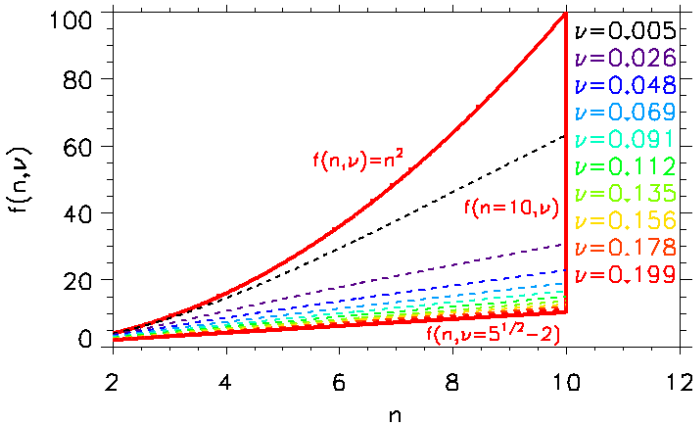

FIGURE 5.2— Plot showing $f(n, \nu)$ versus n for different values of ν (dashed curves). Solid lines represent the boundaries of the parameter-space taking into account the constraints described in the tex related to optimization and stability, namely, $f(n, \nu) = n^2$, $f(n = 10, \nu)$ and, $f(n, \nu = \sqrt{5} - 2)$.

4. The final step to determine the optimum combination of n and ν can be taken now. The ideal situation would be to reach $\Delta t_{MHD,CFL}$ in the minimum number of stable n steps. To that end, we impose,

$$\Delta t_{STS} = \Delta t_{MHD,CFL} \tag{5.21}$$

which implies the following relationship between n and ν:

$$f(n, \nu) = \frac{n}{2\sqrt{\nu}} \left[\frac{(1 + \sqrt{\nu})^{2n} - (1 - \sqrt{\nu})^{2n}}{(1 + \sqrt{\nu})^{2n} + (1 - \sqrt{\nu})^{2n}} \right] = C \tag{5.22}$$

Recalling that n must be an integer, the minimum number of substeps in which the above equation occurs when $\nu \to 0$, so, from Equation (5.15), $n = int(\sqrt{C})$. Since $\nu = 0$ corresponds to the limit of stability, one should consider $n > int(\sqrt{C})$. The first option would be to use $n = \sqrt{C} + 1$; nevertheless, the associated ν could still be small to affect our calculations by round-off errors (Alexiades et al., 1996). For those

reasons, in our STS calculations we impose

$$n = int(\sqrt{C}) + 2 \quad \text{with} \quad C > 4 \tag{5.23}$$

For the cases when $2 \leq C \leq 4$, instead of STS, we apply the subcycling method described by Leake & Arber (2006) and Martínez-Sykora et al. (2017); when $1 \leq C \leq 2$, we follow the CFL criterion.

Having determined n, we can see that for each n there is a limited range of values of ν that satisfies Equation (5.22). This is illustrated in Figure 5.3 through a 2D map of C/n only showing the valid ν in logarithm scale for a given n. In the image, we have overplotted a red horizontal line to delimit $\nu = \sqrt{5} - 2$, and a black one that delineates the minimum value of ν for the maximum $n = 10$ ($\nu \approx 0.00185$).

Using the criteria just indicated for the choice of the ν and n parameters, we can get the best performance, optimizing the stability and speed for the ambipolar diffusion calculations in the Bifrost code.

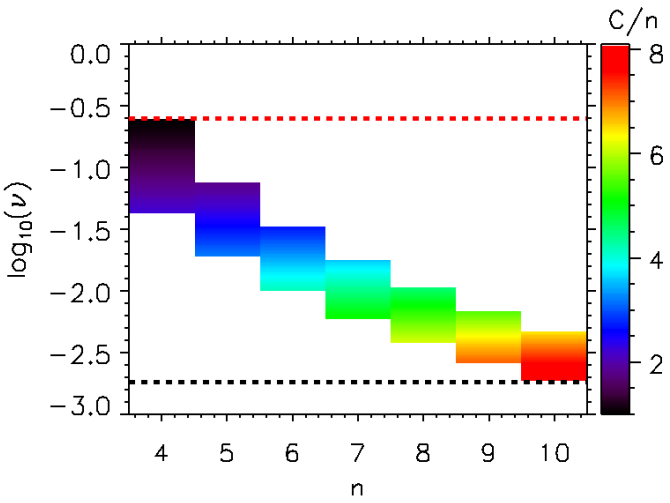

FIGURE 5.3— 2D map of C/n only showing in color the combinations of n and ν that verify Equation (5.22). In the image, a red horizontal line is superimposed to delimit the value $\nu = \sqrt{5} - 2$, and another one to point out the minimum value of ν for the maximum $n = 10$ ($\nu \approx 0.00185$)

5.2.2 Validation test

After programming the STS following the parameter choice described before, we need to verify that the STS is correctly implemented in the Bifrost code. To that end, we have

proceeded with a test that has the advantage that allows us to verify the method in 2.5D MHD scenarios for different initial conditions. This is possible thanks to the existence of a self-similar analytical solution found by Moreno-Insertis (2018). In the following, we describe this analytical solution and the goodness of our STS implementation.

Self-similar solution for ambipolar diffusion problems

The test we intent to carry out is based on the induction equation when only taking into account the ambipolar term, i.e., the pure ambipolar diffusion case. If we also assume that the ambipolar coefficient $\hat{\eta}_{amb}$ is homogeneous, the induction equation becomes

$$\frac{\partial \mathbf{B}}{\partial t} = \hat{\eta}_{amb} \nabla \times [(\mathbf{J} \times \mathbf{B}) \times \mathbf{B}] \,. \tag{5.24}$$

In a 2D domain with polar coordinates, this equation becomes a non-linear diffusion equation when considering an axisymmetric function for $\mathbf{B}$. The self-similar solution tends asymptotically, for large t, to the following shape (All relevant details about the natural timescale to reach the asymptotic solution can be found in the paper by Moreno-Insertis, 2018):

$$B_y(r,t) \longrightarrow \left(\frac{\Phi}{4\pi\eta_{_{amb}} t}\right)^{1/3} \left[1 - \frac{r^2}{R^2(t)}\right]^{1/2}, \quad \text{for} \quad r < R(t),\ 0 \text{ otherwise} \tag{5.25}$$

where

$$R^2(t) \longrightarrow \frac{3}{2}\left[4\eta_{_{amb}} t \left(\frac{\Phi}{\pi}\right)^2\right]^{1/3}, \tag{5.26}$$

Φ is the magnetic flux, y is the symmetry axis, and $r^2 = (x - x_0)^2 + (z - z_0)^2$. From those expressions, it is clear that $B_y \propto t^{-1/3}$ and $R \propto t^{1/6}$. The problem has the additional feature that any single-lobed initial condition with total flux Φ also tends, asymptotically in time, to the shape given in Equations (5.25) and (5.26). This is a robust multidimensional test to check whether the STS method was properly implemented in the code.

Numerical test

In order to test the STS method with the previous self-similar solution, we create a 2.5D snapshot of 1024×1024 points. The physical domain spans from $-4.9939 \leq x \leq 7.4939$ Mm to $-4.9939 \leq z \leq 7.4939$ Mm, with a numerical resolution of $\Delta x = \Delta z = 12.2070$ km. In that domain, we define as initial condition the following axisymmetric function for the magnetic field

$$B_{y0}(x,z) = B_0 e^{-\left[(x-x_0)^2 + (z-z_0)^2\right]/w^2} \tag{5.27}$$

where $B_0 = 0.8$ G, $x_0 = 0$ Mm, $z_0 = 0$ Mm, and $w = 0.5$ Mm. The rest of parameters are representative of the chromosphere: the initial internal energy per unit volumen is $e_0 = 4 \times 10^{-3}$ erg cm^{-3}; the initial density $\rho_0 = 10^{-9}$ g cm^{-3}; and the ambipolar diffusion coefficient is set to a constant, namely, $\tilde{\eta}_{_{amb}} = 10^{16}$ cm^2 s^{-1} G^{-2}. As mentioned above, this

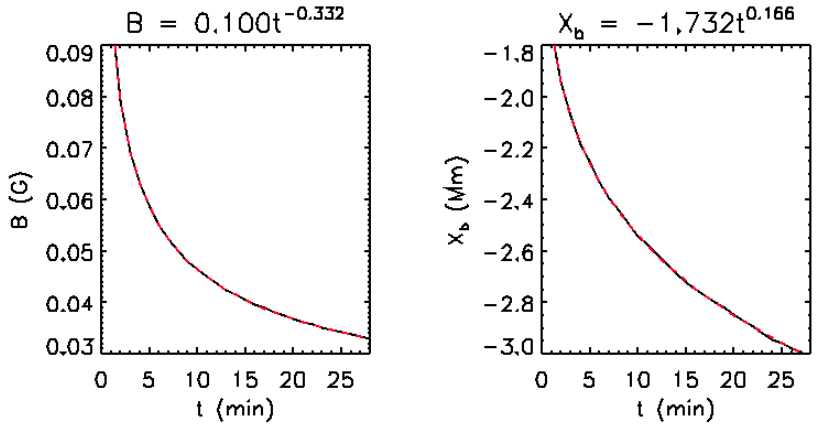

FIGURE 5.4— Results of the STS validation test for the self-similar solution. A) Evolution of the maximum of the magnetic field with time (black) and polynomial fit (red). B) Evolution of X_b with time (black) and polynomial fit (red). Above each panel is shown the resulting fit formula.

initial condition converges to the self-similar solution with the same integrated magnetic flux after an initial transient phase.

We have solved the problem using 64 CPUs at the Teide-HPC supercomputer (see the details of this facility in Section 1.4.3). The results are shown in Figure 5.4. In the image, the left panel illustrates the evolution of the maximum of the magnetic field with time through a black line. The polynomial fit of that curve is shown in red; and the resulting power-law fit formula is shown in the upper part of the panel, namely,

$$B_y = 0.100\, t^{-0.332}. \tag{5.28}$$

The power of the fit agrees quite well with the predicted value $-1/3$ shown in Equation (5.25). On the other hand, the right panel contains the evolution of X_b (one of the cartesian components of R) with time (black curve) and its polynomial fit (red). The power-law fit yields

$$X_b = -1.732\, t^{0.166}, \tag{5.29}$$

which again agrees with the expected value $1/6$ from Equation (5.26). This tests indicates that our STS implementation is correct. In addition, to ascertain the speed-up factor that we gain by means of the STS, we have run the same test with the same number of CPUs under the CFL criterion and also using the subcycling method described by Leake & Arber (2006) and Martínez-Sykora et al. (2017). The results show that for this test, STS is able to compute 28 physical minutes in 1 hour and 40 minutes, the subcycling method lasts around 6 hours, and using CFL, it takes 20 hours: the advantage of using STS is more than evident

for a chromospheric-like situation like this, it leads to a speed-up factor of 3.6 and 12 with respect to the subcycling method and CFL, respectively.

5.3 Preliminary results

In this section, we show recent results obtained in the last stage of this thesis using the new Fortran module. Those results are preliminary, but constitute a first step toward understanding the role of ambipolar diffusion in the process of flux emergence and in the formation of surges.

5.3.1 Flux emergence with ambipolar diffusion

Inspired by the papers by Leake & Arber (2006), Arber et al. (2007), and Leake & Linton (2013), we aim at taking a look at the influence of the ambipolar diffusion on the flux emergence process. To that end, we have used the numerical experiment presented in Chapter 2, enabling the computation of ambipolar diffusion using the STS method. In particular, we turn on the ambipolar diffusion at $t = 40.0$ min of that simulation, an instant in which most of the twisted magnetic tube has reached the surface, to analyze the effects of the ion-neutral interactions in the emerged dome. For comparison reasons, we have calculated various implementations of collision cross sections and frequencies. The results after 13.3 minutes of enabling the ambipolar diffusion term are shown in Figure 5.5. In the image, panel A contains the initial stages of the formation of the emerged dome without ambipolar diffusion. Panel B shows the same instant as before but including the ambipolar diffusion effects using the state-of-the-art implementation for the collision frequencies and cross sections described in Section 5.1.3. Panels C, D and E also include ambipolar diffusion, but based on the simplified collision frequency assumptions of different authors; more specifically, panel C uses the collisional rates given by Fontenla et al. (1993); Panel D, the ones obtained from Osterbrock (1961), De Pontieu & Haerendel (1998) and De Pontieu et al. (2001); and panel E, the rates given by Geiss & Buergi (1986), von Steiger & Geiss (1989) and De Pontieu et al. (2001) (see the corresponding equations in the appendix of the paper by Martínez-Sykora et al. (2012)).

In the image, it is clear that the various assumptions in the collision cross sections and frequencies lead to different results, mainly in the emerged dome, after 13 minutes of enabling the ambipolar diffusion term. In particular, panels C, D and E show a more developed dome, in terms of expanded area, in comparison with panel B, while the latter is quite similar to the case without ambipolar diffusion (panel A). Furthermore, panels C, D and E, also show differences with respect to panel B in the temperature within the dome. This is clearly visible in its upper part, where there are differences up to 2000 K. The fact that the largest differences are located in the upper part of the dome is due to the fact that those regions are rarefied as a result of gravitational downflows during the expansion process (see Chapter 2 for further details about the expansion process). Consequently, the ambipolar diffusion heating (Section 5.1.2) is more efficient in those regions. Apart from the dome, we can also find other differences in the chromosphere such as the feature around $x = 3$ Mm and

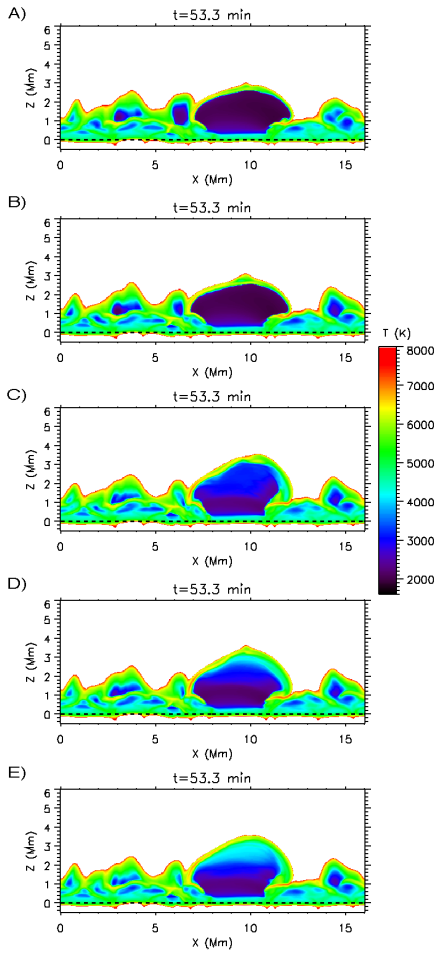

FIGURE 5.5— Temperature maps illustrating the effect of including ambipolar diffusion with the various implementations of collisional frequency. Panel A shows the experiment without ambipolar diffusion. Panel B contains ambipolar diffusion using the collision frequency calculation explained in Section 5.1.3. The rest of the panels are based on the collision frequency calculation of different authors compiled in the appendix of the paper by Martínez-Sykora et al. (2012), in particular, panel C) uses equations (A9) to (A11) from that paper; panel D), equations (A1) through (A4); and panel E), equations (A5) through (A8).

$z = 1.1$ Mm, in which Panel E shows the highest temperatures.

This preliminary result warns about how the assumptions in the collision cross sections and frequencies should be taken carefully, since they directly impact on the calculation of the ambipolar diffusion coefficient η_{amb} and, therefore, indirectly in the magnetic field evolution, the slippage between neutrals and the magnetic field, the amount of ambipolar diffusion heating, among others.

5.3.2 Impact of ambipolar diffusion on surges

The other preliminary result about ambipolar diffusion we would like to highlight in this thesis concerns its impact on the surge itself. To that end, in Figure 5.6 we show the same experiments as in panels A and B of Figure 5.5, but at a later instant, namely at $t = 61.6$ min, already in the launch stage of the surge. Through the temperature maps of the image, we can notice significant differences in the thermal properties between the cases without and with ambipolar diffusion (panels A and B, respectively). When not including ambipolar diffusion, the strong expansion during the flux emergence phase causes adiabatic cooling down to the threshold limit 1660 K (extended area in black in the temperature map that affects the dome and also the surge); when the temperature reaches 1660 K, an artificial ad-hoc heating is enabled to prevent the plasma from reaching even cooler temperatures (see Chapter 2 for further discussion). However, when considering the ion-neutral interactions, the associated heating is able to counteract such tremendous cooling. In panel B, the large black area in the surge and dome distinguishable in panel A has disappeared because it has been heated due to the ambipolar diffusion. Even the coolest region visible in panel B, the core of the emerged dome, is able to keep the plasma around 200 K above the temperature threshold needed in the case with no ambipolar diffusion so, in this case, it is not necessary to include any artificial ad-hoc heating. This may be a significant step forward with a view to determining the coolest temperatures in the solar atmosphere and, consequently, in related phenomena such as surges. In fact, this preliminary result suggests that the thermal properties of the Population C and, to a lesser extent, Population A (two of the surge populations described in Chapter 2) can change when including ambipolar diffusion; the inclusion of these thermal effects may therefore be of interest for the synthetic calculation of chromospheric lines such as Hα. It also seems to indicate that the thermal properties of the remaining populations, namely, B and D, are not affected by ambipolar diffusion. Note that the latter populations are located in the periphery of the surge and are related to the emission in TR lines and NEQ effects discussed in Chapter 4 of this thesis. It appears, therefore, that the inclusion of ambipolar diffusion may have interesting consequences for the thermodynamics of the surge and the diagnostics based on chromospheric lines. This line will be continued in the future extension of the work of this thesis (see Section 6.2).

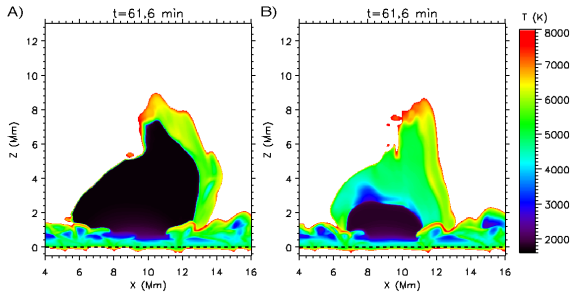

FIGURE 5.6— Temperature maps illustrating the differences for a surge experiment when not including ambipolar diffusion (panel A) and when taking it into account (panel B).

6

Conclusions and future perspective

6.1 Main conclusions of this thesis

In this section we summarize the main results and conclusions obtained for the four fundamental objectives of this thesis explained in Section 1.3.

6.1.1 Surges from a theoretical point of view

We have obtained the first radiative-MHD model of the formation and evolution of a surge, in 2.5D, with spatial domain extending from the solar interior to the corona using a realistic treatment of the atomic and radiation properties of the system. We used the Bifrost code that includes an advanced equation of state for the gas, detailed radiative transfer in the photosphere and chromosphere, and optically thin radiation and thermal conduction, which are of importance in the corona. Our model thus contains the emergence of magnetic flux through a self-consistent convection zone, and many aspects of the evolution of the surge plasma in the chromosphere, TR and corona that were impossible to calculate up to now. A detailed population study via Lagrange tracing allowed us to distinguish different plasma constituents in the surge, which differ in their dynamical and thermal evolution. We have found that the surge is not simply chromospheric plasma dragged by the magnetic field lines, as generally assumed; as a matter of fact, the surge is strongly affected by efficient heating and cooling mechanisms, to the point that a significant fraction of the surge could not be captured in previous theoretical papers due to the lack of a proper treatment of those mechanisms.

In the following, we highlight different conclusions of this theoretical part.

- **Thermal properties of the surge: the role of the entropy sources.**
  We have shown that the thermal evolution of the surge is strongly affected by some of the entropy sources, namely, Joule heating, viscous heating, thermal conduction, optically thin losses and, to a lesser extent, the cooling due to the radiative losses

by neutral hydrogen. In fact, we found that a non-small amount of the surge plasma reaches high temperatures during a fraction of its life, as a consequence of those entropy sources. The foregoing reinforces our conclusion that the idealized experiments of the past are missing a significant fraction of the surge phenomenon. Furthermore, this is of special interest regarding the observational and forward modeling results for the TR of the surge given in later chapters in the thesis. Also, on the basis of these results, a question arises of whether an adequate treatment of the entropy sources may be necessary to understand other ejective phenomena such as macrospicules. First indications in that sense have been recently provided by Kuźma et al. (2017).

- **Launch and decay of the surge.**
  Concerning the kinematics and dynamics, we have found that most of the surge suffers strong accelerations of tens to hundreds of the solar gravity ($g_\odot$) in the launch phase. In most cases, this is because of the large values of the Lorentz force but also, for one of the surge populations (population D, see Chapter 2), because of the large gas pressure gradients near the emerged plasma dome. A statistical study indicates that during the central and decay stages of the development of the surge, the majority of the plasma elements follow quasi-parabolic trajectories with downward acceleration close to $g_\odot$. In contrast to the previous theoretical literature (e.g., Yokoyama & Shibata, 1996; Nishizuka et al., 2008; Takasao et al., 2013; Jiang et al., 2012; Moreno-Insertis & Galsgaard, 2013; MacTaggart et al., 2015), our results finally provide a detailed quantitative assessment of the kinematics and dynamics of the surge. Our conclusions about the role of the Lorentz force and gas pressure gradient have recently been confirmed in the experiments by Yang et al. (2018).

- **The detachment process of the surge.**
  Studying the spatial jumps of the physical magnitudes (temperature, density, gas pressure, velocity and magnetic field), we have concluded that the formation of the surge is mediated by the formation of a deep wedge associated with a strong perpendicular shock. This shock is accompanied by a neighboring shock of the switch-off, slow kind located at the base of the hot jet that also appeared in the experiment. The shocks are caused by a chain of plasmoids generated in the reconnection site which impinge on the dense material of the incipient surge. The high levels of heating and compression in the postshock region lead to the formation of the wedge and the separation of the surge from the dome. Further indications about shocks related to surges have been studied very recently by other solar researchers (Ni et al., 2017; Zhao et al., 2018).

6.1.2 An observational perspective for the transition region of the surges

In this thesis we have opened a new observational avenue in the study of surges by using coordinated observations of chromospheric and TR lines. To that end, we took advantage of the high-resolution capabilities of the IRIS and SST facilities. Thus, we were able to explore the impact of surges in the TR and their close relation to UV bursts.

Using the coordinated observations reported in Chapter 3, we have studied the Hα surge that occurred on 2016 September 03 in active region AR 12585 that was accompanied by a UV

burst in its neighborhood. In those observations, we have found, for the first time, enhanced Si IV emission appearing within the domain of the surge. The Si IV profiles within the surge are broader and around a factor 2-5 brighter than a typical quiet-Sun Si IV profile, even if they are approximately 100 times fainter than the UV burst in the neighborhood. Prior to the publication of those results in 2017 (see Chapter 3), the existing literature had only reported the simultaneous appearance of surges, in chromospheric lines like Hα and Ca II 8542 Å, and UV bursts, observed in TR lines like Si IV 1402.77 Å, in neighboring locations but without detecting evidences of Si IV emission within the surge domain (Kim et al., 2015; Huang et al., 2017). This finding led us to one of the most striking conclusions of this thesis: surges, although traditionally related to chromospheric lines, can cause a sufficient large perturbation in the TR to be detectable in TR lines. Those results qualitatively increase the interest of studying TR lines as diagnostics of chromospheric phenomena.

The coordinated observations by IRIS and SST have also been helpful in providing additional evidence about the close relationship between surges and UV bursts. Furthermore, we have detected an Ellerman bomb in Hα in the close vicinity of those phenomena. It appears just before the start of the surge and burst, and remains active during the whole lifetime of the burst. This is another piece of evidence that surges are an important instance of eruptive phenomenon and that their understanding in relation to other events is essential.

6.1.3 Forward modeling: combining theory and observations

The development of a theoretical model of the surges and the availability of high-resolution observations opened the possibility of combining them to carry out forward modeling using TR spectral lines. A particularly important aspect concerned the need for the inclusion of NEQ ionization when synthesizing the lines: it was known that the departure from statistical equilibrium can be relevant for the ionization of elements, like silicon and oxygen, that have important resonance lines that form in the TR and that are commonly used as diagnostics of that region. The main conclusions reached are:

- **The importance of NEQ ionization for the diagnostics of surges.**
  We have found that the envelope of the emerged dome and surge are strongly affected by NEQ ionization effects of silicon and oxygen. Comparing the number densities computed via detailed solution of the NEQ rate equations with those obtained assuming statistical equilibrium (SE), we conclude that the SE assumption produces an erroneous result in the population of TR ions such as Si IV and O IV. This is specially evident in the boundaries of the surge, where the SE assumption would mistakenly result in an absence of ions in the ionization state of interest. The TR outside of the flux emergence site is also affected by NEQ, but to a smaller extent, and this corroborates previous results (Olluri et al., 2013a, 2015; Martínez-Sykora et al., 2016b, among others). This has important consequences in the corresponding emissivity of lines typically formed in the TR like Si IV λ1402.77 and λ1393.76, or O IV λ1401.16, λ1404.78. This phenomenon causes the greater Si IV intensity detected in the domain of the surge in the IRIS observations compared to the TR outside. We conclude that

it is not possible to understand the observations of the TR surrounding surges without including NEQ ionization.

- **The NEQ ionization and the role of the entropy sources.**
  Using JPDFs of emissivity vs characteristic heating/cooling times for individual plasma elements, we conclude that there is a definite correlation between high emissivity values for Si IV and O IV and short characteristic cooling times both for the optically thin losses and thermal conduction. We conclude that the latter phenomena are likely to be the underlying cause for the departures from statistical equilibrium in the ionization of silicon and oxygen in the surge's TR. This fact reinforces the conclusion reached in the purely theoretical section of the thesis about the importance of considering the entropy sources when studying the evolution of the eruptive phenomena in the atmosphere.

- **The relation between surges and UV bursts.**
  The two numerical experiments described in Chapters 3 and 4 are able to explain the simultaneous appearance in neighboring locations of a surge and a UV burst: both are a natural consequence of the magnetic reconnection between emerged plasma and the preexisting coronal magnetic field. By means of forward modeling of our numerical experiments, we have found multi-component profiles with large Doppler shifts characteristic of the observed UV bursts in the line of sight coming from the reconnection site in the experiment. Furthermore, one of those numerical experiments has recently been used by Rouppe van der Voort et al. (2017) to compare the synthetic profiles in the current sheet with the complex profiles observed with IRIS and SST. The latter authors show that when the LOS traverses the plasmoids created in the current sheet, the resulting profiles are highly broadened, and often have non-Gaussian and triangular shapes, as seen in the IRIS observations. Although there are still discrepancies between experiments and observations, like the burst intensity, which is substantially larger in the observations, the above results allow us to conclude that we are in the right direction to understand the association between surges and UV bursts.

- **The Line-of-sight (LOS) effects in the surge.**
  The spectral synthesis carried out a posteriori in the numerical experiments has allowed us to conclude that line-of-sight (LOS) effects are important to understand the observations of surges in TR lines. Those effects are tied to the irregular shape of the TR of the surge and cause the enhanced brightness of individual features in its domain. The TR follows the crests and wedges of the surge itself, so the LOS can cross the emitting layer multiple times (multiple-crossings effect), correspondingly increasing the intensity. Additionally, whenever the tangent planes to the surge and LOS are not mutually orthogonal, the intensity emitted in that LOS contains the aggregated contribution of a larger number of plasma elements (alignment effect) and, consequently, it is enhanced, sometimes up to a factor 10. Both the alignment and multiple-crossings effects are particularly conspicuous in the footpoints and crests of the surge. This new result provides an explanation for the remarkable brightness of those regions in the IRIS observations analyzed in this thesis. Furthermore, it may help identify the geometry of surges in future observations of TR lines.

6.1.4 Fortran code development for Bifrost: accelerating the calculation of the ambipolar diffusion term.

In this thesis, we have developed a new Fortran module for the Bifrost code to speed up the calculations of numerical experiments that include ambipolar diffusion. To that end, we implemented the Super Time-Stepping (STS) method that allows us to relax the restrictive CFL criterion necessary when solving explicit diffusion problems. To date, the choice of the two free parameters of the STS method was not specified in the literature. For this reason, we have carried out an in-depth analysis of the method and found an optimum combination that ensures stability and efficiency.

Thanks to this new module, we have also been able to obtain the first preliminary results and conclusions concerning the impact of ambipolar diffusion on surges. We have shown that there is a potentially significant difference in the thermal properties of the emerged region and subsequent surges when taking into account the ion-neutral interaction effects. That difference is caused by the heating associated with the ambipolar diffusion, which is able to offset the strong cooling taking place in specific regions of the emerged plasma in the dome and of the surge. This might have implications concerning the thermal properties of some of the surge populations described in Chapter 2, namely, the coolest surge population (Population C) and, to a lesser extent, Population A. The potential of those results and the possibilities for diagnostic of chromospheric lines need to be further explored in the near future.

6.2 Future perspective

In the following, we describe two relevant aspects to be considered in the near future for eruptive phenomena related to chromospheric plasma such as the surges.

6.2.1 Nonequilibrium ionization

In chromospheric processes that occur on comparatively fast time scales, the ionized species may take longer to recombine than predicted by the local-thermodynamic-equilibrium (LTE) equations. The problem of dealing with the lack of equilibrium of hydrogen and helium in the ionization/recombination processes can be particularly important because it has a bearing on the ambipolar diffusion calculation (see Chapter 5), and consequently, for the rate of dissipated heating; it could modify the radiative losses in the upper chromosphere due to neutral hydrogen, just because they depend on the number density (see Carlsson & Leenaarts, 2012); among others. On the other hand, the ion populations of TR elements calculated through the present NEQ module in Bifrost are not being fed back into the energy equation of the general radiative-MHD calculation (see Chapter 4). This needs to be improved in the future, since it could lead to an underestimate of the effects of the entropy sinks, in particular, of the optically thin losses, in eruptive phenomena. In fact, Hansteen (1993) found deviations of more than a factor two in the optically thin losses when considering NEQ effects in his loop model, so the entropy sinks could be even more efficient than found in our numerical experiments.

6.2.2 The role of the ambipolar diffusion

Another aspect that must be improved is the use of the generalized Ohm's law. On the basis of the general results of Leake & Arber (2006); Arber et al. (2007); Martínez-Sykora et al. (2012); Khomenko & Collados (2012); Leake & Linton (2013); Martínez-Sykora et al. (2015), among others, we expect that the ambipolar diffusion may lead to enough friction between the neutrals and ions to counteract to some extent the cold temperatures of the rising dome and affect the subsequent ejective phenomena like surges. Additionally, ambipolar diffusion has been studied in different scenarios, finding that it is able to easily promote instabilities in prominences (Khomenko et al., 2014) and that it is a key mechanism for the formation of type-II spicules (Martínez-Sykora et al., 2017; Martínez-Sykora et al., 2017). Moreover, our preliminary results show a significant impact of the ambipolar heating on the thermal properties of the magnetized emerged dome and the subsequent surge. On the other hand, the effects of the ambipolar diffusion and associated heating and NEQ ionization are likely to strongly affect the typical spectral lines in which chromospheric diagnostics are based on. Primary examples are Hα 6563 Å, He I 10830 Å, He II 304 Å, among others (see, e.g., Golding et al., 2014; Leenaarts et al., 2015, 2016).

Publications

Published papers during the course of this thesis.

1. *The Cool Surge Following Flux Emergence in a Radiation-MHD Experiment.*
Nóbrega-Siverio, D., Moreno-Insertis, F., and Martínez-Sykora, J.
The Astrophysical Journal (ApJ), May 2016, Volume 822.
`http://adsabs.harvard.edu/abs/2016ApJ...822...18N`

2. *Two-dimensional Radiative Magnetohydrodynamic Simulations of Partial Ionization in the Chromosphere. II. Dynamics and Energetics of the Low Solar Atmosphere.*
Martínez-Sykora, J., De Pontieu, B., Carlsson, M., Hansteen, V., **Nóbrega-Siverio, D.**, and Gudiksen, B.
The Astrophysical Journal (ApJ), September 2017, Volume 847.
`http://http://adsabs.harvard.edu/abs/2017ApJ...847...36M`

3. *Surges and Si IV Bursts in the Solar Atmosphere: Understanding IRIS and SST Observations through RMHD Experiments.*
Nóbrega-Siverio, D., Martínez-Sykora, J., Moreno-Insertis, F., and Rouppe van der Voort, L. R.
The Astrophysical Journal (ApJ), December 2017, Volume 850.
`http://adsabs.harvard.edu/abs/2017ApJ...850..153N`

4. *Intermittent Reconnection and Plasmoids in UV Bursts in the Low Solar Atmosphere.*
Rouppe van der Voort, L. R., De Pontieu, B., Scharmer, G. B., de la Cruz Rodríguez, J., Martínez-Sykora, J., **Nóbrega-Siverio, D.**, Guo, L. J., Jafarzadeh, S., Pereira, T. M. D., Hansteen, V., Carlsson, M., Vissers, G.
The Astrophysical Journal Letters (ApJL), December 2017, Volume 851.
`http://http://adsabs.harvard.edu/abs/2017ApJ...851L...6R`

5. *On the Importance of the Nonequilibrium Ionization of Si IV and O IV and the line-of-sight in Solar Surges.*
Nóbrega-Siverio, D., Moreno-Insertis, F., Martínez-Sykora, J.
The Astrophysical Journal (ApJ), May 2018, Volume 858.
`http://adsabs.harvard.edu/abs/2018ApJ...858....8N`

Bibliography

Alexiades, V., Amiez, G., & Gremaud, P. 1996, Super-time-stepping acceleration of explicit schemes for parabolic problems

Altas, L., & Duzgelen, A. 1997, Solar Physics, 171, 145

Arber, T. D., Haynes, M., & Leake, J. E. 2007, ApJ, 666, 541

Archontis, A., Moreno-Insertis, F., Galsgaard, K., Hood, A., & O'Shea, E. 2004, A&A, 426, 1047

Archontis, V., & Hood, A. W. 2013, ApJL, 769, L21

Arnaud, M., & Rothenflug, R. 1985, A&AS, 60, 425

Asai, A., Ishii, T. T., & Kurokawa, H. 2001, ApJL, 555, L65

Ballester, J. L., et al. 2018, Space Science Reviews, 214, 58

Bennett, S. M., & Erdélyi, R. 2015, ApJ, 808, 135

Bohlin, J. D., Vogel, S. N., Purcell, J. D., Sheeley, Jr., N. R., Tousey, R., & Vanhoosier, M. E. 1975, ApJL, 197, L133

Bong, S.-C., Cho, K.-S., & Yurchyshyn, V. 2014, Journal of Korean Astronomical Society, 47, 311

Bradshaw, S. J., & Cargill, P. J. 2006, A&A, 458, 987

Bradshaw, S. J., & Klimchuk, J. A. 2011, ApJS, 194, 26

Bradshaw, S. J., & Mason, H. E. 2003, A&A, 401, 699

Braginskii, S. I. 1965, Reviews of Plasma Physics, 1, 205

Brooks, D. H., Kurokawa, H., & Berger, T. E. 2007, ApJ, 656, 1197

Canfield, R. C., Reardon, K. P., Leka, K. D., Shibata, K., Yokoyama, T., & Shimojo, M. 1996, ApJ, 464, 1016

Cao, T.-j., Xu, A.-a., & Tang, Y.-h. 1980, Chinese Astronomy, 4, 143

Carlsson, M., & Leenaarts, J. 2012, A&A, 539, A39

Carmichael, H. 1964, NASA Special Publication, 50, 451

Carrington, R. C. 1859, MNRAS, 20, 13

Cavallini, F., Berrilli, F., Cantarano, S., & Egidi, A. 2000, in ESA Special Publication, Vol. 463, The Solar Cycle and Terrestrial Climate, Solar and Space weather, ed. A. Wilson, 607

Chae, J., Qiu, J., Wang, H., & Goode, P. R. 1999, ApJL, 513, L75

Chen, H. D., Jiang, Y. C., & Ma, S. L. 2008, A&A, 478, 907

Chen, J., Su, J., Deng, Y., & Priest, E. R. 2017, ApJ, 840, 54

Cheung, M. C. M., & Cameron, R. H. 2012, ApJ, 750, 6

Cheung, M. C. M., & Isobe, H. 2014, Living Reviews in Solar Physics, 11, 3

Cheung, M. C. M., Schüssler, M., & Moreno-Insertis, F. 2007, A&A, 467, 703

Chintzoglou, G., De Pontieu, B., Martínez-Sykora, J., Pereira, T. M. D., Vourlidas, A., & Tun Beltran, S. 2018, ApJ, 857, 73

Chitta, L. P., Peter, H., Young, P. R., & Huang, Y.-M. 2017, A&A, 605, A49

Choi, E., Kim, J., & Wiita, P. J. 2009, ApJS, 181, 413

Courant, R., Friedrichs, K., & Lewy, H. 1928, Mathematische Annalen, 100, 32

Cowling, T. G. 1976, Magnetohydrodynamics (Crane Russak and Co)

De Pontieu, B., De Moortel, I., Martinez-Sykora, J., & McIntosh, S. W. 2017a, ApJL, 845, L18

De Pontieu, B., & Haerendel, G. 1998, A&A, 338, 729

De Pontieu, B., Martens, P. C. H., & Hudson, H. S. 2001, ApJ, 558, 859

De Pontieu, B., Martínez-Sykora, J., & Chintzoglou, G. 2017b, ApJL, 849, L7

De Pontieu, B., McIntosh, S., Martinez-Sykora, J., Peter, H., & Pereira, T. M. D. 2015, ApJL, 799, L12

De Pontieu, B., et al. 2007, PASJ, 59, 655

—. 2014, Solar Physics

Drews, A., & Rouppe van der Voort, L. 2017, A&A, 602, A80

Ellison, M. A. 1943, MNRAS, 103, 3

—. 1949, MNRAS, 109, 3

Emonet, T., & Moreno-Insertis, F. 1998, ApJ, 492, 804

Fan, Y. 2001, ApJL, 554, L111

Fang, F., Fan, Y., & McIntosh, S. W. 2014, ApJL, 789, L19

Fletcher, L., et al. 2011, Space Science Reviews, 159, 19

Fontenla, J. M., Avrett, E. H., & Loeser, R. 1993, ApJ, 406, 319

Forbes, T. G., & Priest, E. R. 1984, Solar Physics, 94, 315

Furth, H. P., Killeen, J., & Rosenbluth, M. N. 1963, Physics of Fluids, 6, 459

Gaizauskas, V. 1996, Solar Physics, 169, 357

Geiss, J., & Buergi, A. 1986, A&A, 159, 1

Golding, T. P., Carlsson, M., & Leenaarts, J. 2014, ApJ, 784, 30

Green, L. M., Török, T., Vršnak, B., Manchester, W., & Veronig, A. 2018, Space Science Reviews, 214, 46

Grubecka, M., Schmieder, B., Berlicki, A., Heinzel, P., Dalmasse, K., & Mein, P. 2016, A&A, 593, A32

Gu, X. M., Lin, J., Li, K. J., Xuan, J. Y., Luan, T., & Li, Z. K. 1994, A&A, 282, 240

Gudiksen, B. V., Carlsson, M., Hansteen, V. H., Hayek, W., Leenaarts, J., & Martínez-Sykora, J. 2011, A&A, 531, A154+

Guglielmino, S. L., Bellot Rubio, L. R., Zuccarello, F., Aulanier, G., Vargas Domínguez, S., & Kamio, S. 2010, ApJ, 724, 1083

Guglielmino, S. L., Zuccarello, F., Young, P. R., Murabito, M., & Romano, P. 2018, ApJ, 856, 127

Gustafsson, B., Bell, R. A., Eriksson, K., & Nordlund, A. 1975, A&A, 42, 407

Habbal, S. R., & Gonzalez, R. D. 1991, ApJL, 376, L25

Hansteen, V. 1993, ApJ, 402, 741

Hansteen, V. H., Archontis, V., Pereira, T. M. D., Carlsson, M., Rouppe van der Voort, L., & Leenaarts, J. 2017, ApJ, 839, 22

Hansteen, V. H., De Pontieu, B., Rouppe van der Voort, L., van Noort, M., & Carlsson, M. 2006, Apj, 647, L73

Harvey, K., & Harvey, J. 1973, Solar Physics, 28, 61

Hayek, W., Asplund, M., Carlsson, M., Trampedach, R., Collet, R., Gudiksen, B. V., Hansteen, V. H., & Leenaarts, J. 2010, A&A, 517, A49+

Heyvaerts, J., Priest, E. R., & Rust, D. M. 1977, ApJ, 216, 123

Hirayama, T. 1974, Solar Physics, 34, 323

Hodgson, R. 1859, MNRAS, 20, 15

Huang, Z., Madjarska, M. S., Koleva, K., Doyle, J. G., Duchlev, P., Dechev, M., & Reardon, K. 2014, A&A, 566, A148

Huang, Z., Madjarska, M. S., Scullion, E. M., Xia, L.-D., Doyle, J. G., & Ray, T. 2017, MNRAS, 464, 1753

Hyman, J., Vichnevtsky, R., & Stepleman, R. 1979, Adv. in Comp. Meth, PDE's-III, 313

Iijima, H., & Yokoyama, T. 2015, ApJL, 812, L30

Jiang, R.-L., Fang, C., & Chen, P.-F. 2012, ApJ, 751, 152

Jiang, Y. C., Chen, H. D., Li, K. J., Shen, Y. D., & Yang, L. H. 2007, A&A, 469, 331

Jibben, P., & Canfield, R. C. 2004, ApJ, 610, 1129

Joselyn, J. A., Munro, R. H., & Holzer, T. E. 1979, ApJS, 40, 793

Judge, P. G. 2015, ApJ, 808, 116

Karlický, M., Bárta, M., & Rybák, J. 2010, A&A, 514, A28

Katsukawa, Y., et al. 2007, Science, 318, 1594

Kayshap, P., Srivastava, A. K., Murawski, K., & Tripathi, D. 2013, ApJL, 770, L3

Khomenko, E., & Collados, M. 2012, ApJ, 747, 87

Khomenko, E., Díaz, A., de Vicente, A., Collados, M., & Luna, M. 2014, A&A, 565, A45

Kim, Y.-H., et al. 2015, ApJ, 810, 38

Kirshner, R. P., & Noyes, R. W. 1971, Solar Physics, 20, 428

Kneer, F. 1980, A&A, 87, 229

Kopp, R. A., & Pneuman, G. W. 1976, Solar Physics, 50, 85

Kurokawa, H., & Kawai, G. 1993, in Astronomical Society of the Pacific Conference Series, Vol. 46, IAU Colloq. 141: The Magnetic and Velocity Fields of Solar Active Regions, ed. H. Zirin, G. Ai, & H. Wang, 507

Kurokawa, H., Liu, Y., Sano, S., & Ishii, T. T. 2007, in Astronomical Society of the Pacific Conference Series, Vol. 369, New Solar Physics with Solar-B Mission, ed. K. Shibata, S. Nagata, & T. Sakurai, 347

Kuźma, B., Murawski, K., Zaqarashvili, T. V., Konkol, P., & Mignone, A. 2017, A&A, 597, A133

Leake, J. E., & Arber, T. D. 2006, A&A, 450, 805

Leake, J. E., Arber, T. D., & Khodachenko, M. L. 2005, A&A, 442, 1091

Leake, J. E., & Linton, M. G. 2013, ApJ, 764, 54

Leenaarts, J. 2018, ArXiv e-prints

Leenaarts, J., Carlsson, M., Hansteen, V., & Rutten, R. J. 2007, A&A, 473, 625

Leenaarts, J., Carlsson, M., & Rouppe van der Voort, L. 2015, ApJ, 802, 136

Leenaarts, J., Golding, T., Carlsson, M., Libbrecht, T., & Joshi, J. 2016, A&A, 594, A104

Li, H., et al. 2017, ApJL, 842, L20

Li, Z., Fang, C., Guo, Y., Chen, P. F., Zou, P., & Cao, W. 2016, ApJ, 826, 217

Liu, W., Berger, T. E., Title, A. M., & Tarbell, T. D. 2009, ApJL, 707, L37

Liu, Y., & Kurokawa, H. 2004, ApJ, 610, 1136

MacTaggart, D., Guglielmino, S. L., Haynes, A. L., Simitev, R., & Zuccarello, F. 2015, A&A, 576, A4

Madjarska, M. S., Doyle, J. G., & de Pontieu, B. 2009, ApJ, 701, 253

Madjarska, M. S., Doyle, J. G., Hochedez, J.-F., & Theissen, A. 2006, A&A, 452, L11

Madjarska, M. S., Huang, Z., Galsgaard, K., Doyle, J. G., Scullion, E. M., Xia, L., & Ray, T. 2017, MNRAS, in preparation

Martínez-Sykora, J., De Pontieu, B., Carlsson, M., & Hansteen, V. 2016a, ApJL, 831, L1

Martínez-Sykora, J., De Pontieu, B., Carlsson, M., Hansteen, V. H., Nóbrega-Siverio, D., & Gudiksen, B. V. 2017, ApJ, 847, 36

Martínez-Sykora, J., De Pontieu, B., De Moortel, I., Hansteen, V. H., & Carlsson, M. 2018, ArXiv e-prints

Martínez-Sykora, J., De Pontieu, B., & Hansteen, V. 2012, ApJ, 753, 161

Martínez-Sykora, J., De Pontieu, B., Hansteen, V., & Carlsson, M. 2015, Royal Society of London Philosophical Transactions Series A, 373, 40268

Martínez-Sykora, J., De Pontieu, B., Hansteen, V. H., & Gudiksen, B. 2016b, ApJ, 817, 46

Martínez-Sykora, J., De Pontieu, B., Hansteen, V. H., Rouppe van der Voort, L., Carlsson, M., & Pereira, T. M. D. 2017, Science, 356, 1269

Martínez-Sykora, J., Hansteen, V., & Carlsson, M. 2008, ApJ, 679, 871

McMath, R. R., & Mohler, O. 1948, The Observatory, 68, 110

McMath, R. R., & Pettit, E. 1937, ApJ, 85, 279

Meyer, C. D., Balsara, D. S., & Aslam, T. D. 2012, MNRAS, 422, 2102

Mitchner, M., & Kruger, C. H. 1973, Partially ionized gases (John Wiley and Sons Inc)

Moore, R. L., Cirtain, J. W., Sterling, A. C., & Falconer, D. A. 2010, ApJ, 720, 757

Moreno-Insertis, F. 2018, ApJ, in preparation

Moreno-Insertis, F., & Galsgaard, K. 2013, ApJ, 771, 20

Moreno-Insertis, F., Galsgaard, K., & Ugarte-Urra, I. 2008, ApJL, 673, L211

Moreno-Insertis, F., Martínez-Sykora, J., Hansteen, V. H., & Muñoz, D. 2018, submitted to ApJ

Murawski, K., Srivastava, A. K., & Zaqarashvili, T. V. 2011, A&A, 535, A58

Nakai, Y., & Hattori, A. 1985, Memoirs Faculty of Sciences University of Kyoto, 36, 385

Nelson, C. J., & Doyle, J. G. 2013, A&A, 560, A31

Newcomb, W. A. 1961, Physics of Fluids, 4, 391

Newton, H. W. 1942, MNRAS, 102, 2

Ni, L., Zhang, Q.-M., Murphy, N. A., & Lin, J. 2017, ApJ, 841, 27

Nishizuka, N., Shimizu, M., Nakamura, T., Otsuji, K., Okamoto, T. J., Katsukawa, Y., & Shibata, K. 2008, ApJL, 683, L83

Nóbrega-Siverio, D., Martínez-Sykora, J., Moreno-Insertis, F., & Rouppe van der Voort, L. 2017, ApJ, 850, 153

Nóbrega-Siverio, D., Moreno-Insertis, F., & Martínez-Sykora, J. 2016, ApJ, 822, 18

—. 2018, ApJ, 858, 8

Nordlund, Å. 1982, Aap, 107, 1

Nordlund, Å., & Galsgaard, K. 1995, A 3D MHD Code for Parallel Computers

Nordlund, Å., Stein, R. F., & Asplund, M. 2009, Living Reviews in Solar Physics, 6, 2

Olluri, K., Gudiksen, B. V., & Hansteen, V. H. 2013a, ApJ, 767, 43

—. 2013b, Astronomical Journal, 145, 72

Olluri, K., Gudiksen, B. V., Hansteen, V. H., & De Pontieu, B. 2015, ApJ, 802, 5

Ortiz, A., Bellot Rubio, L. R., Hansteen, V. H., de la Cruz Rodríguez, J., & Rouppe van der Voort, L. 2014, ApJ, 781, 126

Osterbrock, D. E. 1961, ApJ, 134, 347

O'Sullivan, S., & Downes, T. P. 2006, MNRAS, 366, 1329

—. 2007, MNRAS, 376, 1648

Özgüç, A. 1989, Solar Physics, 123, 381

Özgüç, A., Yesilyaprak, H., & Duzgelen, A. 1991, A&A, 241, 209

Pariat, E., Dalmasse, K., DeVore, C. R., Antiochos, S. K., & Karpen, J. T. 2016, A&A, 596, A36

Pereira, T. M. D., De Pontieu, B., & Carlsson, M. 2012, ApJ, 759, 18

Pereira, T. M. D., Rouppe van der Voort, L., & Carlsson, M. 2016, ApJ, 824, 65

Pereira, T. M. D., et al. 2014, ApJL, 792, L15

Peter, H., et al. 2014, Science, 346, 1255726

Petschek, H. E. 1964, NASA Special Publication, 50, 425

Pike, C. D., & Harrison, R. A. 1997, Solar Physics, 175, 457

Priest, E. 2014, Magnetohydrodynamics of the Sun (Cambridge University Press)

Priest, E. R., & Forbes, T. G. 2002, Astronomy and Astrophysics Review, 10, 313

Raouafi, N. E., et al. 2016, Space Science Reviews, 201, 1

Raymond, J. C., & Dupree, A. K. 1978, ApJ, 222, 379

Reep, J. W., Warren, H. P., Crump, N. A., & Simões, P. J. A. 2016, ApJ, 827, 145

Robustini, C., Leenaarts, J., de la Cruz Rodriguez, J., & Rouppe van der Voort, L. 2016, A&A, 590, A57

Rouppe van der Voort, L., et al. 2017, ApJL, 851, L6

Roy, J.-R. 1973, Solar Physics, 32, 139

Rust, D. M. 1976, Philosophical Transactions of the Royal Society of London Series A, 281, 353

Rutten, R. J., Vissers, G. J. M., Rouppe van der Voort, L. H. M., Sütterlin, P., & Vitas, N. 2013, in Journal of Physics Conference Series, Vol. 440, Journal of Physics Conference Series, 012007

Samanta, T., Tian, H., Banerjee, D., & Schanche, N. 2017, ApJL, 835, L19

Savcheva, A., et al. 2007, PASJ, 59, S771

Scharmer, G. B., Bjelksjo, K., Korhonen, T. K., Lindberg, B., & Petterson, B. 2003, in Society of Photo-Optical Instrumentation Engineers (SPIE) Conference Series, Vol. 4853, Society of Photo-Optical Instrumentation Engineers (SPIE) Conference Series, ed. S. L. Keil & S. V. Avakyan, 341–350

Scharmer, G. B., et al. 2008, ApJL, 689, L69

Schlüter, A. 1957, in IAU Symposium, Vol. 4, Radio astronomy, ed. H. C. van de Hulst, 356

Schmahl, E. J. 1981, Solar Physics, 69, 135

Schmieder, B., Mein, P., Martres, M. J., & Tandberg-Hanssen, E. 1984, Solar Physics, 94, 133

Schmieder, B., Shibata, K., van Driel-Gesztelyi, L., & Freeland, S. 1995, Solar Physics, 156, 245

Schrijver, C. J., & Higgins, P. A. 2015, Solar Physics, 290, 2943

Shelyag, S., Khomenko, E., de Vicente, A., & Przybylski, D. 2016, ApJL, 819, L11

Shen, Y., Liu, Y. D., Su, J., Qu, Z., & Tian, Z. 2017, ApJ, 851, 67

Shibata, K., & Magara, T. 2011, Living Reviews in Solar Physics, 8, 6

Shibata, K., Nishikawa, T., Kitai, R., & Suematsu, Y. 1982, Solar Physics, 77, 121

Shibata, K., Nozawa, S., & Matsumoto, R. 1992a, PASJ, 44, 265

Shibata, K., et al. 1992b, PASJ, 44, L173

Shimizu, T., et al. 2009, ApJL, 696, L66

Shimojo, M., Hashimoto, S., Shibata, K., Hirayama, T., Hudson, H. S., & Acton, L. W. 1996, PASJ, 48, 123

Skartlien, R. 2000, ApJ, 536, 465

Skogsrud, H., Rouppe van der Voort, L., De Pontieu, B., & Pereira, T. M. D. 2015, ApJ, 806, 170

Spitzer, L. 1956, Physics of Fully Ionized Gases (New York: Interscience Publishers)

Steinolfson, R. S., Wu, S. T., & Schmahl, E. J. 1979, Solar Physics, 63, 187

Sturrock, P. A. 1966, Nature, 211, 695

Takasao, S., Isobe, H., & Shibata, K. 2013, PASJ, 65, 62

Tian, H., Xu, Z., He, J., & Madsen, C. 2016, ApJ, 824, 96

Tian, H., et al. 2014, Science, 346, 1255711

—. 2018, ApJ, 854, 92

Tortosa-Andreu, A., & Moreno-Insertis, F. 2009, A&A, 507, 949

Tsiropoula, G., Tziotziou, K., Kontogiannis, I., Madjarska, M. S., Doyle, J. G., & Suematsu, Y. 2012, Space Science Reviews, 169, 181

Uddin, W., Schmieder, B., Chandra, R., Srivastava, A. K., Kumar, P., & Bisht, S. 2012, ApJ, 752, 70

Švestka, Z. 1951, Bulletin of the Astronomical Institutes of Czechoslovakia, 2, 100

Vargas Domínguez, S., Kosovichev, A., & Yurchyshyn, V. 2014, ApJ, 794, 140

Verma, V. K. 1984, Solar Physics, 94, 155

—. 1985, Solar Physics, 97, 381

—. 1986, Solar Physics, 106, 67

Vissers, G. J. M., Rouppe van der Voort, L. H. M., & Rutten, R. J. 2013, ApJ, 774, 32

Vissers, G. J. M., Rouppe van der Voort, L. H. M., Rutten, R. J., Carlsson, M., & De Pontieu, B. 2015, ApJ, 812, 11

von Steiger, R., & Geiss, J. 1989, A&A, 225, 222

Vranjes, J., & Krstic, P. S. 2013, A&A, 554, A22

Vranjes, J., Poedts, S., Pandey, B. P., & de Pontieu, B. 2008, A&A, 478, 553

Wang, H., & Liu, C. 2012, ApJ, 760, 101

Wang, J. f., Zhou, T. h., & Ji, H. s. 2014, Chinese Astronomy and Astrophysics, 38, 65

Wang, Y.-M., et al. 1998, ApJ, 508, 899

Watanabe, H., Vissers, G., Kitai, R., Rouppe van der Voort, L., & Rutten, R. J. 2011, ApJ, 736, 71

Webb, D. F., & Howard, T. A. 2012, Living Reviews in Solar Physics, 9, 3

Xu, A.-a., Tang, Y.-h., & Cao, T.-j. 1981, Chinese Astronomy and Astrophysics, 5, 44

Yan, X. L., et al. 2017, ApJ, 845, 18

Yang, H., Chae, J., Lim, E.-K., Lee, K.-s., Park, H., Song, D.-u., & Cho, K. 2014, ApJL, 790, L4

Yang, H., et al. 2013a, Solar Physics, 288, 39

Yang, L., He, J., Peter, H., Tu, C., Zhang, L., Feng, X., & Zhang, S. 2013b, ApJ, 777, 16

Yang, L., Peter, H., He, J., Tu, C., Wang, L., Zhang, L., & Yan, L. 2018, ApJ, 852, 16

Yokoyama, T., & Shibata, K. 1995, Nature, 375, 42

—. 1996, PASJ, 48, 353

Yoshimura, K., Kurokawa, H., Shimojo, M., & Shine, R. 2003, PASJ, 55, 313

Young, P. R., & Muglach, K. 2014, Solar Physics, 289, 3313

Young, P. R., et al. 2018, ArXiv e-prints

Zhang, J., Wang, J., & Liu, Y. 2000, A&A, 361, 759

Zhang, Q. M., & Ji, H. S. 2014, A&A, 561, A134

Zhao, T., Ni, L., Lin, J., & Ziegler, U. 2018, ArXiv e-prints

Zhelyazkov, I., Zaqarashvili, T. V., Chandra, R., Srivastava, A. K., & Mishonov, T. 2015, Advances in Space Research, 56, 2727

Zheng, R., Jiang, Y., Yang, J., Bi, Y., Hong, J., Yang, B., & Yang, D. 2013, ApJ, 764, 70

Zweibel, E. G. 2015, in Astrophysics and Space Science Library, Vol. 407, Magnetic Fields in Diffuse Media, ed. A. Lazarian, E. M. de Gouveia Dal Pino, & C. Melioli, 285

Zweibel, E. G., Lawrence, E., Yoo, J., Ji, H., Yamada, M., & Malyshkin, L. M. 2011, Physics of Plasmas, 18, 111211

Acknowledgments

First of all, I would like to express my special thanks of gratitude to my supervisor Professor Fernando Moreno Insertis for introducing me to the exciting topic of solar physics. There is no way to put into words his immense guidance and infinite advices during the course of this thesis, as well as for the countless interesting discussions and English lessons we have had over all my PhD years.

I am also profoundly grateful to my co-supervisor Dr. Juan Martínez Sykora for his extraordinary support and help in this thesis process. The research stays at Lockheed Martin Solar and Astrophysics Laboratory (LMSAL) would not have been possible without the contribution of him and his family and friends.

I would like to thank to all the LMSAL group for the warm reception during the months I was there as part of my thesis, as well as to the members of the RoCS team at Oslo for their help and trust to keep developing my research career.

I am also grateful to the following Drs., namely, Eric Priest, Alan Hood, Maria Madjarska, Gregal Vissers, Peter Young, and Jaroslav Dudík for their constructive comments to improve the papers that constitute this thesis.

Last but not least, thanks to my parents, girlfriend and friends for their inestimable support and company during this long journey.

This thesis project would have been impossible without the support by the Spanish Ministry of Economy and Competitiveness (MINECO) through projects AYA2011-24808 and AYA2014-55078-P, as well as by NASA through grants NNX14- AI14G, NNH15ZDA001N, NNX16AG90G, NNX17AD33G, and by NSF grant AST- 1714955 and contract NNG09FA40C (IRIS). The authors thankfully acknowledge the computer resources and the technical expertise and assistance provided at the LaPalma supercomputer installation (IAC, Spain), at the Teide High-Performance Computing (HPC) facilities (Instituto Tecnologico y de Energias Renovables, ITER, Spain), and at MareNostrum (BSC/CNS/RES, Spain).

Daniel Nóbrega-Siverio